Speckle Reduction and Lesion Segmentation for Optical Coherence Tomography Images of Teeth

by

Jialin Li

A thesis submitted to the Faculty of Graduate Studies of

the University of Manitoba

in partial fulfillment of the requirements for the degree of

MASTER OF SCIENCE

Department of Electrical and Computer Engineering

University of Manitoba

Winnipeg

Abstract

The objective of this study is to apply digital image processing (DIP) techniques to optical coherence tomography (OCT) images and develop computer-based non-subjective quantitative analysis, which can be used as diagnostic aids in early detection of dental caries. This study first compares speckle reduction effects on raw OCT image data by implementing spatial-domain and transform-domain speckle filtering. Then region-based contour search and global thresholding techniques examine digital OCT images with possible lesions to identify and highlight the presence of features indicating early stage dental caries. The outputs of these processes, which explore the combination of image restoration and segmentation, can be used to distinguish lesion from normal tissue and determine the characteristics prior to, during, and following treatments. The combination of image processing and analysis techniques in this thesis shows potential of detecting early stage caries lesion successfully.

Acknowledgements

This thesis arose in part out of my research that has been done since I came to the National Research Council Canada-Institute for Biodiagnostics (NRC-IBD) Spectroscopy Group. I have worked with a great number of people whose contributions in many ways have helped in completing the thesis and deserved mention. It is a pleasure to convey my gratitude to them all in my humble acknowledgement.

First and foremost I offer my sincerest gratitude to my project supervisor Dr. Lin-P'ing Choo-Smith, who has supported me throughout my thesis with her guidance, knowledge and unending patience. Above all and the most needed, she provided me invaluable encouragement and support in various ways. Without her persistent help this thesis would not have been possible. My thanks are also extended to Dr. Christopher Bowman for his guidance and crucial contribution on image processing techniques.

In addition, gratitude is also due to the members of the supervisory committee, Dr. Reza Fazel and Dr. Gabriel Thomas. Without whose knowledge and assistance this study would not have been successful. Special thanks are extended to Mark Hewko and Michael Smith, for their help with this project. Finally, I thank my parents for their unwavering support and encouragement throughout all my studies at the university.

Table of Contents

List of Tables

List of Figures

Chapter 1

Introduction

A significant amount of research is directed towards earlier and better caries detection. Next to the question of detecting caries at its early stages, is the issue of treatment decision which relies on acquiring quantitative measure of lesion extent. A quantitative measure of early stage caries is important to monitor lesion progress, and to determine whether surgical intervention is needed, or the lesion can be arrested or is arrested or reversed. In contrast to the attention given to the discovery and development of new diagnostic imaging technologies, few applications use the quantitative evaluation of dental images to diagnose caries. As an emerging technology for performing high resolution imaging, optical coherence tomography (OCT) can be used to identify tooth damage due to caries, compensating for the low sensitivity (high false negative) rate of visual inspection by dentists. The addition of OCT as well as other imaging tools to traditional dental practice could lead to a shift in diagnosis from subjective interpretation to quantitative analysis and measurement. If the shape of caries can be quantified, and the relationship between the numerical value and the condition of the lesion can be demonstrated, this information would be helpful to diagnose dental caries with great precision.

Reproducible dental image analysis driven by algorithms that enable geometric measurement of structures is guided with the information present in the images, as well as embedded anatomical features. The aim of this study is to assess the possibility of digital image processing and analysis of OCT dental images, by means of applying image restoration methods to speckle contaminated images, and applying semi-automatic image segmentation to generate image partition with geometric details which defines basic anatomical landmarks. Here I first provide an overview of current clinical dental caries diagnostic methods and a review of some new imaging tools to bring forward the understanding of the present development in dental imaging.

1.1 Current Clinical Dental Caries Detection Overview

Dental caries, also generally known as tooth decay, is a common bacteria based disease. The mechanism of dental caries is well-understood. It is caused by the acid erosion of tooth enamel. The process starts with the plaque on the surface of the tooth and the plaque consists of a bacterial film that produces acids. As the amount of bacterial plaque increases, acid produced by bacterial action diffuses into the tooth and dissolves the carbonated mineral - a process called demineralization [1], [2], [3]. Dental caries is a dynamic process with periods of demineralization alternating with periods of remineralization (re-deposition of mineral). However, if this process is not halted or reversed via remineralization, it eventually becomes a frank cavity. Dental caries of the enamel typically is first observed clinically as a so-called “white spot” lesion.

Current and previous clinical technologies, largely based on subjective parameters such as color, translucency and hardness aided by relatively basic instruments such as explorers, viewing mirrors, and artificial light sources, usually result in low sensitivity and high specificity, meaning a large number of lesions may be missed. This visual and tactile approach is often supplemented by the use of selected radiographs to help in the diagnosis of small lesions on the surfaces between adjacent teeth [4], [5]. The prime treatment objective for carious teeth is complete removal of infected tooth enamel or dentin followed by placement of restorative materials. Since dental caries is a dynamic process, the recent trend in management of non-cavitated early stage lesions has been a shift from the operative to a more conservative approach to inhibiting and reversing lesion progression. Thus, the early clinical detection of incipient carious lesions has attracted increasing interest because of the possibility that primary preventive procedures (e.g. topical fluorides) may enhance remineralization and even arrest dental decay rather than requiring operative intervention.

In the past 20 years, many efforts have been dedicated to the development of new technologies for early stage caries detection [6]. The on-going progress in caries research has offered us great opportunities to better understand, detect, and monitor the disease. These new technologies include quantitative laser or light fluorescence (QLF), electrical conductance measurements (ECM), infrared laser fluorescence and digital fiber-optics trans-illumination [7]. A significant recent discovery in the field of biomedical science is the utilization of light and fiber-optics to view living biological tissues in a technique known as optical coherence tomography (OCT). OCT imaging has been applied to diagnose dental caries in its incipient stage with its advantage over conventional digital radiography without ionizing radiation, and benefits in non-invasive, and thus nondestructive imaging the anatomical feature of the dental structure over other conventional imaging modalities, including eye inspection (EI), digital intraoral radiography (DIOR), light illuminating examination (LIE), and electron probe micro analyzer (EPMA) [8]. For further reading, one can also refer to Hall & Girkin [9] for a review of potential new diagnostic modalities for caries lesions, including multi-photon imaging, infrared thermography and infrared fluorescence, ultrasound, terahertz imaging and optical coherence tomography. Among these novel medical imaging techniques, optical coherence tomography has offered better resolution, depth in penetration, and quality.

1.2 An OCT Approach and Digital Image Analysis

Optical coherence tomography techniques generate cross-sectional images from a series of laterally adjacent depth-scans [10]. Optical tomographic techniques are of particular importance in the medical fields, as these techniques can provide non-invasive diagnostic images. Along with rapid expanding in research and commercial development in OCT imaging techniques, an OCT imaging system has characteristics of compact dimension, and reliability, in addition, offers a therapeutic potential in providing anatomic and functional information in intact tissues with micron-scale resolution. One of the attractive features of OCT is that it uses near-infrared light instead of ionizing radiation. Furthermore, high transversal and depth resolution on the order of 10 μm can be obtained. The very first commercialized applications are in the field of ophthalmology, where OCT enables a total non-invasive view of the retinal tissue structure. The capability of bringing microscopic detail *in vivo* equals "optical biopsy" which potentially could replace many invasive biopsy procedures to support diagnosis in many fields beyond ophthalmology.

Owing to its high axial (~10-20 μm) and transversal (~10 μm) resolution, OCT is expected to improve the management of dental caries. OCT holds promise for detecting early lesion involving enamel and for quantifying enamel demineralization. With its potential application in dentistry, researchers investigate the assessment of imaging dental soft and hard tissues [11]. Some preliminary studies have applied OCT technique to obtain tomographic images of extracted sound and decayed human teeth in order to evaluate its possible diagnostic potential for dental applications [12], [13], [14], [15], [35] , [36], [37]. Optical scattering properties of different tissues are translated into contrast variations that can be used to image and identify structural components. The image contrast between healthy and carious tooth structures attainable from OCT images is a promising prognosis for detection of caries. Despite this obvious advantage, OCT images suffer contrast and resolution degradation caused by contaminating speckle noise and it is the primary hurdle to be overcome in digital image processing concerning the inability to adequately identify the carious lesion. Thus, prior to image analysis based lesion segmentation, the image preprocessing aims at noise reduction, and contrast/resolution enhancement.

Chapter 2

OCT Background

This chapter reviews the basic concepts of OCT signal formation, and the OCT imaging applied to early stage dental caries detection. Some fundamental anatomy of human tooth is also reviewed.

2.1 Principles of OCT

In many ways, time domain OCT can be represented as an optical analogue to ultrasound (US) imaging [16]. Laterally adjacent depth-scans are similar to A-scan of ultrasound imaging. Typically, OCT techniques, like the reflectometry technique, are based on time-domain low coherence interferometry depth-scans. Due to the speed of light however, practical OCT systems cannot measure return signal on time-of-flight basis (compared to ultrasound) and the time "delay" is translated into time difference during the interference. An optical interferometric scheme is used as an indirect way to visualize coherently reflected or scattered light. A standard Michelson interferometer, with a low-coherence time-domain broadband light source, is used to measure the relative optical path difference between a reference arm and the various layers of tissue samples in the sample arm. **Figure 2.1** depicts a standard OCT scheme. In its simplest form, a particular incoherent light source illuminates a Michelson interferometer. The signal beam is reflected from the biological specimen and a reference beam is reflected from a reference mirror while scanning over an optical delay line at kHz speed. Two beams interfere at a depth in the tissue corresponding with the position of the reference mirror at each moment and a detector measures the intensity of the backscatters of the interference. This way, an axial image (A-scan) of the tissue is produced. By scanning the beam transversely, a two dimensional (2-D) cross section image (B-scan) of the tissue can be formed. If the whole construction is additionally moved in a direction perpendicular to the transversal direction, a full three dimensional (3-D) image volume can be imaged.

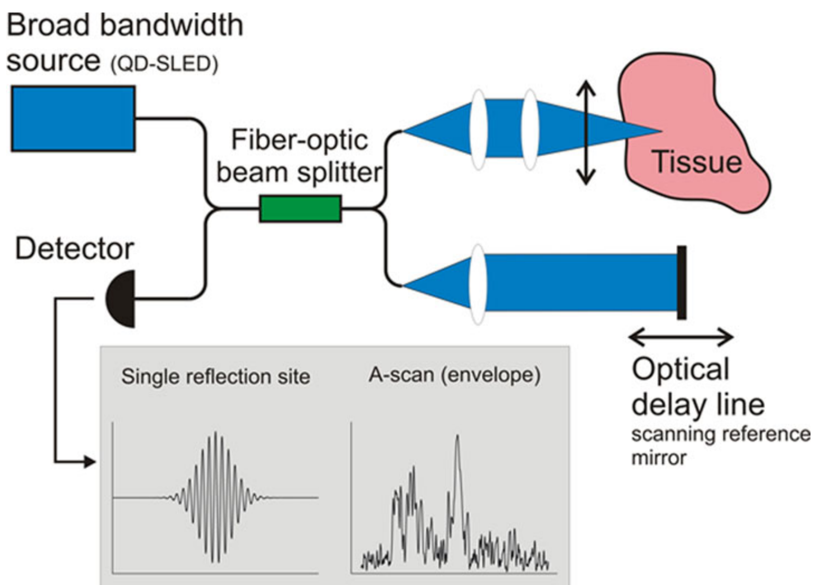

Figure 2.1 Standard OCT scheme based on a low-coherence time-domain Michelson interferometer [17].

The time delay is controlled by varying the position of the reference mirror and the constructive interference effects from two beams are observed at the output of the interferometer when the relative path length is changed during scanning of the reference mirror. If the light source has a long coherence length, the interference fringes will be observed for a wide range of relative path lengths of the reference and measurement arms.

In OCT imaging, it is necessary to measure precisely the absolute distance of the structures within the biological tissues. Thus, a short-coherence light (broad bandwidth) is used (shown in **Figure 2.2**).

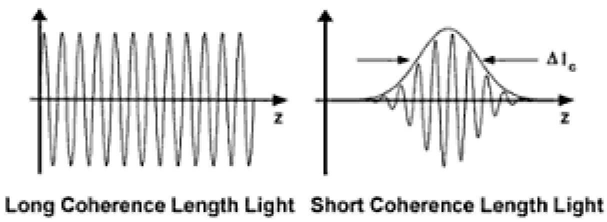

Figure 2.2 Examples of light source with long coherence length and short coherence length. The low-coherence light is desired for a Michelson-type interferometer to perform micrometer resolution measurements [10].

The coherence length Δl_c is a measure of the coherence and it is inversely proportional to the frequency bandwidth $\Delta\lambda$. For a Gaussian optical spectrum, the coherence length is presented by

$$\Delta l_c = \frac{2\ln(2)}{\pi}\frac{\lambda^2}{\Delta\lambda} \approx 0.44\frac{\lambda^2}{\Delta\lambda} \tag{2.1}$$

where λ is the mean (center) wavelength and $\Delta\lambda$ is the spectral width of the power spectrum [18]. The coherence length is normally measured from the full-width at half-maximum (FWHM) of the autocorrelation function (A-scan envelope). The axial resolution in OCT images is determined by the coherence length of the light source. In fact, one can prove that the axial resolution of an OCT system is proportional to the bandwidth of the light source, thus it is crucial to use sources with wide bandwidth (i.e. super luminescent diodes can provide bandwidth of 50-100 nm for ~1300 nm wavelength). In contrast to standard microscopy, e.g. confocal microscopy where the choice of wavelength is decided between desired wavelength and axial resolution, OCT can achieve fine axial resolution independent of the beam focusing and spot size. **Figure**

2.3 summarizes the relationship of axial resolution versus bandwidth for light sources at different wavelengths [19]. The transverse resolution is the same as in optical microscopy and it is determined by diffraction-limited spot size of the focused optical beam. The diffraction-limited spot size is inversely proportional to the numerical aperture (NA) of the beam.

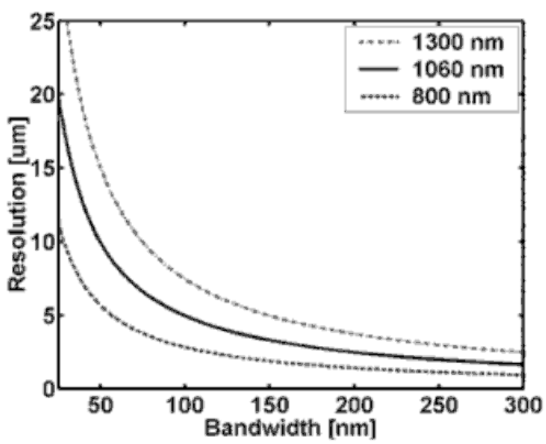

Figure 2.3 Axial resolutions versus bandwidth of the light sources for center wavelength of 800 nm, 1060 nm and 1300 nm. Micro-scale axial resolution requires extremely broad optical bandwidths. Bandwidth drastically increases for longer wavelength [19].

2.2 Dental Caries and OCT Signal Formation

2.2.1 Dental Caries

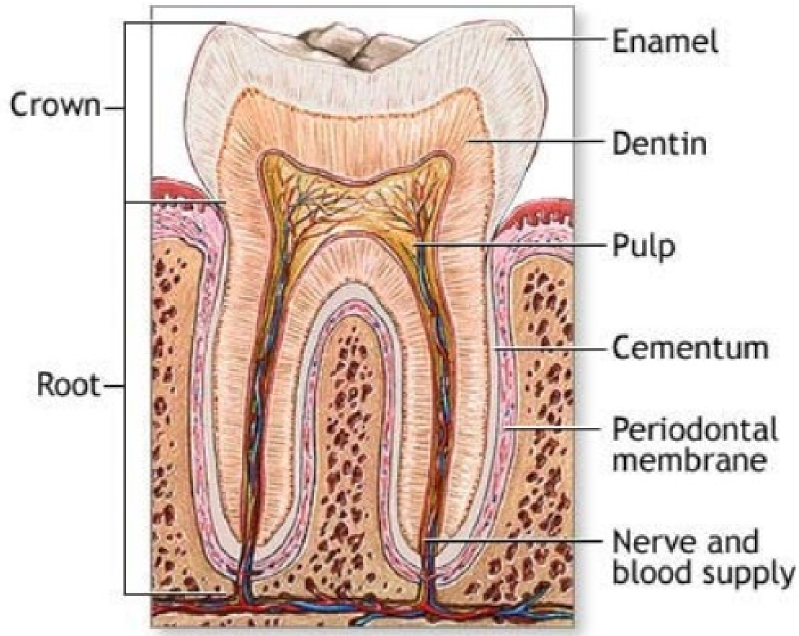

Figure 2.4 Schematic of tooth anatomy [20].

A cross section of a human tooth is shown in **Figure 2.4**. The crown is the part of the tooth that is visible above the gums. The root is the region of the tooth that is below the gums. The crown of each tooth has a coating of enamel, which protects the underlying dentin. The layers of tooth we are concerned with are the outmost enamel, the dentin, and the pulp. Enamel is the hardest substance in the human body. It gains its hardness from tightly packed rows of calcium and phosphorus crystals within a protein matrix structure. The enamel is organized into hard rods or prisms that are 4-6 μm in diameter, with glycoprotein prism sheaths 0.1-0.2 μm wide in between [21].

The major component of the inside of the tooth is dentin. This substance is slightly softer than enamel. It is elastic and compressible in contrast to the brittle nature of enamel. It also contains tubules throughout its structure that connect with the central nerve of the tooth within the pulp. The dentin-enamel junction (DEJ) constitutes a unique boundary between two highly mineralized tissues with very different matrix composition and physical properties. Enamel and dentin are believed to be linked by many parallel 80-120 nm diameter fibrils, which are inserted directly into the enamel mineral and also merge with the interwoven network of the dentin matrix.

Dental caries is a dynamic process that does not necessarily result in the formation of cavities. The tooth may undergo cycles of demineralization and remineralization. It is believed that the net loss of minerals will ultimately determine the extent of caries. The earliest changes are dissolution of the enamel leading to the pathways where diffusion can occur. If over a period of months to years, the surface weakens sufficiently then cavitations may result. Early lesions cannot be detected with current clinical detectable techniques due to lack of resolution. The possible clinically observable amount of caries is the white spot lesion, where demineralization has progressed to at least 300-500 μm. The white spot can be a reversible stage, and the lesion may ultimately revert to normal enamel.

2.2.2 Dental OCT Signal Formation

The use of light as a high resolution imaging tool in dental applications has been greatly compromised by the turbid nature of dental tissue. The average scattering and absorption properties have been recorded for both enamel and dentin. The average scattering coefficient is significantly affected by wavelength. In general, the shorter the wavelength, the greater the scattering coefficient is observed [22]. The amount of absorption in the near infrared is much lower compared to tissue absorption of light in visible region, where light absorption is greatly affected by electronic transition. Improved light penetration is achieved by performing imaging with light having an incident wavelength around 1310 nm. Absorption is low because this wavelength is too long to result in large amount of electron transition [23]. Conclusions can be drawn from these optical properties with respect to dental OCT imaging: longer wavelength sources should penetrate much further in enamel than shorter wavelengths and visible to near-infrared light should propagate much further through enamel than through dentin. These findings are consistent with OCT images features, where penetration depth in human tooth beyond 3 mm is not usual.

The OCT contrast or the reflected signal intensity is based on Fresnel reflection [24]: only at a depth of location where significant changes of the reflection index results in a consequence of changes in the return signal. A simple relationship can be governed by the equation:

$$R = \left(\frac{n_1 - n_2}{n_1 + n_2} \right)^2 \tag{2.2}$$

where n_1 and n_2 are the refractive indices of the media, and R is the reflectivity. Two light beams originate from the same source: reference field (Er) and sample field (Es) which are considered as time-variant fields. The sample field focuses on the tissue sample and the scattered sample field (Es') is reflected back and fed into the interferometer. If two beams (Er and Es') meet at a location within the coherence length, and the scattered field (Es') has traveled with extra time delay τ, where such delay is caused by the spatial and temporal properties of the sample, the resultant total field received at the photodetector is [23]

$$E(t) = E_r(t) + E_s^{'}(t + \tau) \tag{2.3}$$

The intensity of the combined light beam with interference can be expressed as,

$$I = \left|E(t)\right|^2 = I_r + I_s + 2\,\mathrm{Re}\left\langle E_r^*(t)E_s^{'}(t + \tau)\right\rangle \tag{2.4}$$

where I_r and I_s are mean intensity (dc value) returning from the reference and sample arms of the interferometer respectively, and $\mathrm{Re}\left\langle E_r^*(t)E_s^{'}(t + \tau)\right\rangle$ is the real part of the complex field. The interference signal can be analogously viewed as reflectivity profile mapping of the sample tissue [23]. A simple model of treating biological tissue is to regard them as small flat mirrors, however most hard or soft tissues are optically dense and differences in the refractive index can also cause the light to scatter at various angles. Thus such model does not conform well in practice. A single-backscattering model which describes the aspects of attenuation of a focused beam in tissue composed of particular scatters, has been adapted to the analysis of OCT [5], [25]. This model only accounts the scattering interactions either due to total loss of coherence (a full reflection) or no loss (a wide angle scatter cannot be detected by photo detectors). Two articles by Pan *et al* and Hellmuth *et al* have outlined the concept that OCT systems respond to the discontinuities of the refractive index structure on the scale of wavelength [26],[27]. In fact, the coherence "gate" behaves as an optical band-pass filter centered at $2\pi/\lambda$ (λ is the center wavelength), with a width set by the coherence length of the source. Overall, scattering is a relatively complex phenomenon which has its origin in refractive index mismatches. The intensity and angular dependence of scattering is determined by the size, position, and shape of the scatter relative to the wavelength of the incident light in addition to the index mismatch [28].

2.3 Dental OCT Images

Previously, Colston *et al* had firstly employed *in vitro* and *ex vivo* imaging of dental structures, where polarization-dependent backscattering might play an important role in dental OCT [29], [30]. Feldchtein *et al* have reported the imaging of hard and soft tissues containing oral mucosa, caries of a tooth, and dental restorative procedures [31]. Amaechi *et al* measured the reflectivity variation, induced by demineralization, for quantitatively assessing the dental caries lesion [32]. Wang *et al* has applied polarization-sensitive OCT (PS-OCT) for characterizing dentin and enamel, and Fried *et al* have also shown images of caries lesions and lesion progression with PS-OCT [33]. Brandenburg *et al* have imaged demineralized tissues, caries lesions, restored teeth, and oral mucosa [34]. The Spectroscopy group at the National Research Council of Canada – Institute of Biodignostics (NRC-IBD) reported *ex vivo* studies examining the correlation between morphological information provided by histological images and OCT images. This information is aided by Raman spectroscopy to assure the biochemical confirmation of the caries [35], [36]. Two OCT images of early stage dental caries are illustrated in **Figure 2.5**. Data were collected using a commercially available OCT system by Zeiss and a higher wavelength system built in house at the NRC-Industrial Materials Institute (NRC-IMI). Instrumentation details have been previously described in [37]. Some of two OCT system parameters are listed in **Table 2.1**.

Table 2.1 List of OCT systems used in this study.

	Galvanometer Imaging System (IMI)	Humphrey OCT-2000 Imaging System (Zeiss)
Central Wavelength	1310 nm	850 nm
Axial/depth resolution	12 μm	15 μm
Transverse/lateral resolution	24 μm	10-20 μm
Scan depth (in air)	4 mm	3 mm

Imaging was performed across the tooth surface using OCT probe. Images are acquired with image size of 500 x 100 pixels for 850 nm system and 2500 x 280 pixels or 3700 x 1800 pixels for 1310 nm system. Two photographs of extracted human molars cross-section obtained by destructive histological sectioning and light microscopy (**Figure 2.5 B** and **D**) along side are shown. Two non-destructive cross-section depth scans of human teeth are shown in **Figure 2.5 A** and **C**. The two-dimensional OCT image (B-scan) shows the light backscattered signals collected at the OCT detector and details the morphology of a carious lesion, and its surroundings. At 850 nm, most the data is obtained at the surface of the image. At 1310 nm, structural details identified deeper within the tissue, with the DEJ (dentin-enamel junction) line clearly identified. The regions of interest (ROIs) are manually delineated to demonstrate the comparison between OCT images and histology images.

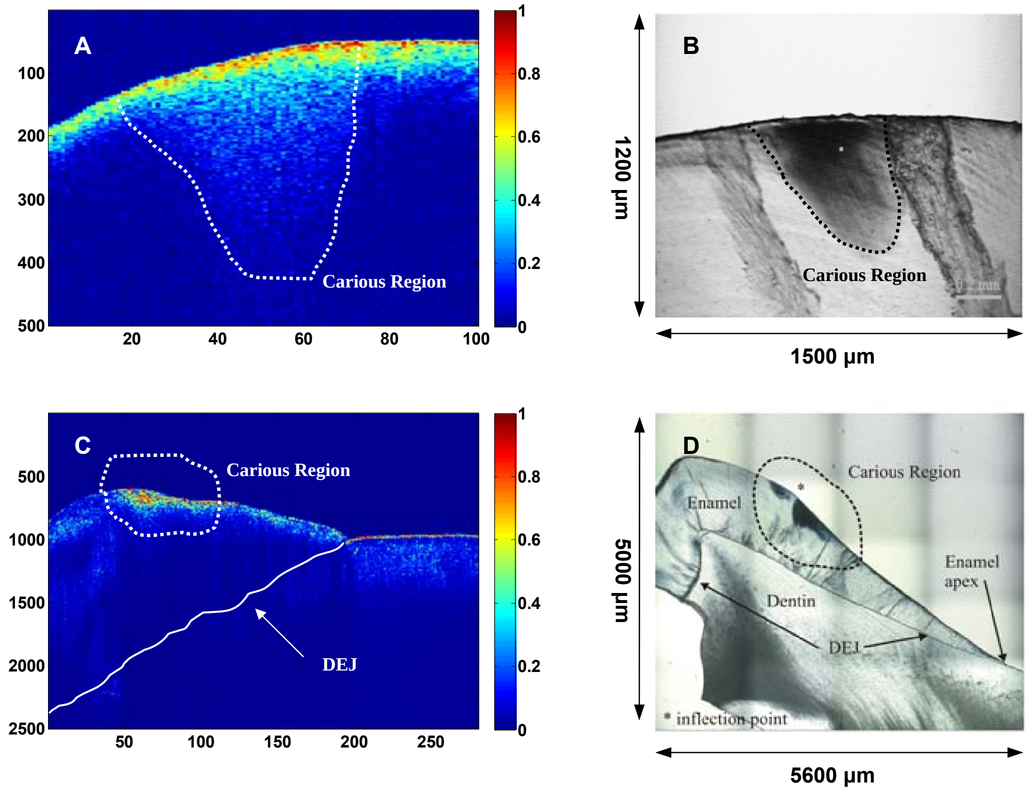

Figure 2.5 Influence of wavelength on penetration depth. In these four graphs, lesions are manually delineated. Images **A** and **C** are the cross-section depth scans. Images **B** and **D** are the cross-section images obtained by destructive histological sectioning and light microscopy. OCT imaging at 1310 nm (Image **C**) is demonstrated with higher resolution and greater penetration depth than imaging at 850 nm (Image **A**), where at 850 nm wavelength the DEJ can not be identified.

OCT images clearly are capable of identifying the suspicious carious lesion with greater speckle contrast compared to rest of the sound enamel. The advantage of OCT imaging at 1310 nm is also demonstrated with higher resolution and greater penetration depth than imaging at 850 nm, where at 850 nm wavelength the DEJ can not be identified. The actual size of 850 nm OCT images used in this study is 1.9 × 2 mm. For 1310 nm system, the axial resolution is 12 µm, and the transverse resolution is ~20 µm. **Figure 2.6 A** shows a 1310 nm OCT image of 5 × 8 mm in size, and **B** is 4 × 7 mm in size. Possible lesions in both images are indicated by circles.

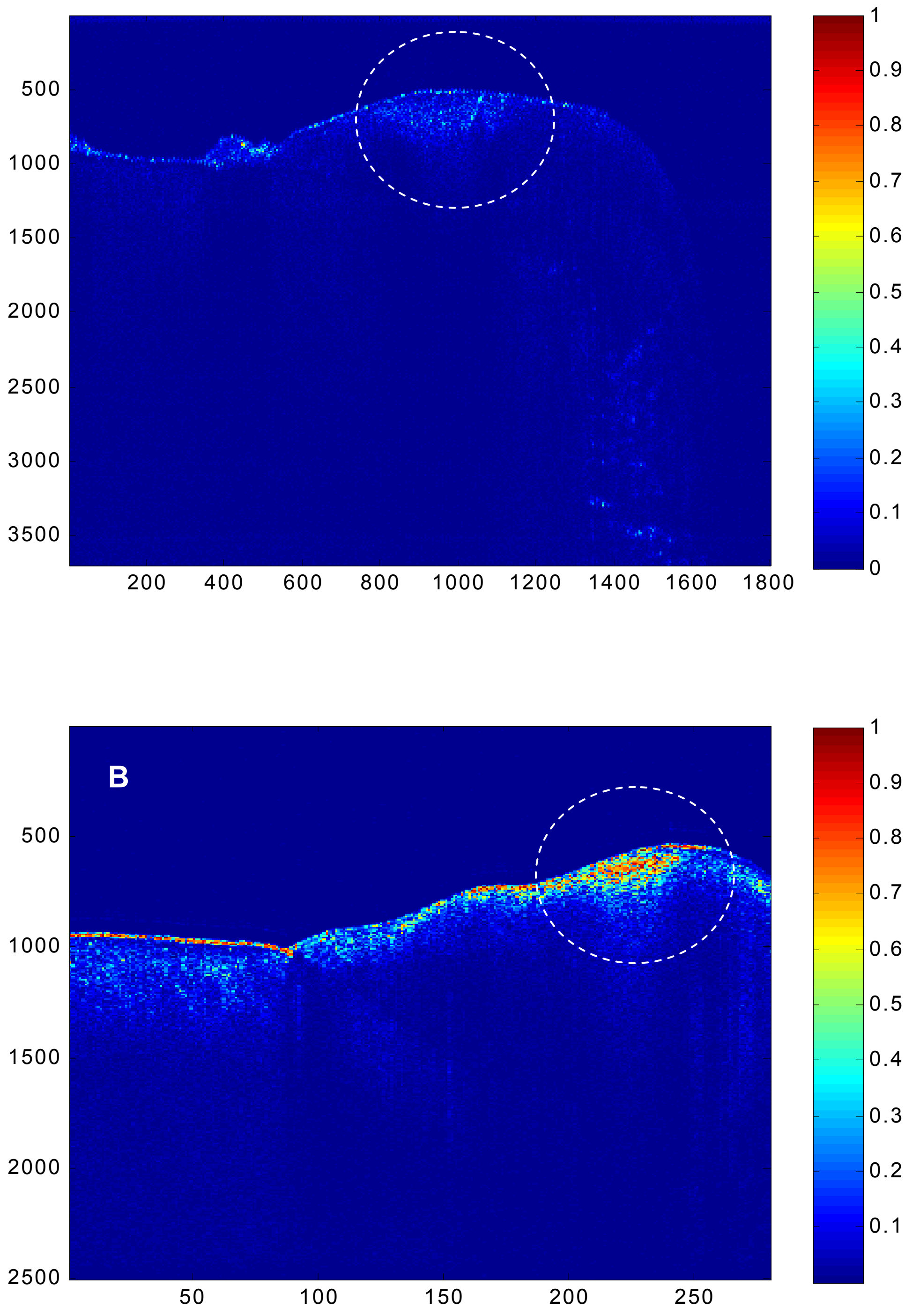

Figure 2.6 Two 1310 nm OCT images with different resolutions. **A**: 3700 x 1800 pixels (5 x 8 mm in size). **B**: 2500 x 280 pixels (4 x 7 mm in size).

Note that the OCT data in this study are direct measures of the backscattered signal without log-compression to reduce the dynamic range. The logarithm transformation results in compression of relative variations in signal, which might be or might not be desirable depending on applications. The direct display of the backscatter intensities on computer monitor in gray scale provides only 8-bits or 256 gray levels. The white level corresponds to the highest reflection or backscatter in the signal, and the black level corresponds to the weakest back reflection. In our case, the dynamic range of gray-scale image is very limited. In addition, the eye has a limited ability to differentiate gray levels with close similarities, so gray scale images do not faithfully represent the full dynamic range of information available in OCT images. This can be shown in **Figure 2.7**, when they are compared with **Figure 2.5**. To enhance the differentiation of different structure within the image, the images can be also displayed in a false color representation as seen in **Figure 2.5**. The highest back reflection or backscattering is displayed by red and yellow, whereas the lowest backscattering is represented by blue. The false color representation demonstrates the improvements in differentiation of different structures. However, the principle disadvantage of using false color display is that it can produce artifacts in the image. Thus normalization of signal levels is required. In addition, different signal levels in the image are mapped to different colors that do not necessarily correspond to different physical structures.

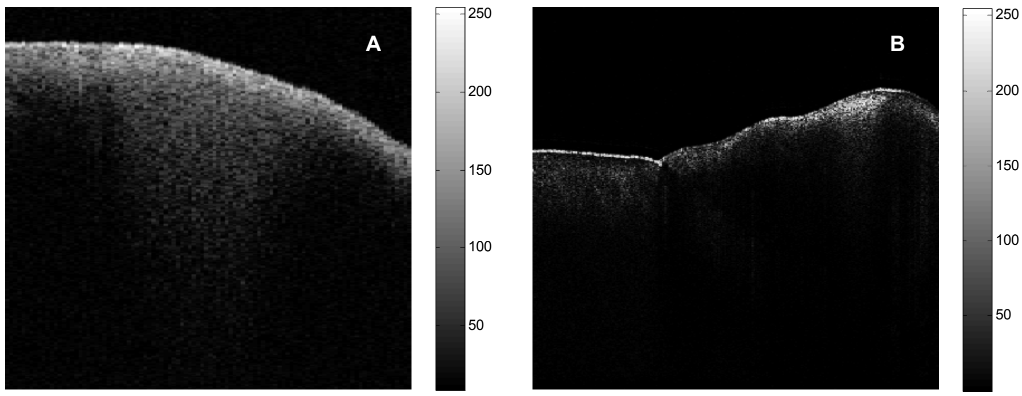

Figure 2.7 Same OCT images from **Figure 2.5 (A** and **B)** are displayed in 8-bit or 256 gray levels. The white level corresponds to the highest reflection or backscatter in the signal, and the black level corresponds to the weakest back reflection. The possible lesions are not visible when compared with false color representation.

Chapter 3

OCT Image Speckle Fundamentals

The significant portion of the image post-processing is speckle noise reduction. If the speckle reduction produces promising results, meaning that majority of the image features are preserved, then difficulties in many following processing procedures such as, edge detection, image segmentation, classification and image compression and registration are efficiently reduced. This chapter will first describe the OCT image speckle formation and speckle modeling (section 3.1 and section 3.2). As necessary steps prior to speckle suppression, some preliminary procedures like homophonic transformation (section 3.3) and image contrast enhancement (section 3.4) are introduced.

3.1 OCT Systematic Noise and Image Artifacts

The OCT system mainly consists of optical and electronics components, especially the detection unit. In addition, because factors such as variation in detector sensitivity, transmission and quantization error, temperature, components mismatch, etc. observational total noise still includes systematic noise signal. The systematic noise is unavoidable and can be treated as an additive noise (noise floor),

$$I_s^{meas} = I_s^{true} + I_{noise} \tag{3.1}$$

where I_s^{meas} is the measured signal and I_s^{true} is the "true signal". Since constant properties of the noise do not affect the qualitative properties of an OCT image, and assuming the noise to be of random nature, the time average of the noise must be zero. $E\langle I_{noise}\rangle = 0$.

An often used measure of noise is the root-mean-square (RMS) standard deviation, which can lead to a series of definitions like signal-to-noise ratio (SNR) and contrast to noise ratio (CNR). Thorough developments of the systematic noise models, including thermal noise, photon shot noise, amplifier noise, and filter noise have been extensively discussed in [38] and [39].

A common difficulty with the interpretation and analysis of OCT noise besides systematic noise and speckle noise is the artifacts. There are three types of primary image artifacts generally associated with any OCT images: motion, birefringence and echo. The motion artifacts can lead to a loss of spatial resolution in both the axial and transverse directions. Transverse motion error can occur during relatively long image acquisition times and lead to inaccuracies in the transverse resolution. The motion artifacts can be minimized by limiting the acquisition time to the order of few seconds. Tissue birefringence can occur in conventional OCT system, due to the polarization of light within the enamel, where refractive indices are different in the direction along the prism axis and direction perpendicular to the axis. One method for eliminating these artifacts is to use a polarization-sensitive OCT (PS-OCT) system. The last and potentially serious type of artifact is reflection echoes created by multiple reflection paths in the OCT interferometer. The strength of these echoes is proportional to the magnitude of the interface creating a specular reflection and is a function of source output power. One solution is to use imaging gel at the interface. The gel provides an index-matching medium that prevents overly bright specular reflections and eliminates artifacts.

3.2 Speckles in OCT Imaging

Speckle noise reduces image contrast and makes the boundaries between tissues difficult to resolve, especially in highly scattering tissues. Speckle noise gives a grainy and granular appearance to OCT images and has a negative effect on texture based analysis of carious lesions [40]. In addition to OCT imaging, speckles occur in other coherent imaging systems as well including synthetic aperture radar (SAR), medical ultrasound, and radio astronomy. Speckles arise as a result of a coherent superposition of constructively and destructively backscattered light waves sampled from different areas containing densely packed scattering particles.

Speckles significantly degrade image quality and complicate further image processing tasks, like image segmentation and edge detection. The nature of speckle has been a major subject of investigation. Schmitt *et al* investigated the origin and the formation of speckles together with their influence on OCT images, in which speckles play a dual role both as a noise source and as a carrier of information about tissue structure [23].

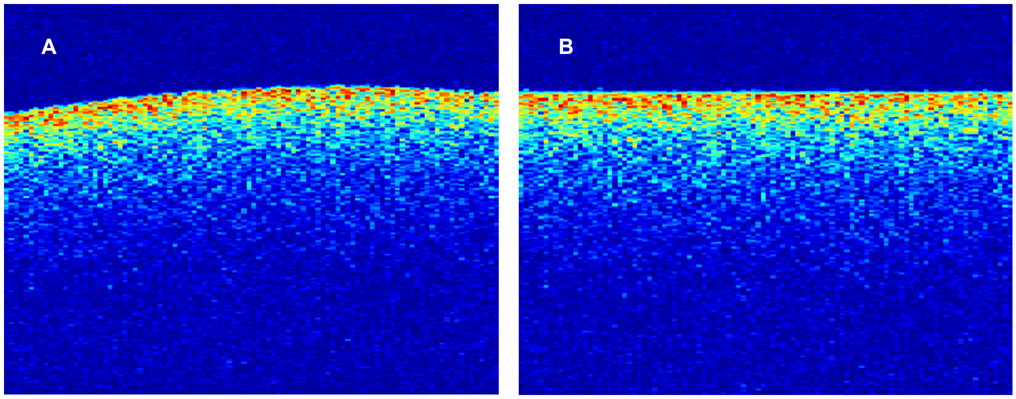

Figure 3.1 Example of an OCT image of a sound tooth (image of the air-tooth surface and enamel below) containing high-contrast speckle. The image is acquired at 850 nm. Image **A** is an example of an OCT image with strong backscatters below the air-tooth surface. A natural curvature of the air-tooth surface is straightened to demonstrate the transition of the speckle pattern below the surface (image **B**).

There are two types of speckle noise based on the methods of image formation. The first type involves the random phase variation of the wave front. This occurs when imaging through a turbulent medium. The second case involves the random interference of the various phases when they are scattered by microscopic fluctuation on the tissue surface. If the target's surface is very rough when compared to the optical wavelength of the laser, a fully developed speckle results [41]. This type of speckle is the most predominant in the OCT images and is usually treated as the result of uncorrelated backscatters.

Figure 3.1 shows an example of an OCT image with strong backscatter below the air-tooth surface. The appearance of the speckle has no obvious dependence on the depth, which suggests that the statistical properties of the OCT speckle are dominated by the effects of multiple scatters, rather than by phase aberrations incurred during the propagation through the dental hard tissue [42]. In addition to the optical properties (multiple scattering and phase aberrations), the speckle formation is also influenced by physical parameters of the imaging device: size and temporal coherence of the light source and the aperture of the detector [43]. Assuming the tissue sample has been imaged coarsely enough so that the degradation at any point can be assumed to be independent from all other points, the speckle can be modeled as multiplicative noise with univariate statistics. The intensity of the "zero-mean" symmetric Gaussian random variable obeys the negative exponential distribution [23]

$$p(I) = \frac{1}{\langle I \rangle} \exp\left(- \frac{I}{\langle I \rangle} \right) = \frac{1}{\sigma} \exp\left(- \frac{I}{\sigma} \right) \tag{3.2}$$

where $\langle I \rangle$ denotes the time average intensity of a homogeneous region (which equals to the standard deviation σ, $\sigma = \sqrt{\langle I^2 \rangle - \langle I \rangle^2}$). In denoising studies, it is often simplified that a logarithmical transformation converts multiplicative speckle noise into additive Gaussian noise [44]. It is also shown that this assumption is oversimplified, and a preprocessing procedure is proposed, which modifies the acquired images so that the noise in the log-transformation domain becomes close to Gaussian noise [45] (throughout this thesis I only applied the first assumption, the complicated model is left for future studies). The corresponding magnitude (square root of intensity) of full developed speckle is well modeled by a Rayleigh distribution [47]

$$p(A) = \frac{A}{\sigma^2} \exp\left(- \frac{A^2}{2\sigma^2} \right), \qquad A \geq 0 \tag{3.3}$$

where A is the amplitude factor and σ denotes the standard deviation of the random backscatter amplitude of the individual scatters. The ratio of the standard deviation to the mean produces a speckle contrast ($\frac{\sigma}{\langle A \rangle}$). The Rayleigh model proves to be a good model for the first-order statistics of OCT images as well [46], [47], even though under certain assumptions a Gaussian model holds [48]. An analytical model that describes the performance of OCT signals in both single and multiple scattering regimes has previously been presented [49], [50]. The symmetric Gaussian, the negative exponential, and the Rayleigh distributions are equivalent. They are applicable to the complex, intensity, and magnitude representation of the same data, with $\sigma = I/2$. To demonstrate this, the probability density function of a selected highly scattered region below air-tooth surface (assumed homogenous) together with its power and logarithmic transformations are shown in the figure below.

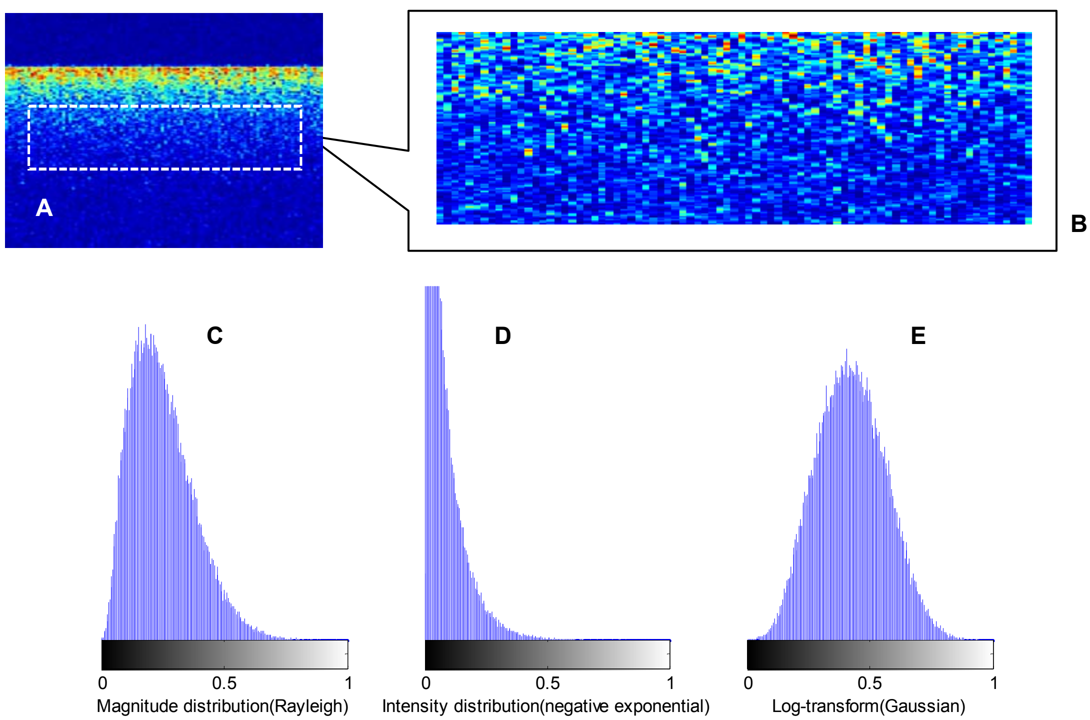

Figure 3.2 The histograms of an OCT image of a high-contrast speckle region. Image **A** is the original OCT image. Image **B** is the enlarged high-contrast speckle region. The intensity of the speckles distribution appears the have a Rayleigh-similar distribution (image **C**), and its square-power transformation follows a negative exponential distribution (Image **D**). The log-transform of the speckles then has become a Gaussian-like shape (image **E**).

Given the nature of speckle noise, speckle is conventionally modeled as a multiplicative noise, which provides us with a more sophisticated image noise model, adding multiplicative speckle noise to the observation [51].

$$f(x,y) = f_{true}(x,y) \cdot N(x,y) + W(x,y) \tag{3.4}$$

We replaced I (from equation 3.1) with function f corresponding to location coordinates (x, y) to give a spatial representation. The additive noise I_{noise} is also explicitly described as white noise with spatial variables (x, y). $f(x, y)$ is the noisy observation of the noise-free image $f_{true}(x, y)$. This model has been successfully used both in ultrasound and SAR imaging. Moreover, when applied to OCT images, only the multiplicative component N of the noise needs to be reckoned with, as the multiplicative noise is the dominant source of noise when compared with the additive noise. Thus the model from above equation can be simplified as,

$$f(x,y) = f_{true}(x,y) \cdot N(x,y) \tag{3.5}$$

There also exist alternative models for describing speckle noise as the additive noise, and some proposed the idea where the amplitude is proportional to the square root of the image. Equation 3.5 is more recognized as a general simplified expression for OCT speckle noise model.

3.3 Logarithmic Transformation

The combination of additive and multiplicative noise in OCT data makes direct processing of the OCT images a challenging task. A common approach to address this problem is to log-transform the observed data prior to processing. To understand the effects that log-transformation has on OCT data, we assume that the previously mentioned noise model is true, which is $f(x,y) = f_{true}(x,y) \cdot N(x,y) + W(x,y)$ (equation 3.4). The theoretical development of log-transformation was originated from the polarized light source model free of additive noise. Such light source obeys a Rayleigh distribution.

$$p(A) = \frac{A}{K^2} \exp\left(-\frac{A^2}{2K^2}\right), \qquad A \geq 0 \tag{3.6}$$

where A and K are simplified amplitude and constant factors, respectively. It can be shown that the probability density of the natural logarithm of the above distribution is [52],

$$p(\tilde{A}) = \frac{e^{2\tilde{A}}}{K^2} \exp\left(-\frac{e^{2\tilde{A}}}{2K^2}\right) \tag{3.7}$$

where $\tilde{A} = \ln(A)$. Though not exact, the distribution of $\tilde{A}$ can be reasonably approximated with a Gaussian distribution. Thus applying the log-transformation to an OCT image corrupted with speckle noise, converts the multiplicative noise N into additive Gaussian noise. To clearly state the transformation, the assumption here is that once a multiplicative model undergoes logarithmical transformation which converts multiplicative speckle noise into additive noise (the additive noise is mutually uncorrelated). Now let us consider the treatment for original additive noise. Let R denote the difference between the logarithm of the complete observation and logarithm of the simplified observation.

$$R = \ln\left(f_{true}(x,y) \cdot N(x,y) + W(x,y)\right) - \ln\left(f_{true}(x,y) \cdot N(x,y)\right) \tag{3.8}$$

Further numerical test has proven the difference R value is also well approximated by a Gaussian distribution [52]. This combined with the results for speckle only observation implies that $\ln\left(f_{true}(x,y)\cdot N(x,y)+W(x,y)\right)$ is reasonably well approximated by a signal ($\ln\left(f_{true}(x,y)\cdot N(x,y)\right)$) plus additive Gaussian noise (R) and when speckle is the dominant noise, as is often the case, the additive log-domain noise is zero mean. Therefore, one will model the logarithm of the observed OCT data as

$$\ln\left(f(x,y)\right)=\ln\left(f_{true}(x,y)\cdot N(x,y)+W(x,y)\right) \tag{3.9}$$

$$\begin{aligned}\ln\left(f(x,y)\right)&=\ln\left(f_{true}(x,y)\right)+G_{N,W}\\&\approx\ln\left(f_{true}(x,y)\right)+G_{N}\end{aligned} \tag{3.10}$$

where $G_{N,W}$ and G_N are zero-mean Gaussian noise that is independent of the noise-free signal and captures the total noise in the log-domain. G_N is an approximation of $G_{N,W}$ and $G_{N,W}$ is considered as the combined noise of $N(x,y)$ and $W(x,y)$ that is modeled as a general Gaussian. The assumed noise model and its log-transformation provide an estimate of the noise free signal and noise. In the context of speckle denoising, the aim is to estimate the log-domain signal $\ln\left(f_{true}(x,y)\right)$ given the log-domain observation $\ln\left(f(x,y)\right)$. After having approximated the completed OCT observation, we now have a general scheme that utilizes the noise model assumption.

3.4 Image Contrast Enhancement

A spatially varying refractive index continuum can accurately represent turbid biological medium such as tooth enamel and dentin. The light scattering strength and directionality depend on the gradient of the refractive index. As stated earlier in this chapter, we usually adopt a particle model of the tissue in which scatters are randomly distributed throughout the sample. The assumption is that speckle arises from the superposition of multiple scatters within the sample volume, rather than the effect of wave-front distortion that occurs in the propagating through the sample volume. Hillman [53] has demonstrated that the speckle contrast is correlated with the concentration of scatters in the OCT sample volume, which is in agreement with the random phasor model resulted from multiple backscatters. A recent study by Popescu [54] analyzes the difference in A-scan OCT signal attenuation between sound and carious enamel. Due to the process of demineralization creating pores in the carious enamel tissue, the OCT signal attenuates slower when compared with sound enamel. Another study by Li [55] has described the contrast ratio as being proportional to the detection depth and scattering coefficient of tissue and for the deeper layer, the contrast ratio approaches a constant. The histogram of the OCT image pixel intensities, which we have seen in **Figure 3.3**, roughly follows a negative exponential distribution. The majority of the image pixels are considered as dark background.

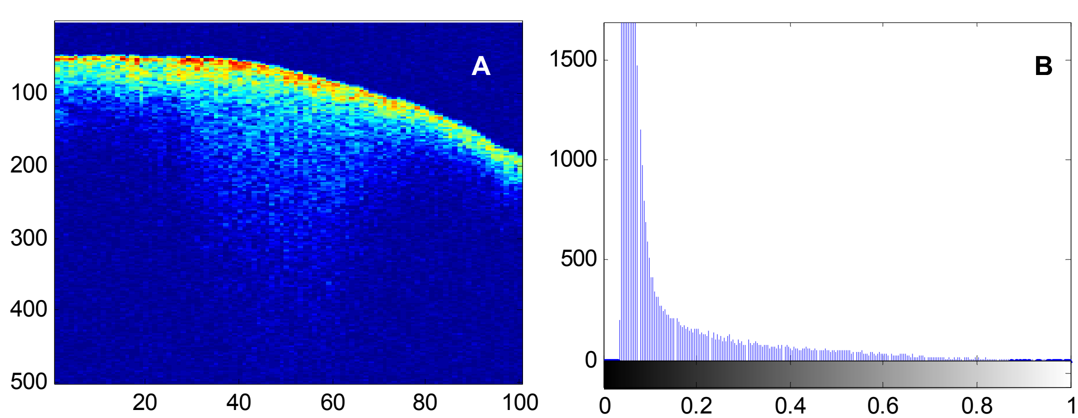

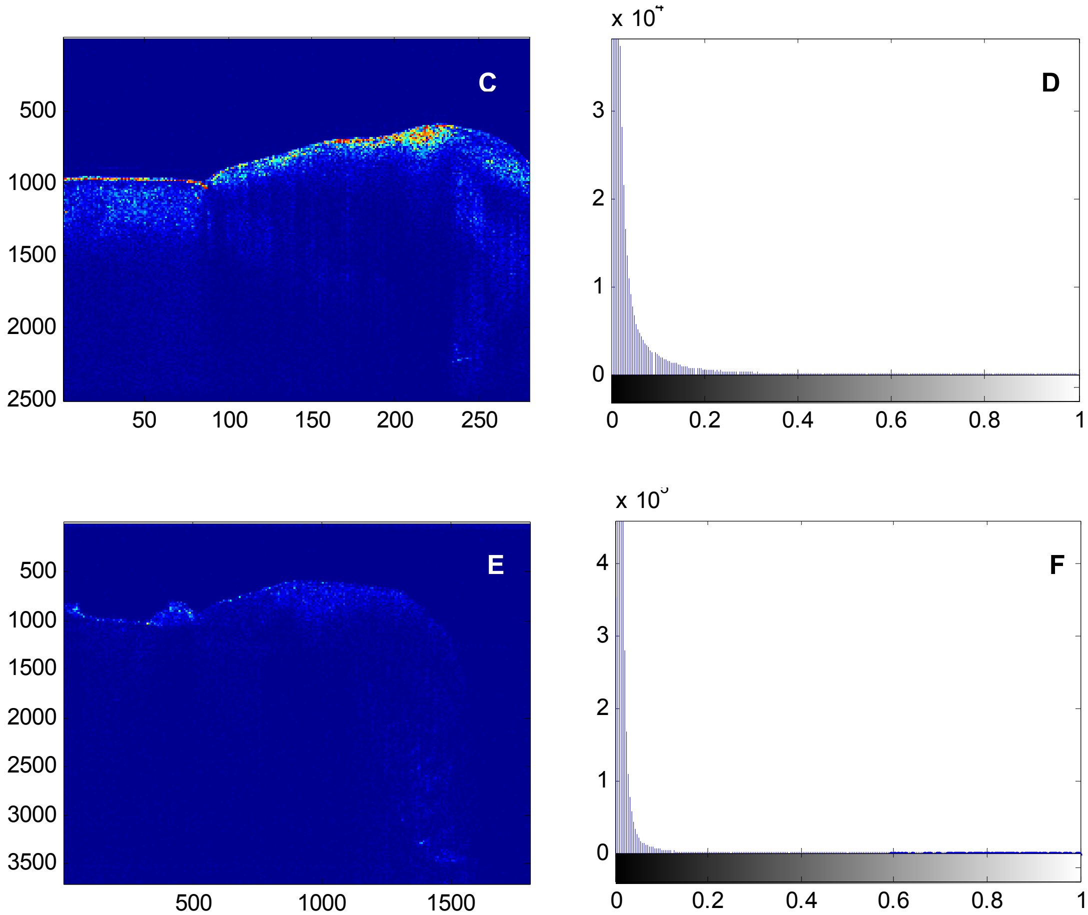

Figure 3.3 A is the original image acquired at 850 nm and **C** and **E** are acquired at 1310 nm center frequency. **B**, **D** and **F** are the histograms (probability density functions of the pixel intensities with respect to 16-bit grayscale levels) of the corresponding OCT images.

The task of image contrast enhancement here is to process an image so that the outcome is more suitable for lesion detection in terms of better contrast over the sound enamel surrounding it. In this investigation, only the spatial domain method is investigated, which deals with a direct manipulation of pixels in the raw image and also it is among the simplest of all images enhancement techniques. Some of the popular methods include linear transformation, log/power-law transformation, and histogram matching. Keeping in mind the multiplicative nature of speckle noise, some of these methods are not suitable for OCT image contrast enhancement. The characteristics of the speckle allow us to apply power/exponential operation to the raw image pixels without changing the nature of the speckle noise. Power-law transformation has the basic form,

$$f = c \cdot f^{\gamma} \tag{3.11}$$

where c and γ are positive constants. Through most of the operations, the constant c is chosen as 1, and the only tuning parameter is γ. The purpose of the power-law transformation is to increase the darker pixel intensities so that the ones with close similarities will likely cluster. And the results in the next chapter have proven to be so. However γ cannot be set to a small number, as it will amplify the background noise. A very simple way to look at the impact of such transformation is to substitute Equation 3.5 into Equation 3.11,

$$\begin{aligned} f(x,y) &= \left(f_{true}(x,y) \cdot N(x,y)\right)^{\gamma} \\ &= \left(f_{true}(x,y)\right)^{\gamma}\left(N(x,y)\right)^{\gamma} \end{aligned} \tag{3.12}$$

In case of log-transformation,

$$\begin{aligned} \ln\left[\left(f_{true}(x,y) \cdot N(x,y)\right)^{\gamma}\right] &= \gamma \cdot \ln\left[f_{true}(x,y)\right] + \gamma \cdot \ln\left[N(x,y)\right] \\ &= \gamma \cdot \ln\left[f_{true}(x,y)\right] + \gamma \cdot G_N \end{aligned} \tag{3.13}$$

From both cases, the speckle noise amplitude has been magnified, and it will affect the denoising outcomes later during the speckle denoising stage. However, the risk of introducing more noise is greatly compromised by the improvement in regional contrast. As image quality can be a subjective measure, the viewer is the ultimate judge. However, such subjective measure can be evaluated based on certain anatomical landmarks as references. The anatomical landmarks are three distinguishable regions in OCT images: strong backscatters in the carious region, high intensities in dentin and enamel region, and the dentin-enamel junction (DEJ). **Figure 3.4** displays four examples of carious and sound tooth images acquired at 1310nm to demonstrate the difference of image contrast. The top two images in have lower signal-to-noise ratio when compared with the bottom two images, resulting in less contrast in the carious lesion region. Also the DEJ lines are not as visible as the images from the second row. Ideally a layer of surface reflection with strong backscatters should be observable near the air-tooth surface. This is clearly evidenced by high intensity pixels shown near the surface from the second row images, whereas the images from the first row were not able to highlight some of the anatomical landmarks.

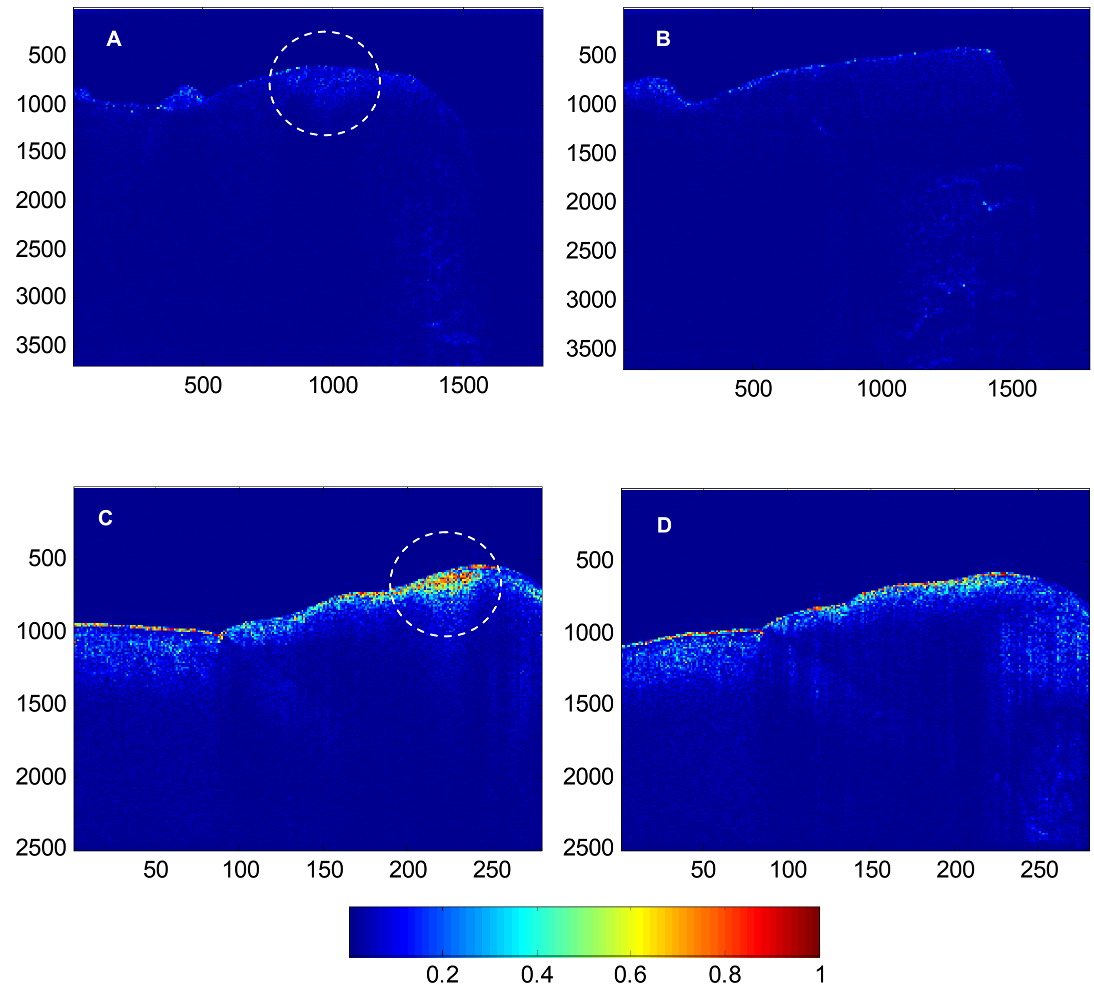

Figure 3.4 Original images acquired at 1310 nm. **A** and **B** are obtained with the same resolution settings (3700 x 2800 pixels). Images of **C** and **D** are measured using the same instrument settings (2500 x 280 pixels). Possible lesions are outlined by circles. Image **A** and **B** have less backscatter intensities, thus present less speckle contrast, and the lesion is more difficult to be indentified. The color bar represents the normalized backscattering intensities.

Speckle contrast is a measure of speckle characteristics, which is a direct assessment of the backscatters intensities. The speckle contrast is defined as the ratio of the mean intensity and standard deviation of the intensity fluctuation, and its value lies between 0 and 1. The speckle contrast is expressed by the following terms,

$$C = \frac{\mu_{ROI}}{\sigma_{ROI}} \tag{3.14}$$

where μ_{ROI} and σ_{ROI} are the mean value and standard deviation of the regions of interest (ROIs) respectively. Four regions are manually chosen to calculate the local speckle contrast: 1) background, 2) lesion area and 3) sound enamel and 4) dentin under surface area.

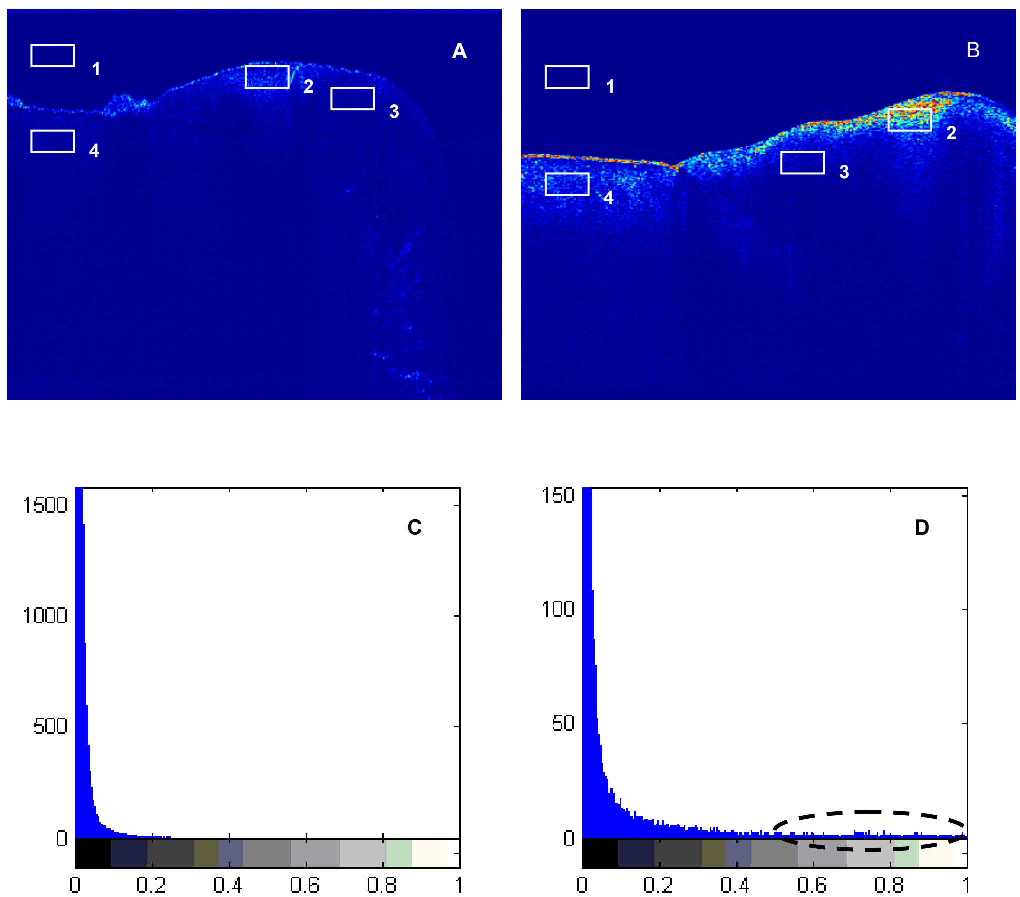

Figure 3.5 Four regions representing background, sound enamel, carious enamel and sound dentin (marked by boxes 1, 2, 3 and 4 respectively) are manually selected in two original OCT images (**A** and **B**) to compare the speckle contrast improvement after contrast stretching technique is applied. Images **C** and **D** show the difference in pixel intensity histograms (for the whole image) between two 1310 nm images acquired at different parameter settings. The highlighted region in **D** represents the high intensity pixels in the image.

The numerical values of these four local contrasts are listed in the **Table 3.1** below. The low value of "background contrast" in **Figure 3.5-B** image is possibly due to the low variance at the background and higher signal to noise ratio which gives a “sharper” look when it is compared with image in **Figure 3.5-A**.

Table 3.1 OCT image local speckle contrast.

	Image A	Image B
Background Contrast	*0.2396*	*0.0281*
Dentin Contrast	*0.0812*	*0.1976*
Lesion Contrast	*0.1870*	*0.1921*
Enamel Contrast	*0.1920*	*0.1904*

From the observation of histogram distributions of these two images one can conclude that the image in **Figure 3.5-B** is preferable, as the possible lesion region has strong backscatter (shown in higher pixel intensities in area “2” in **Figure 3.5-B**). This is due to the high intensity pixels located near the tail of the histogram distribution (**Figure 3.5-D**). In other words, the contrast in image **Figure 3.5-B** is better. To achieve the same effect on the “weakly” scattered image **Figure 3.5-A**, we apply a contrast stretching technique that re-maps the intensity range of [0, 0.5] from the original image to [0, 1] and then reconstruct the spatial distribution. The consequence of truncating the pixels located between [0.5, 1] and mapping them to a value “1”, is negligible since only less than 0.006% (455 out of 666000) pixels are saturated to maximum value. Therefore the positive result gives a more spread-out distribution over the original image (**Figure 3.5-A**) and it provides more contrast in the lesion area (shown in **Figure 3.6**).

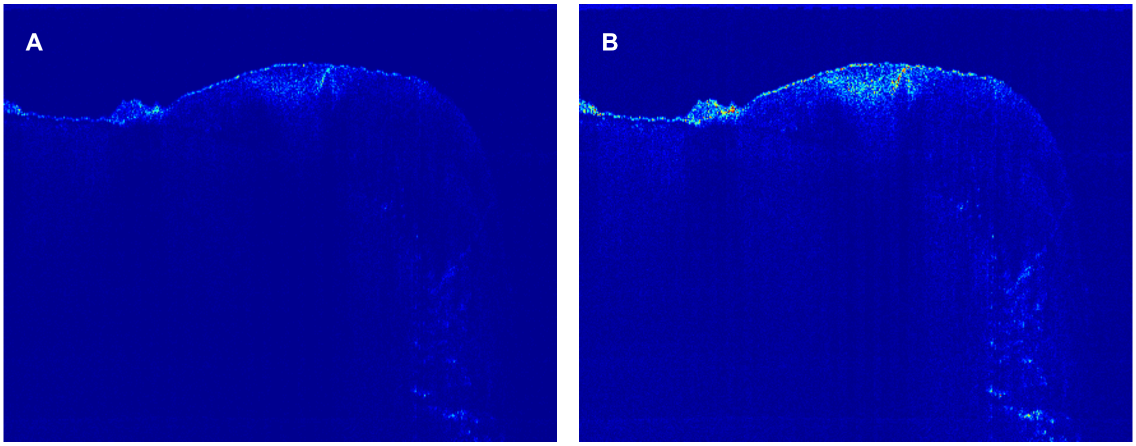

Figure 3.6 Images **A** is the original OCT image and image **B** is obtained after contrast stretching operation. The visual improvement can be easily noticed in image **B**. The lesion area is observed to have more back scatters with higher intensity. This is the result of saturating the pixels that have intensity between 0.5 and 1 to the maximum value of the image.

The numerical results are shown in the **Table 3.2**. The contrast stretching operation does not change the homogeneity of the following three regions: background, dentin and enamel. It only adjusts the lesion contrast, which is helpful in caries visualization. The resulting higher contrast in the lesion area is possibly due to the fact that high intensity backscatters with intensities between [0.5, 1] are mostly located in the lesion region. The contrast stretching only amplifies the contrast in that region locally.

Table 3.2 OCT image local speckle contrast comparison.

	Before Stretching	*After Stretching*
Background Contrast	*0.2396*	*0.2396*
Dentin Contrast	*0.0812*	*0.0812*
Lesion Contrast	*0.1870*	*0.1781*
Enamel Contrast	*0.1920*	*0.1920*

The power-law transformation is implemented after the contrast stretching step. The parameter γ in Equation 3.11 is experimentally set between 0.7-0.8. This is chosen to achieve a balance between noise amplification and visual separation of the lesion. One set of two 1310 nm OCT images (one with carious enamel and one with sound enamel) are compared after contrast stretching and power-law transformation in the **Figure 3.7**.

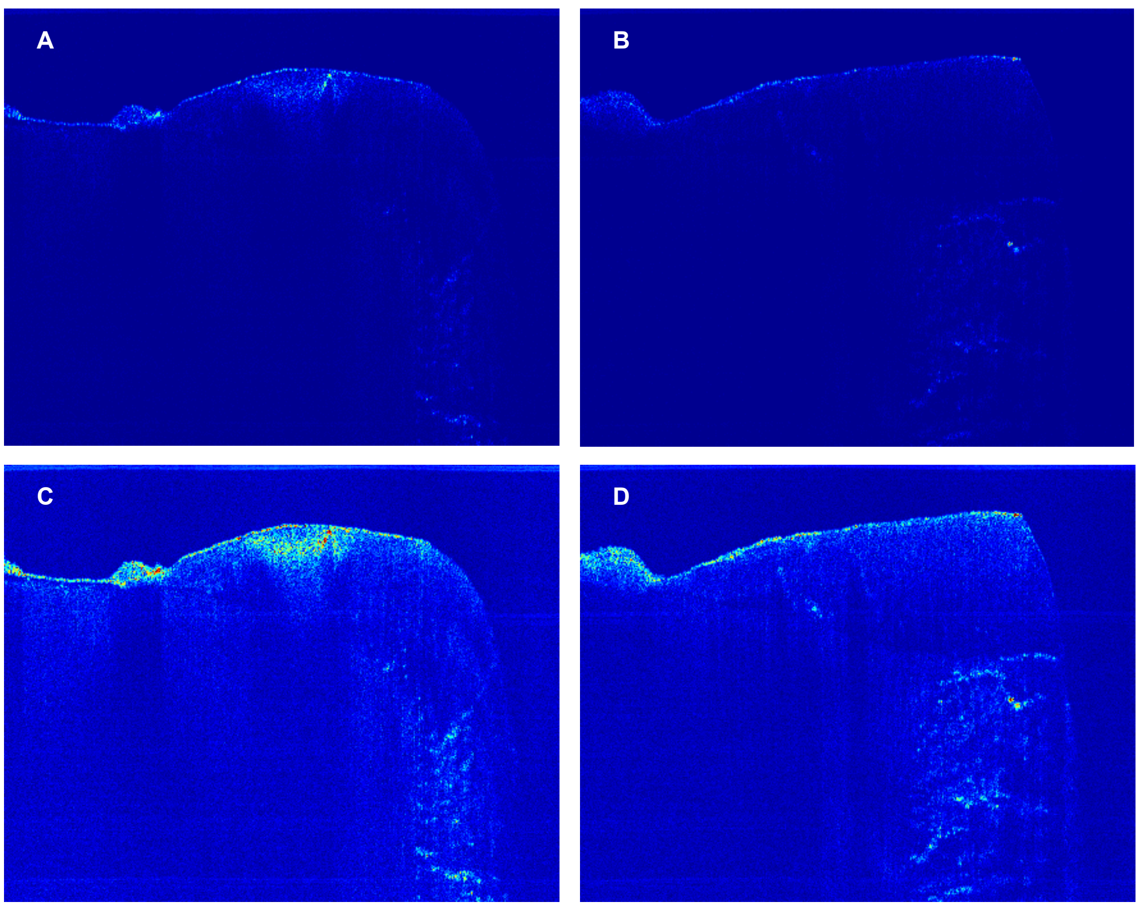

Figure 3.7 Two original 1310 nm images **A** and **B** with carious enamel and sound enamel respectively. Images **C** and **D** are the obtained by contrast stretching and power-law transformation. The visual improvement is subjected to three landmark areas: carious lesion, below surface dentin/enamel intensity and DEJ line, where these three areas are not easily visible from the original images.

Based on the visual examination of landmark regions (carious lesion, sound enamel/dentin and DEJ line), the enhancement in enamel below the air-tooth surface and the contrast between carious and sound enamel are both easily visualized. The contrast enhancement will also play an important role in speckle reduction later on to be mentioned in the next chapter.

Now we will look at how the contrast enhancement on OCT images has affected the pixel intensity histogram index (HI) and the nature of the probability distribution. Similar to foregoing steps, three representative regions are selected: carious enamel, sound enamel and background. They are corresponding to boxes 1, 3 and 4 in **Figure 3.5**. Ideally, a group of pixels with similar characteristics (usually within assumed homogenous region) will cluster based on their similarity in the statistical distribution. And the clustering result is improved, as the variance of each distribution (assumed Rayleigh distribution, thus the variance is the deterministic parameter) will also be increased and therefore the shape of sample distribution is distinguishable. **Figure 3.8** illustrates the histogram distributions at selected locations before and after the non-linear contract enhancement. At each image, the pixel histogram distributions of a group of two areas (background and caries, or enamel and caries) are plotted in the same graph with different colors to separate the distribution patterns.

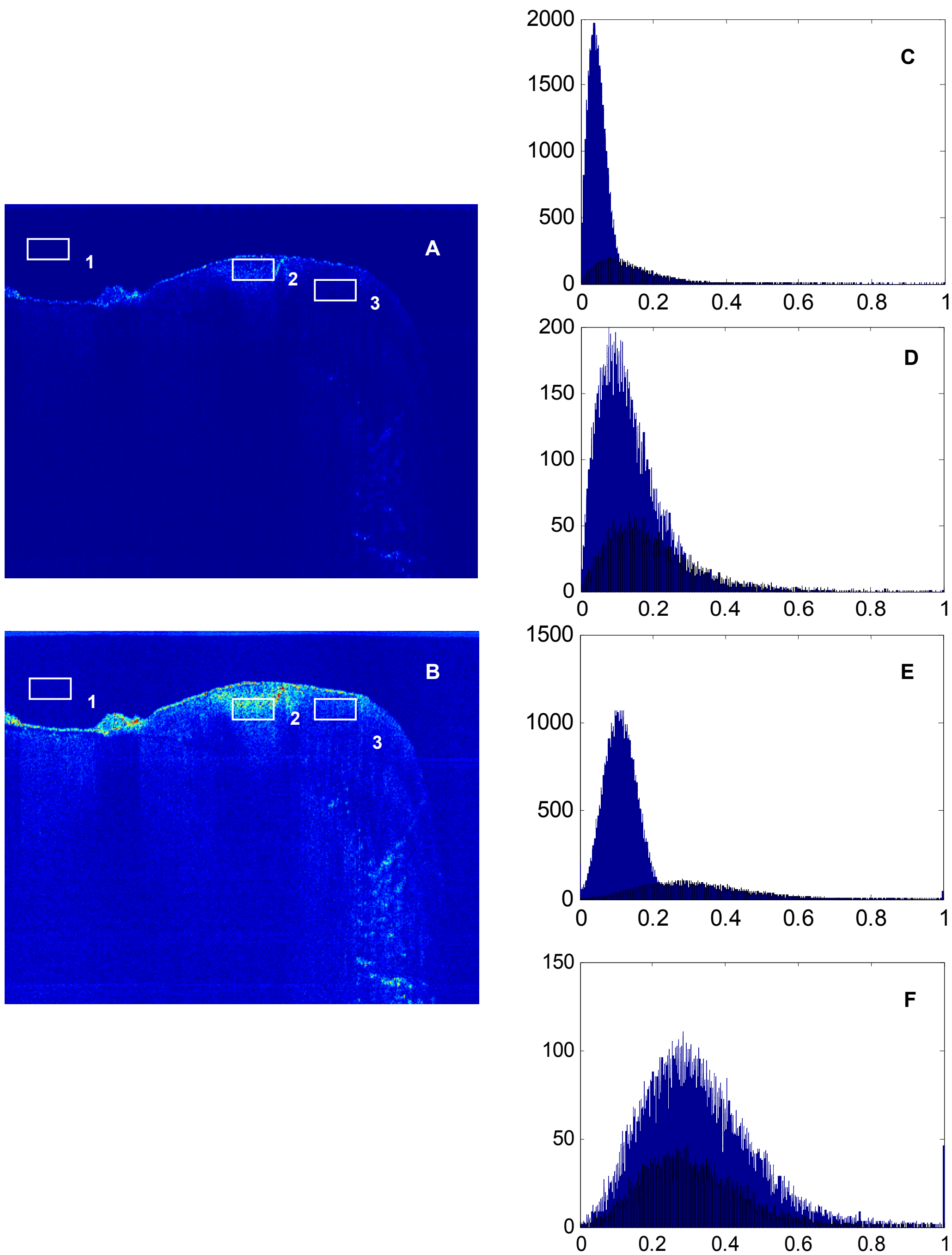

Figure 3.8 Three regions are selected from two images (**A** and **B**) and histogram distributions from three sampled regions are calculated to compare the normalized histogram distribution patterns before and after contrast enhancement. Plot **C** is the histogram distributions of region 1 (blue) and 2 (black) fitted in one graph. Similarly, plot **D** is a graph of region 2 (blue) and 3 (black) from image **A**. Plots **E** and **F** are generated from image **B**. Plot **E** is generated from region 1 (blue) and 2 (black). And plot **F** is generated from region 2 (blue) and 3 (black).

The distinctive sampled histogram distribution patterns provide some unique features to characterize the homogenous regions statistically. A second order statistics will provide sufficient information to separate lesion areas from its surroundings. We selectively compare the histogram distributions between background and lesion, and sound enamel and lesion, as carious lesion normally borders with background and rest of sound enamel. Once we can focus on this small region and manage to parameterize these three assumed homogenous entities, the following segmentation work becomes trivial.

Chapter 4

OCT Speckle Reduction and Image Restoration Techniques

Techniques of digital image processing have been extensively developed in many mathematical models, thus the choice of terms is quite deliberate. For the purpose of this investigation, some of the common definitions are restated for clarity. "Observed image" refers to general OCT data that is acquired and measured from the OCT imaging system. The "estimated image" denotes the estimated solution through image reconstruction and the "true image" denotes the original image or the underlying true image giving rise to the "observed image". In case of possible ambiguity, "image model" is used to describe the estimated prior knowledge about the "true image". This chapter begins with a brief review of existing speckle reduction techniques, followed by some general discussion of the mathematical preliminaries related to each technique. The numerical results are tested with Signal-to-Noise Ratio (SNR), Contrast-to-Speckle Ratio (CSR) and Equivalent Number of Looks (ENL). Two categories of speckle reduction techniques are detailed in this study: 1) single resolution (spatial domain) and 2) multi-resolution (wavelet-transform domain). Some numerical results on representative images are provided.

4.1 Review of OCT Speckle Reduction Techniques

OCT image restoration can be a difficult task because of the substantial contamination of the speckle noise in the image, yielding only minor trace of the desired data. Many approaches towards speckle reduction in OCT images have been based on two classes of techniques: employing some form of spatial/frequency compounding (polarization, frequency, spatial diversity) [23], or image restoration techniques (image post-processing methods). The first category is based on modifications to the OCT system design and speckle reduction occurs during the image acquisition stage. The latter category is based on numerical image processing algorithms, and is considered as image post-processing.

With OCT being an optical analog to medical ultrasound and synthetic-aperture radar (SAR), many speckle reduction techniques are similar to those employed in the fields of medical imaging and remote sensing, where extensive research has been devoted to speckle reduction in these two areas. In this chapter, some of the speckle reduction techniques in OCT are first reviewed. A few of the earlier techniques includes ZAP (zero adjustment procedure) [56] and CLEAN (originally proposed by Jan Hogborn) [57] algorithms, based on iterative deconvolution that were developed originally for use in radio astronomy. Standard adaptive spatial filters such as the Lee [58], Kuan [59], and Frost [60] filters, which use the second order statistics within a minimum mean squared error estimation approach and based on a multiplicative speckle model, have widely been used to reduce speckle in SAR, ultrasound and OCT images. A comparative analysis of these and related filters is presented in [61]. More recent speckle filters in the image domain such as the enhanced Lee and enhanced Frost filters [62], are implemented in combination with a preliminary classification knowledge about the texture of the images. Rotating Kernel Transformation (RKT), another adaptive speckle suppression filter has been applied to coronary OCT images [63]. Filtering techniques based on the RKT can produce good contrast enhancement of image features, but they also result in significant edge blurring when strong noise reduction is required. Anisotropic diffusion (AD) filter is another type of noise reduction algorithm that has been previously applied for speckle noise reduction in OCT images. The performance of two variations of the AD algorithm was compared in reference [64]. The main problem with any image processing algorithm based on AD is the large number of iterations necessary to reach a steady state solution. Also some results have shown that for images with large noise components, AD will have no significant effect [65].

The use of multi-resolution (wavelet-based) techniques has been recently reported by several groups with promising results [66] [67]. The approaches take into account the signal and noise properties in spatial and frequency domain. Several representative wavelet denoising methods for OCT range from thresholding to vector based minimum mean squared error estimation. Some notable examples of wavelet based OCT noise reduction include the optimal non-linear wavelet thresholding method [67], originally developed for ultrasound [68], which applies soft-thresholding, with image dependent and sub-band dependent thresholds and multi-dimensional method [69], which processes multiple OCT image slices by making use of both spatial and temporal correlations.

4.2 Evaluation Matrices

Image denoising can be an objective process, as one can control the image outcome in order to achieve the psychological satisfaction by the human visual system.

Whereas on the other hand, one cannot promise such procedure will yield an optimal estimation of the desired result in the absence of a true reference (original image). Therefore, there are no absolute subjective measures or criteria of image restoration quality to provide reliable standards consistent with human perception. Only tolerable qualitative measures are being regularly used. Filter performance was compared using established evaluation measures, including Root Mean Squared Error (RMSE), Peak Signal-to-Noise Ratio (PSNR), Signal-to-Noise Ratio (SNR) and Contrast-to-Speckle Ratio (CSR). However, all these measures only partly cover the visual quality. The visual quality of an image is difficult to define with mathematical precision, since it is dependent on the properties of our visual system. We know, for example, that our visual system is more tolerant to a certain amount of noise than to a reduced sharpness. On the other hand our eyes are very sensitive to certain specific artifacts. Unintended artifacts may give rise to a wrong interpretation of the image, which may lead to a faulty diagnosis. Also in judging the performance of a speckle suppression technique and comparing speckle suppression techniques, aspects that evaluate visual performance are: the ability to retain small details and preserve edges, i.e., sudden transitions in gray level or texture, and gradual changes in grey level.

The first evaluation method is the basic SNR which is a quantitative measure of the noise suppression ability. It measures the variation in the speckle of the image and is defined as

$$
\begin{aligned}
SNR &= 20 \cdot \log\left(\frac{\sqrt{\sum f(x,y)^2}}{\sqrt{\sum\left[f(x,y) - \widehat{f}(x,y)\right]^2}} \right) \\
&= 20 \cdot \log\left(\frac{\sqrt{\sum f(x,y)^2}}{RMSE} \right)
\end{aligned}
\tag{4.1}
$$

where the top part of the fraction describes the square root power sum of each pixel (x and y represent the position of each pixel within the image) from the original OCT image and the denominator is the Root Mean Square Error (RMSE) between the observed image $f(x,y)$ and image after speckle filtering $\widehat{f}(x,y)$.s While this metric is intuitive and widely used, it does not always provide an accurate visual display of image quality. Another similar image quality measure is the Peak Signal-to-Noise Ratio (PSNR) [70], and this measure is defined by

$$
PSNR = 20 \cdot \log\left(\frac{255}{RMSE} \right) \tag{4.2}
$$

where 255 is the maximum pixel value for a standard 8-bit per pixel gray scale image.

Contrast-to-Speckle Ratio (CSR), also generally known as Contrast-to-Noise Ratio (CNR), is another quantity measure that assesses image quality [23]. It describes the ability to perceive a target from the background region. CSR is defined as

$$
CSR = 20 \cdot \log\left(\frac{\left|\mu_{ROI} - \mu_{background}\right|}{\sqrt{\sigma_{ROI}^2 + \sigma_{background}^2}} \right) \tag{4.3}
$$

where $\mu_{background}$ and μ_{ROI} are the mean brightness of the background and the ROI and $\sigma_{background}^2$ and σ_{ROI}^2 are the variance of background and ROI, respectively. The *CSR* is a distortion measure that predicts image integrity. This *CSR* is a more robust measure compared to *SNR* as it employs the contrast that perceptually is convenient for humans to detect pattern differences. The above measures are assumed theoretically correct upon the condition that the ROI under investigation is homogenously distributed, whereas the actual calculation of a scattering region is the result of compounding multiple A-scans, containing statistical isotropically distributed scatters of one dimension. However, certain assumptions about tissue homogeneity may not be true in reality.

Another commonly used measure for speckle suppression is the Equivalent Number of Looks (ENL), which measures smoothness in the areas that should appear homogenous, but are corrupted by speckle [71]. For an OCT image, we calculate this value only in highly scattered region. The reason for this is that only within the region below the tooth-air surface we can assume that the ideal intensity should be homogenous. Hence we evaluate

$$ENL = 10 \cdot \log\left(\frac{\mu_{ROI}^2}{\sigma_{ROI}^2}\right) \tag{4.4}$$

where μ_{ROI} and σ_{ROI} denote mean value and variance of the regions with high intensity backscatters, respectively. This is also generally referred to as a different form of speckle contrast. A large ENL indicates a stronger speckle smoothing in the corresponding region.

The Structural Similarity Index Matrix (SSIM) is a method for measuring the similarity between two images [72]. The SSIM index is a full reference metric, in other words, the measuring of image quality based on an initial image as reference. SSIM is designed to improve on traditional methods like PSNR and RMSE, which have been shown to be inconsistent with human eye perception [72]. The SSIM metric is calculated on various windows of an image.

$$SSIM = \frac{\left(2\mu_f \mu_{\hat{f}} + c_1\right)\left(2\sigma_{f\hat{f}} + c_2\right)}{\left(\mu_f^2 + \mu_{\hat{f}}^2 + c_1\right)\left(\sigma_f^2 + \sigma_{\hat{f}}^2 + c_2\right)} \tag{4.5}$$

where μ_f and $\mu_{\hat{f}}$ are the mean intensities of the original image and filtered image respectively. σ_f and $\sigma_{\hat{f}}$ are the standard deviations of the original image and estimated image respectively. $\sigma_{f\hat{f}}$ is the covariance matrix. $c_1 = (k_1 L)^2$ and $c_2 = (k_2 L)^2$ are two variables stabilizing the equation. The default values for L is 256, for $k_1 = 0.01$ and for $k_2 = 0.03$ are by default. The resultant SSIM index is a decimal value between -1 and 1, and the value 1 is only reachable in the case of two identical sets of data. Typically it is calculated on window sizes of 8×8.

4.3 Adaptive Spatial Filtering

In this category, the image processing function in the spatial domain can be expressed as

$$\hat{f}(x, y) = T\{f(x, y)\} \tag{4.6}$$

where the original image is defined as a two dimensional function $f(x, y)$, with x and y the spatial coordinates, $\hat{f}(x, y)$ is the estimated image after the transform, and T is the transformation function. The amplitude of f and $\hat{f}$ at any pair of coordinates (x, y) is the intensity or grey level of the image at that point. Speckle spatial filtering consists of moving a kernel over each pixel in the image and applying a mathematical calculation using the pixel values under the kernel and replacing the central pixel with the calculated value.

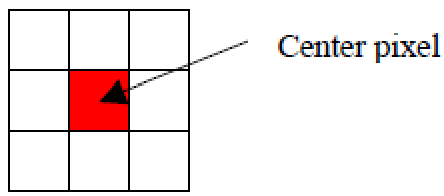

Figure 4.1 A simple 3 x 3 kernel is shown with a center pixel indicated in red.

The kernel is moved along the image one pixel at a time until the entire image has been covered. The visual appearance of the speckle reduction is achieved by applying various levels of a smoothing filter. We start by introducing some the simplest form of speckle smoothing filters. The typical size of the filter window can range from 3 × 3 to 33 × 33, with the size of the window is considered odd, in most cases. A larger filter window means that a larger area of the image can be used for calculation and possibly requires more computation time depending on the complexity of the filter algorithm. If the size of the filter window is too large, the important details will be lost due to over smoothing. On the other hand, if the size of the filter window is too small, speckle reduction may not be very effective. During numerical tests, a 7 × 7 or a 9 × 9 filter window usually yields the best results, but sometime, we can be more conserved with choosing the size of the kernel, thus on large images with finer details, a 5 × 5 filters were also applied.

Mean filter actually does not remove the speckles but averages them into the data. As speckle noise appears as a high frequency component in the OCT image, the mean filter, a widely-used low-pass filter, can be used for speckle suppression purposes. Generally this method results in loss of details and resolution. However, it can be used for applications where resolution is not the first concern. In mean filtering, the center pixel of the kernel is calculated through a mean value in a local neighborhood. The value of the estimated image $\hat{f}(x,y)$ at any point (x,y) is simply the arithmetic mean computed using the pixels within the moving window. In other words,

$$\hat{f}(x,y) = mean\{f(m,n)\},\ m,n \in S_{xy} \tag{4.7}$$

where S_{xy} is the sub-image, or in this case, the moving window/kernel. m and n are the defining parameters for the size of the window. The mean filter has the property of locally reducing the variance thus reducing the SNR and it requires the user to specify only the size of the window. However it has the effect of potentially blurring the image.

For **median filter** instead of calculating the center pixel value with the mean value of the neighboring pixels, it simply computes the median value in the area encompassed by the filter,

$$\hat{f}(x,y) = median\{f(m,n)\},\ m,n \in S_{xy} \tag{4.8}$$

One can think that the low-value and high-value pixels correspond to destructive and constructive speckles. Thus the median filter can be used for such erratic variations. Median filtering also works really well for random distributed noise, such as salt and pepper and spike noises. The conventional median filter does not shift edges and therefore results in fewer artifacts near the boundary of different objects in the image.

Lee filter utilizes the statistical distribution of the pixel values within the moving kernel to estimate the value of the center pixel. The noise model is assumed to be a multiplicative Gaussian. The Lee filter is based on the assumption that the mean and variance of the center pixel is equal to the local mean and variance of all the pixels within the moving kernel [73].

$$\hat{f}(m,n) = mean\{S_{mn}\} + K\left[f(m,n) - mean\{S_{mn}\}\right] \tag{4.9}$$

where S_{mn} is a kernel window of size *m* by *n* pixels. The statistical values associated with S_{mn} are computed at the center pixel. An estimator of $\hat{f}(x,y)$ is obtained by minimizing either the mean square error or the weighted least square estimation. *K* is calculated as:

$$K = \frac{(std\{S_{mn}\})^2}{[mean\{S_{mn}\}]^2 \sigma_f^2 + (std\{S_{mn}\})^2} \tag{4.10}$$

The Lee filter is based on the approach that if the variance over an area is low or constant, then the smoothing will be performed. Otherwise, if the variance is high (e.g. near edges), smoothing will not be performed. If there is no smoothing, the filter will output only the mean intensity value of the filter window. Otherwise, the difference between center pixel and original image is calculated and multiplied with a weighting function and then summed with the original image [73].

Kuan filter is very similar to the Lee filter. It does not make an approximation on the noise variance within the filter window. The Kuan filter simply models the multiplicative model of speckle into an additive linear form, but it relies on the ENL from an image to determine a different weighting function to perform the filtering [74],

$$K = \frac{\dfrac{std\{S_{mn}\}}{mean\{S_{mn}\}} - \dfrac{\sigma_f}{\mu_f}}{\left(1 + \dfrac{\sigma_f}{\mu_f}\right)\dfrac{std\{S_{mn}\}}{mean\{S_{mn}\}}} \tag{4.11}$$

Frost filter, similar to Lee filter, is based on the local statistics and the multiplicative model. The Frost filter replaces the pixel of interest with a weighted sum of the values within the *m-by-n* moving kernel. The weighting factors decrease with distance from the pixel of interest. The weighting factors increase for the central pixels as variance within the kernel increases [59].

$$\hat{f}(m,n) = \sum_{mxn} \alpha \exp(-\alpha D) \tag{4.12}$$

where $\alpha = \left(\dfrac{1}{\sigma_f \cdot \sqrt{mn}}\right)\dfrac{std\{S_{mn}\}}{mean\{S_{mn}\}}$, and D is the absolute value of the pixel distance between the center pixel to its surrounding pixels in the filter window. The parameters in the Frost filter are adjusted according to the local variance in each area. If the variance is low, then the filtering will cause extensive smoothing. While in high variance areas, little smoothing occurs and edges are retained [60].

RKT Filter. The rotating kernel transformation operates through selecting the largest filter output at each pixel from a set of templates that consists of kernels with small incremental steps from 0 to 360 degrees. The kernel itself consists of zeros and ones and is typically an elongated, line-like structure that is rotated in small discrete steps through 360 degrees. In essence, the RKT is an elongated neighborhood that repeats along different directions and retains the maximum result. This technique is efficient but rather in *ad hoc* fashion and uses no information concerning the speckle statistics. The convolution can be written as

$$\hat{f}_\theta(m,n) = f(m,n) * K_\theta(m,n),\ m,n \in S_{mn} \qquad (4.13)$$

where $K_\theta(m,n)$ is the kernel orientated at rotation angle θ. S_{mn} is the moving window defined by size m x n. The maximum values are calculated over all the rotated kernels and the output image is defined by,

$$\hat{f}(m,n) = \arg\max\left\{f(m,n) * K_\theta(m,n) : 0^0 \le \theta < 360^0\right\} \qquad (4.14)$$

The RKT algorithm is related to the class of "rotating kernel min-max transformation" (RKMT) [75]. In this case, the RKT technique is the maximum value output.

Anisotropic Diffusion Filter is a partial differential equation (PDE) based speckle removal approach that allows the generation of an image scale space, i.e. a set of filtered images that vary from fine to coarse, without bias due to filter window size and shape. Speckle reduction anisotropic diffusion (SRAD) filters [76] not only preserve edges but also enhances edges by inhibiting diffusion across edges and allowing diffusion on either side of the edge. SRAD is adaptive and does not utilize hard thresholds to alter performance in homogeneous regions or in regions near edges and small features. The diffusion technique is based on the same minimum mean square error (MMSE) approach to filtering as the Lee/Kuan and Frost filters. SRAD can be related directly to the Lee and Frost window-based filters. Thus, SRAD is the edge sensitive extension of conventional adaptive speckle filter. SRAD describes the idea of incorporating minimum mean square error, the local statistics of image, and anisotropic diffusion algorithm. Recall in Lee and Frost filter, the local statistics $C_{x,y}$, the coefficient of variation (COV) at position (x,y).

To implement a PDE version of the speckle reduction filters, an approximation version of $C_{x,y}$ is derived,

$$C_{x,y}^2 = \frac{(1/2)|\nabla f|^2 - (1/16)(\nabla^2 f)^2}{(f + (1/4)\nabla^2 f)^2} \tag{4.15}$$

A function *q*, called the *instantaneous coefficient of variation*, is introduced and can be view as a discretization version of the COV,

$$q(x, y; t) = \sqrt{\frac{(1/2)(|\nabla f|/f)^2 - (1/16)(\nabla^2 f/f)^2}{(1 + (1/4)\nabla^2 f/f)^2}} \tag{4.16}$$

This term combines a normalized gradient magnitude operator and normalized Laplacian operator to act as an edge detector. High relative gradient magnitude and low relative Laplacian value tend to indicate an edge. The SRAD algorithm is evolved according to diffusion equation,

$$\begin{cases} \dfrac{\partial f(x, y; t)}{\partial t} = div[c(q)\nabla f(x, y; t)] \\ f(x, y; 0) = f_0(x, y), \left.\dfrac{\partial f(x, y; t)}{\partial \vec{n}}\right|_{\partial\Omega} = 0 \end{cases} \tag{4.17}$$

Where $\partial\Omega$ denotes the border of image domain Ω, and initial image $f_0(x, y)$ has non-zero support over the image domain. $\vec{n}$ is the normal to $\partial\Omega$. The diffusion coefficient is defnied as,

$$c(q) = \frac{1}{1 + \dfrac{[q^2(x, y; t) - q_0^2(t)]}{[q_0^2(t)(1 + q_0^2(t))]}} \tag{4.18}$$

$$q_0(t) = \frac{\sqrt{\operatorname{var}[z(t)]}}{mean[z(t)]} \tag{4.19}$$

where $\mathrm{var}[z(t)]$ and $mean[z(t)]$ are the variance and mean over a homogenous area at time t, respectively. In SRAD, $q(x, y; t)$ serves as the edge detector in the speckled image. The function will exhitbit high values at edges and yields values near $q_0(t)$ in homogenous region. Thus, SRAD maybe viewed as the edge senstitive PDE version of the conventional adaptive speckle reduction filters such as Lee and Frost.

4.4 Spatial Speckle Reduction Results

For the purpose of evaluating the performance of the adaptive spatial filters quantitatively, five quality measures (SNR, PSNR, CSR, ENL and SSIM) are used first to evaluate the optimal kernel size. **Fig. 4.2** shows the plots of speckle filtering results with respect to different kernel sizes, ranging from 3 × 3 up to 31 × 31. Five spatial filtering algorithms are applied to 850 nm OCT caries image, as the images acquired at 1310 nm are considered as less speckle contaminated due to their high signal-to-noise ratio. Thus, the speckle reduction results are more apparent in 850 nm images. SNR and PSNR are standard measures of ideal noise suppression. CSR is a measure based on MSE to quantify an ROI in contrast to background speckle. The CSR is generally a more robust measure of image quality because it incorporates a measure of contrast (the difference of mean over variance) that does not increase without bound as the image becomes smoother. ENL is the measure of regional homogeneity, and SSIM is the measure of similarity between the original and speckle reduced images. Edge and fine detail preservation are measured by visual examination. For locally adaptive filters like Lee, Kuan and Frost, the SNR and PSNR values are inversely proportional to RMSE. After applying large kernel windows, these algorithms usually consider regions within the kernel window to be homogenous. As a result, the SNR and PSNR curves do not decrease like the other algorithms do. However, mean, median or even RKT filters are considered as straight forward pixel manipulation without prior knowledge of local statistics and they are not locally adaptive. Therefore, SNR and PSNR values decrease as a result of increasing RMSE. Notice that with the same window size, the RKT filter has higher values for CSR and ENL measures. This is possibly due to the fact that RKT filter is a "maximum" output filter that produces higher values over the other filters. This also cab be seen in **Figure 4.3** with more bright pixels in the lesion regions. SSIM is a comprehensive measure of image similarity and apparently local adaptive filters have advantages in retaining structural information when compared to simple mean or median filters.

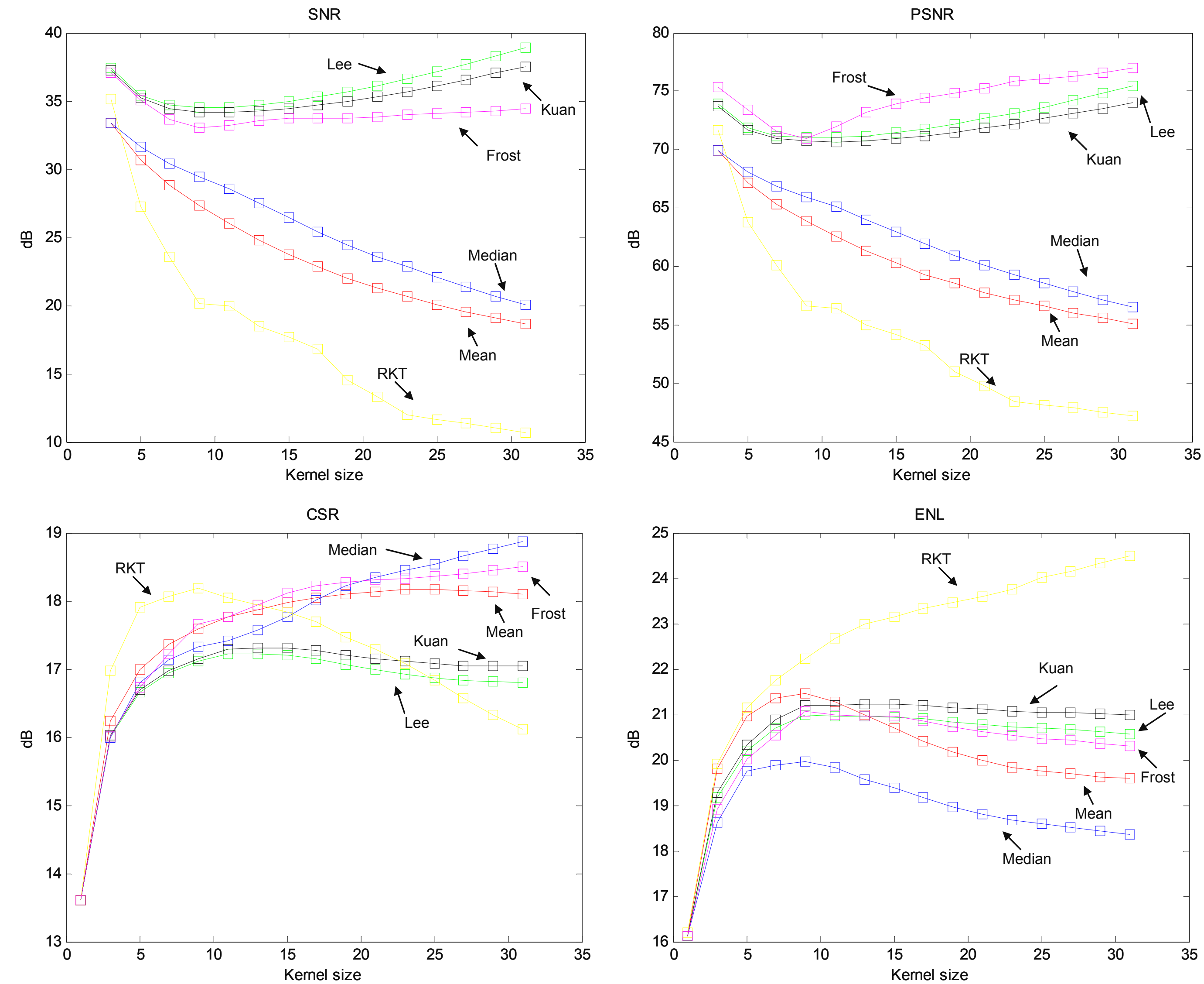

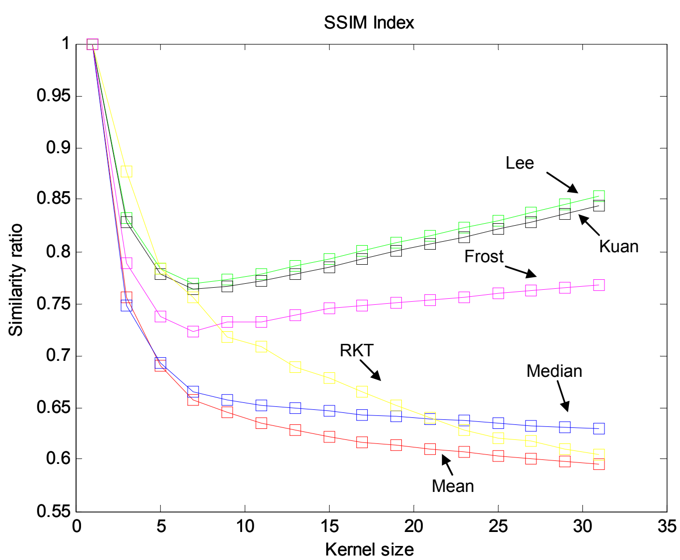

Figure 4.2 Five image quality matrices are computed with the increasing kernel size from 3 x 3 to 31 x 31. These matrices are different speckle reduction measures. SNR, PSNR, CSR and ENL are plotted with dB units. SSIM is plotted with similarity ratio (i.e. between 0~1).

By examining the numerical results from **Figure 4.2**, it appears that for most of the filters, when the window sizes range from 5 × 5 to 9 × 9, the evaluation metrics reach a "transition" region, where the slopes of most curves are at their minimum. As the kernel window size increases, detailed features are blurred, and the values of these metrics stay within small variations. The effect of kernel size on the image appearance is shown in the following representative 850 nm images (**Figure 4.3**). For comparison, image speckle filtering results with kernel sizes of 3 × 3, 7 × 7 and 21 × 21 are shown. When the kernel size is large, most algorithms generate artifact along the air-tooth surface, which is not desirable if the edge detection algorithm is applied. Overall, the kernel size 7 × 7 and 9 × 9 seem to produce reasonable results by suppressing the speckle grainy appearance and retaining homogeneity in certain region.

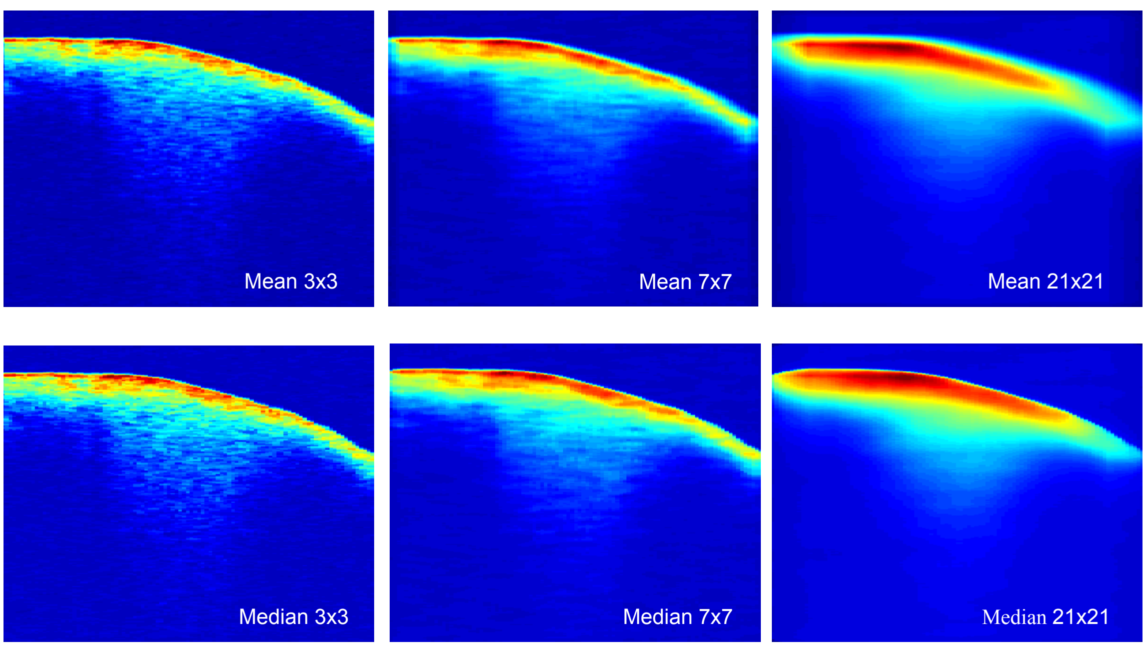

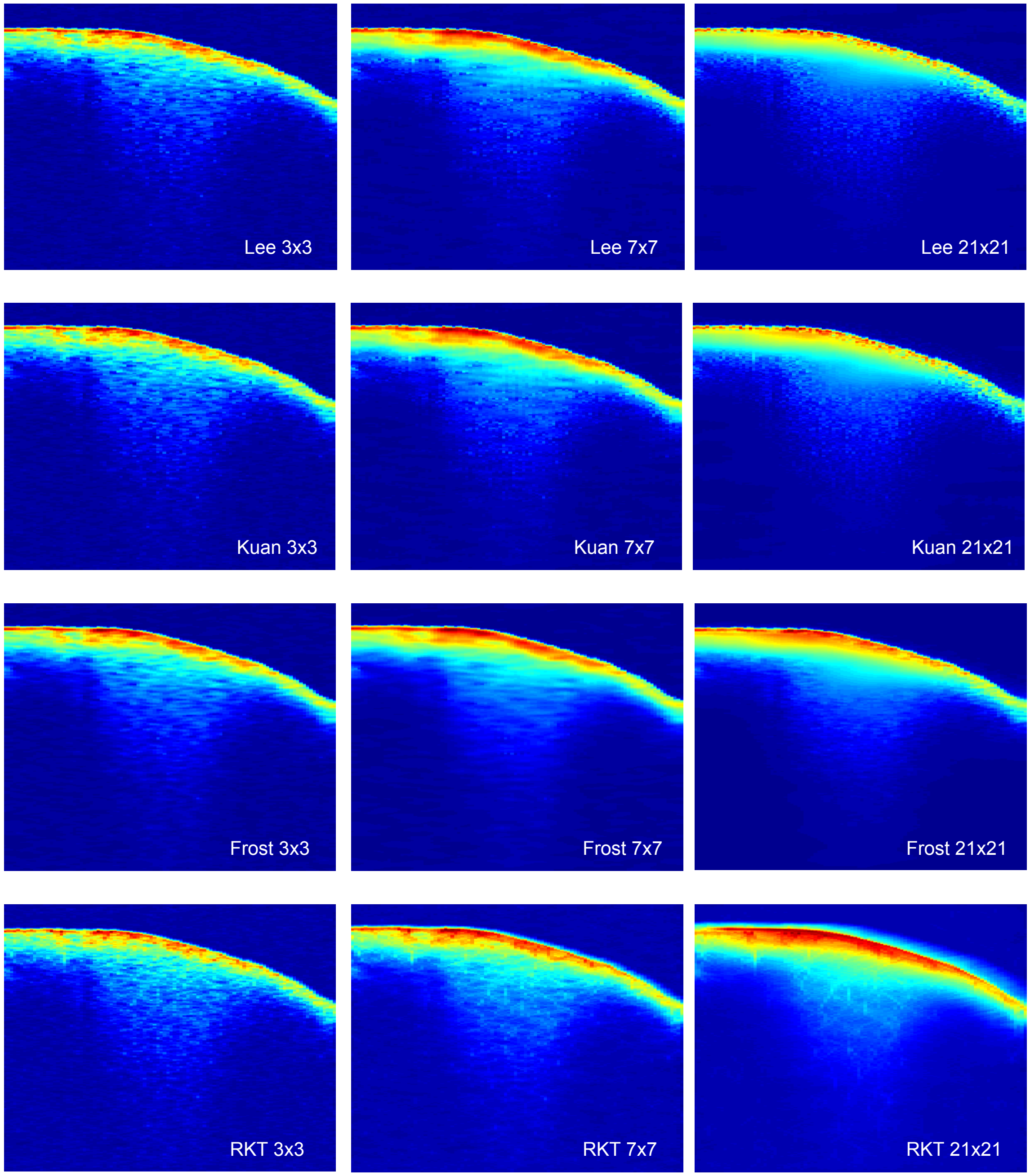

Figure 4.3 Images after speckle reduction with spatial adaptive filters with respect to kernel window sizes. Three representative kernel window sizes 3 x 3, 7 x 7 and 21 x 21 are displayed.

A comparison between SRAD and other adaptive spatial speckle reduction filters is shown in **Figure 4.4**. One of the parameters associated with SRAD filter is the number of iterations. Thus the quantities measures are plotted versus number of iterations from 0 to

140 with increment of 10 at each step. The PSNR and SSIM values are scaled in order to plot all five metrics into one graph.

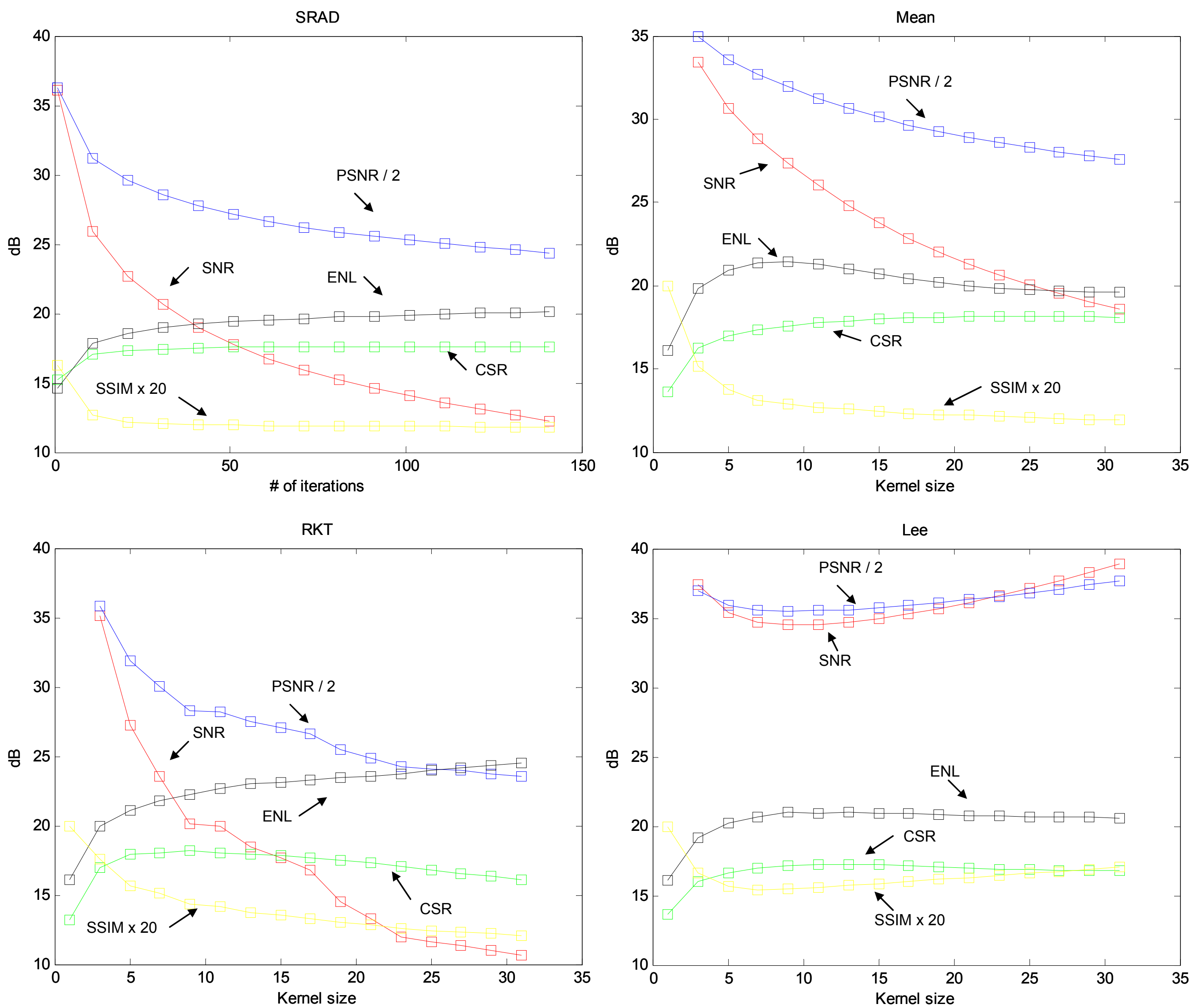

Figure 4.4 A comparison of SRAD filter speckle reduction parameter and three other adaptive speckle filters. SRAD plot is generated with increasing number of iterations from 0 to 140. The corresponding parameters are fitted in one graph, including SSIM and PSNR whose magnitudes are scaled to fit in the plot as indicated.

Similar conclusion can be drawn with the number of iterations as the increasing parameter since the evaluation metrics also appear to have a “transition” period at iteration numbers between 20 and 40. Similar gain levels are achieved. The image details and edges are also blurred as the iteration number goes up. For an overall visual comparison, the most satisfying filtering results are displayed for the purpose of identifying the pros and cons of each filter class. The algorithms are now applied to both 850 nm and 1310 nm images to give an overall evaluation for visual judgments. **Figure 4.5** shows different algorithms applied to 850 nm OCT images. Each image is labeled with the corresponding noise reduction method. The color difference in the background when comparing the filtered images with the original image is likely due to the changes in image intensities after applying each algorithms and its corresponding representation in false color scale. And it is one of the limitations representing intensity image with false color scale, as such false color representation can be sensitive to small changes in image intensities. When the proper window size is chosen, most of the algorithms seem to suppress speckle noise sufficiently. For the 850 nm image, the RKT filter provides good sharp edges and regional homogeneity. Lee and SRAD filters also give good results in outlining the shape of lesion, only with less sharp edges along the air-tooth surface. However, the result can be different from application to application.

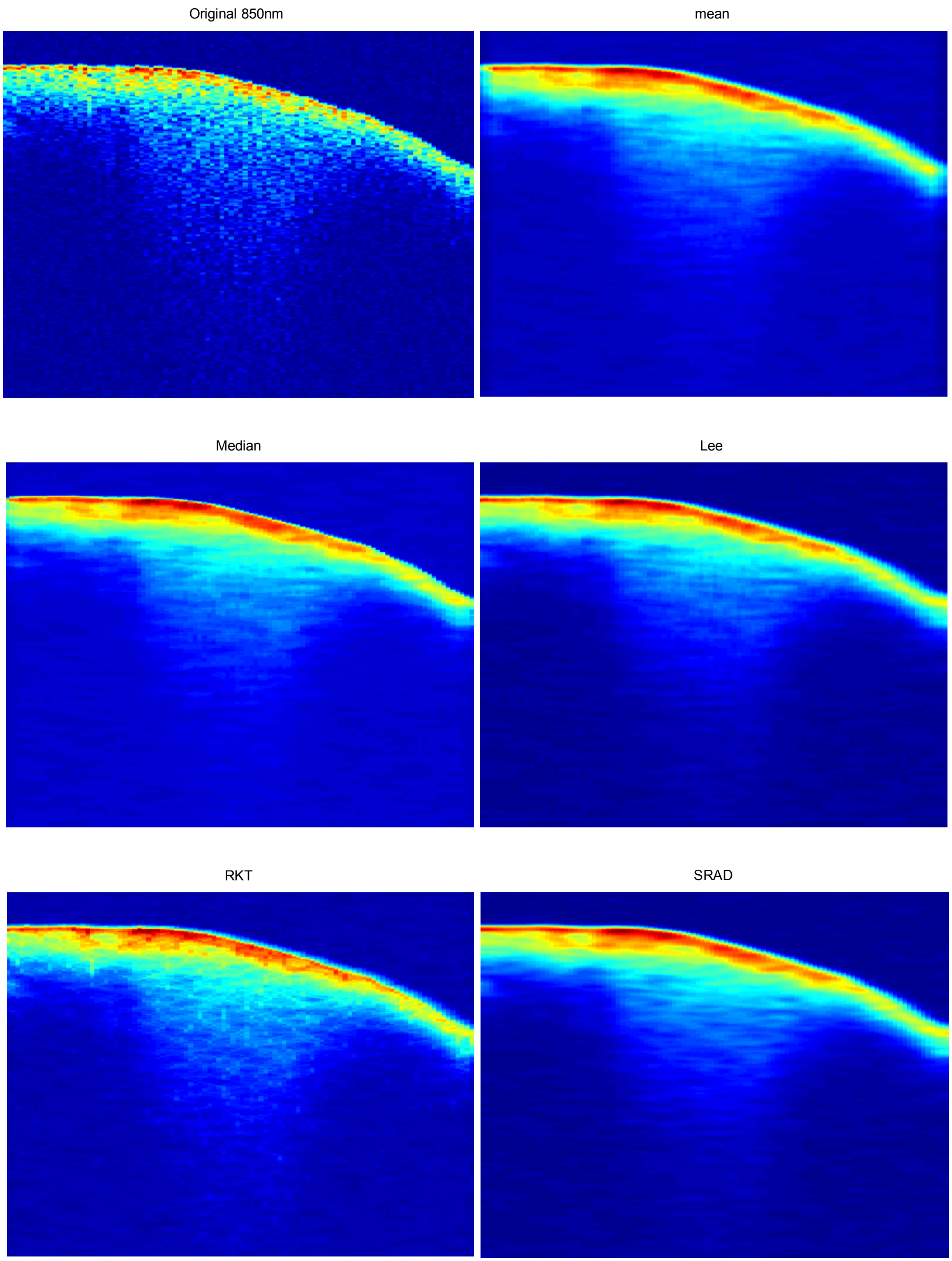

Figure 4.5 The above five speckle reduction algorithms are applied to 850 nm tooth image. For mean, median, Lee and RKT filters, the window size is chosen as 7 x 7. For SRAD filter, the number of iterations is chosen as 40.

When these algorithms are applied to 1310 nm images with higher resolutions, a different conclusion can be drawn. Assuming the same level of speckle reduction in the background from **Figure 4.6**, Lee, median and mean filter seem to produce reasonable results in the lesion region, where the results from RKT and SRAD filtering appear to be more noise contaminated. A second test image with contrast previously adjusted, is also filtered with these speckle suppression filters (**Figure 4.7**). RKT and Lee filter seem to produce more contrast in the lesion region. Visual enhancement as a result of contrast enhancement and speckle filtering could produce better lesion segmentation. However, with some drawbacks, the RKT and Lee filter generate more artifacts along the air-tooth surface, which blurs the sharp edge that was originally present. This is more apparent when applying these algorithms to a sound tooth image, shown in **Figure 4.8**. Sometimes, a strong edge response is desirable for the simple purpose of edge detection. However, loss in resolution near the edge could result in measurement errors when quantifying lesion sizes.

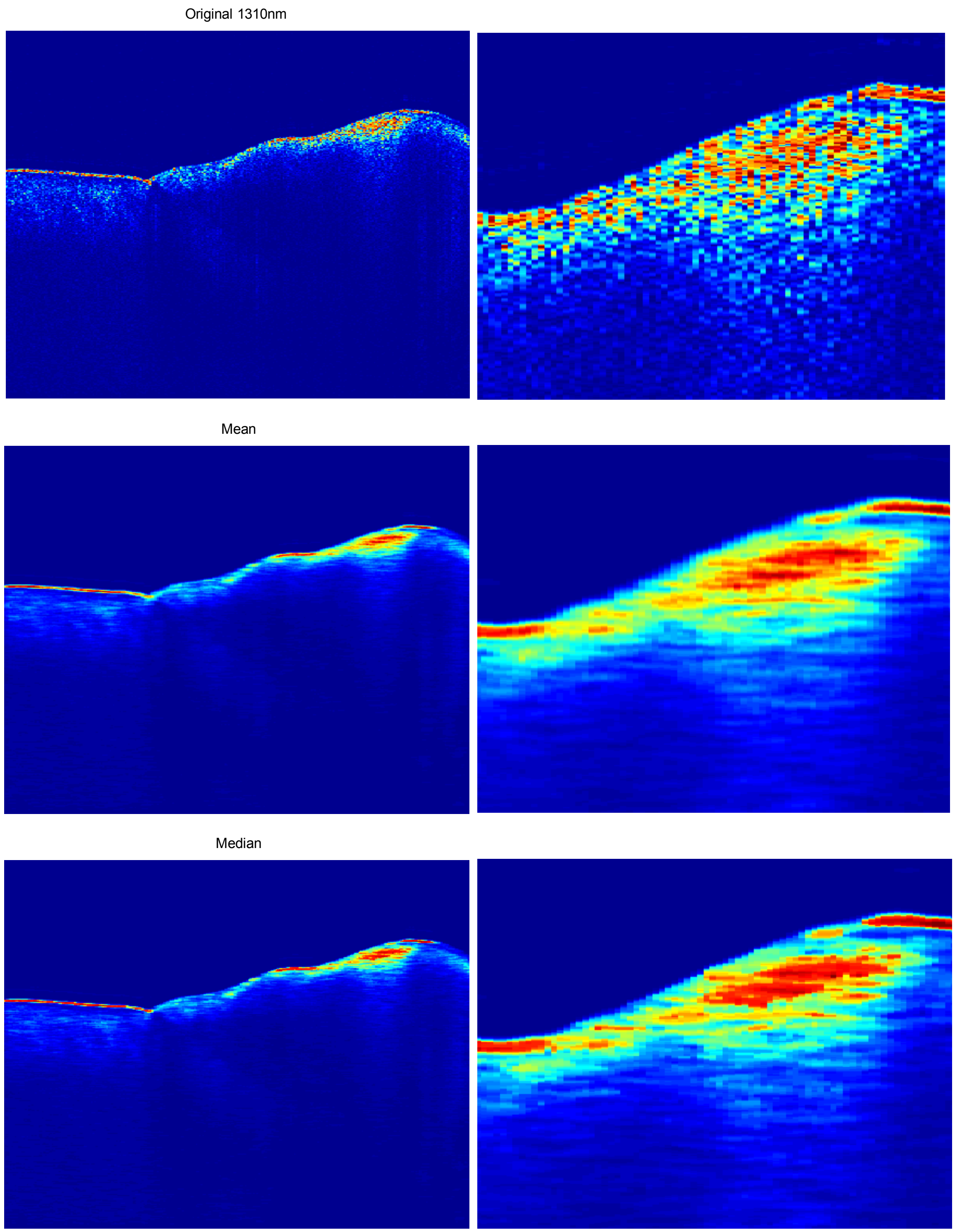

Original 1310nm
Mean
Median

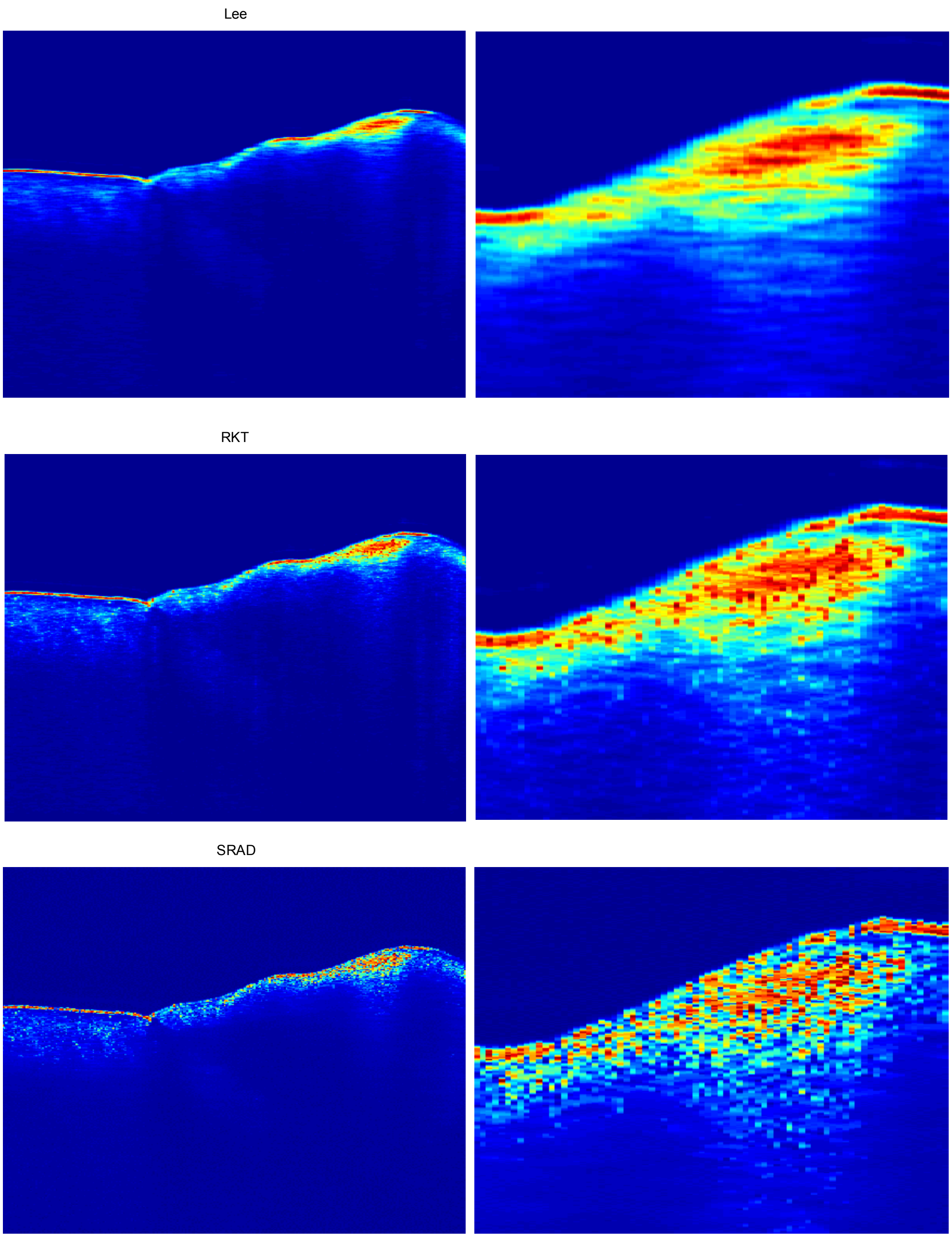

Figure 4.6 Five speckle reduction algorithms are applied to 1310 nm carious tooth image. For mean, median, Lee and RKT filters, the window size is chosen as 7 x 7. For SRAD filter, the number of iterations is chosen as 40. On the right hand column, the enlarged lesion region is shown to demonstrate the speckle reduction result.

Original 1310nm contrast adjusted

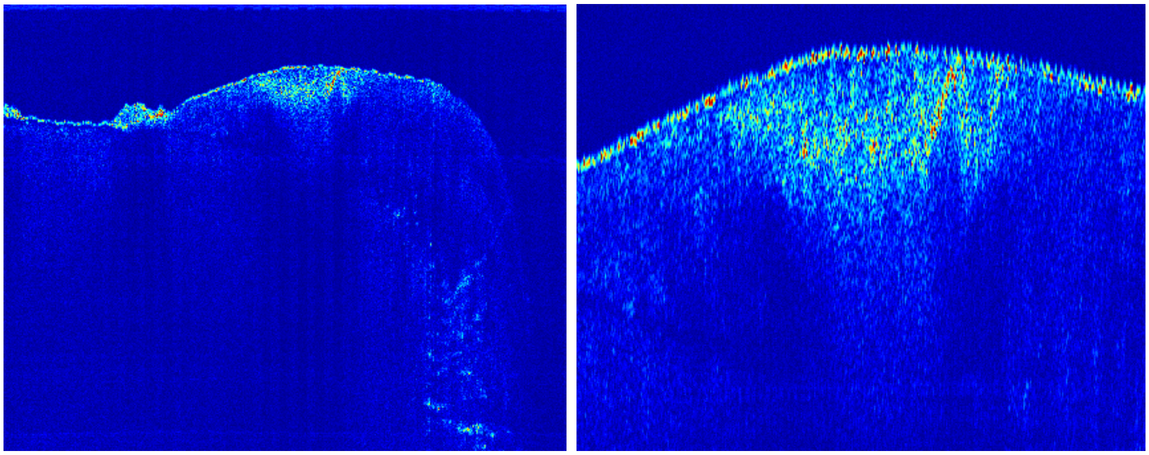

Mean

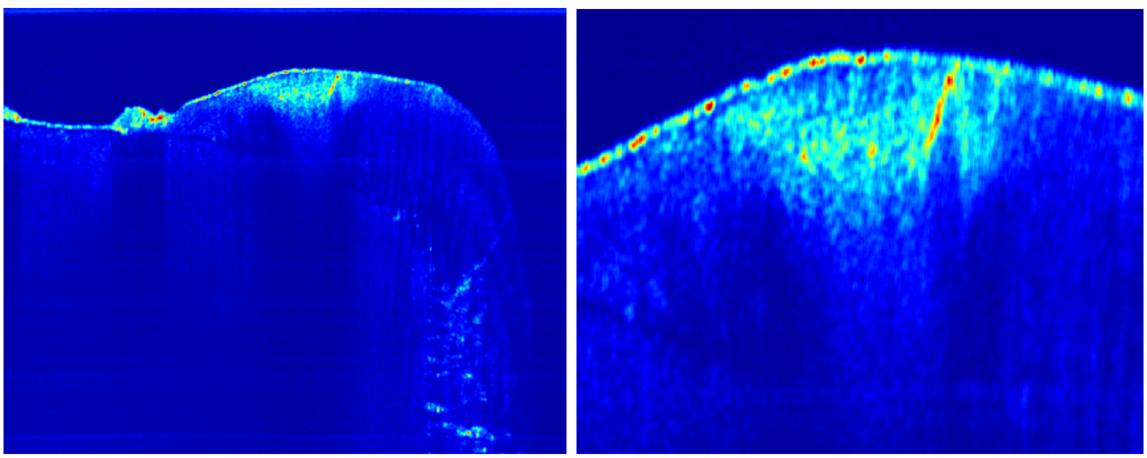

Median

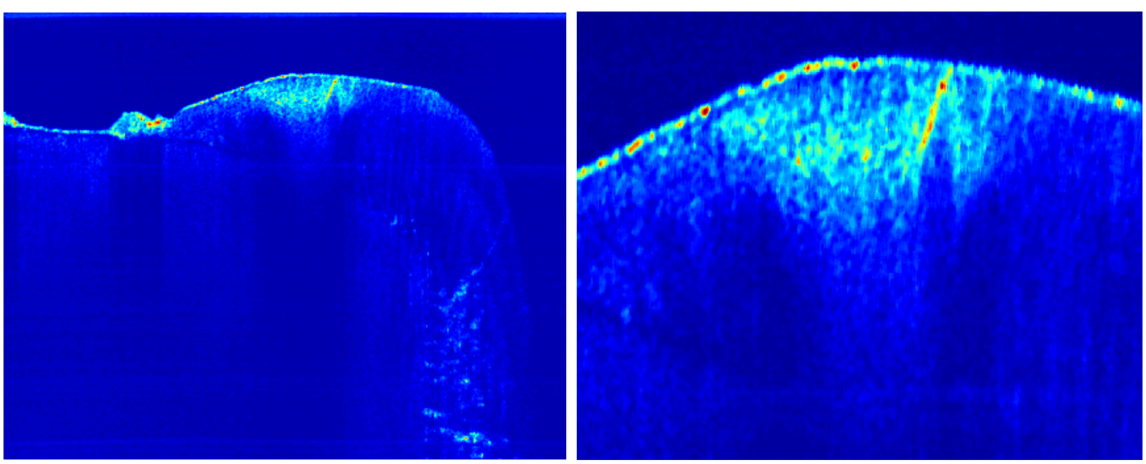

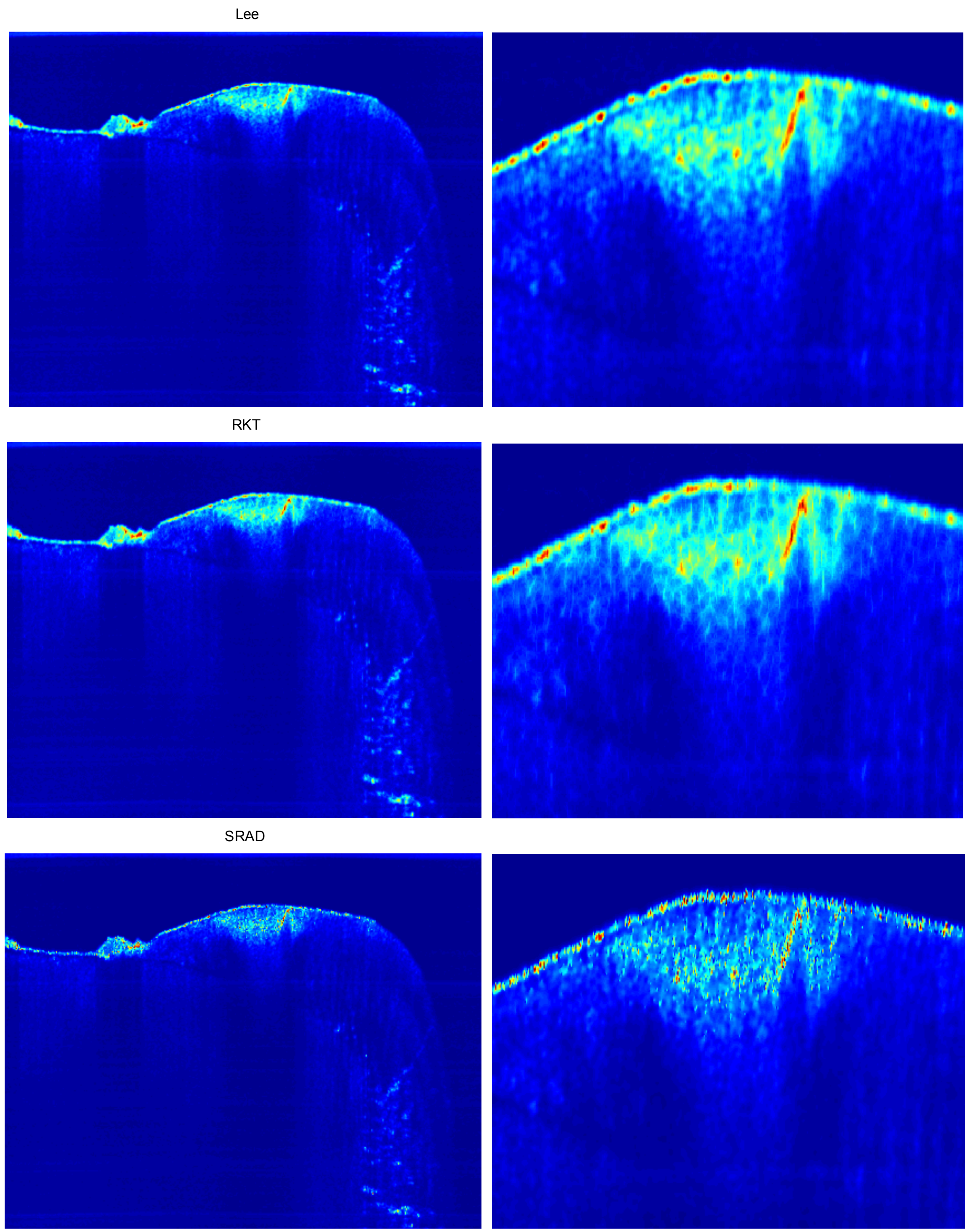

Figure 4.7 Five speckle reduction algorithms applied to another separate 1310 nm carious tooth image, whose image contrast has been previously adjusted. For mean, median, Lee and RKT filters, the window size is chosen as 7 x 7. For SRAD filter, the number of iterations is chosen as 40. On the right hand column, the enlarged lesion region is shown to demonstrate the speckle reduction result.

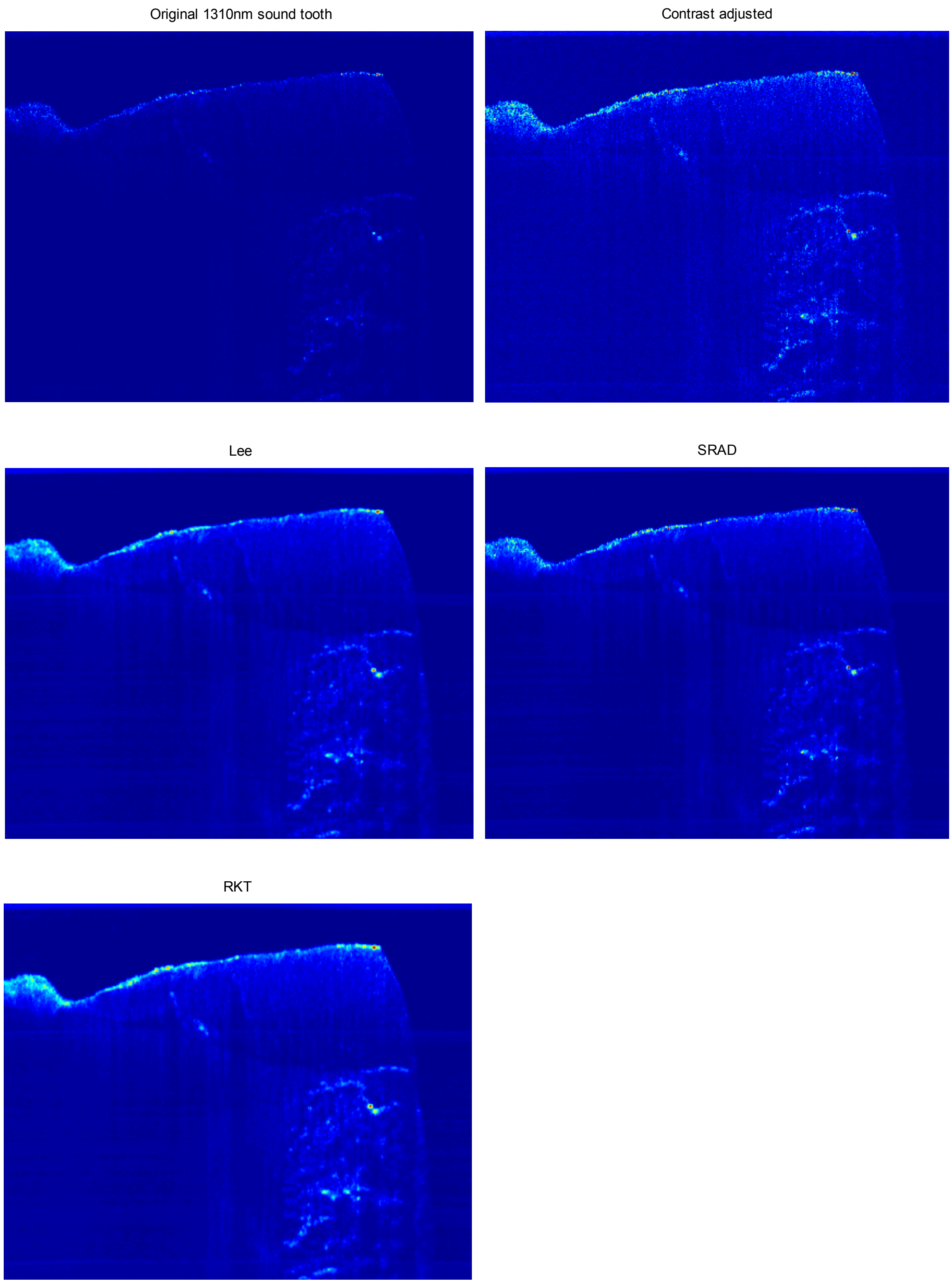

Figure 4.8 Three speckle reduction algorithms are applied to a 1310 nm sound tooth image, whose image contrast has been previously adjusted. For Lee and RKT filters, the window size is chosen as 7 x 7. For SRAD filter, the number of iterations is chosen as 40.

In general, adaptive filters such as Lee filter and SRAD filter allow both image enhancement and information conservation. Local adaptive filters provide good SNR. However the rule is not universal. Some results have shown discrepancies after applying speckle filtering to images acquired at different frequencies and resolution set-up. This can be explained by the fact that biological OCT images are very complex and contain various kinds of speckles and they differ with frequency response. A globally assumed homogeneity generally does not fit well to different regions within an image of biological tissue, and that is why the mean and median filters failed. The RKT filter smoothes the images and reveal interesting properties and features such as layers of the caries and light backscattered intensity response in the lesion area. However, the disadvantage is that artifacts appear near the air-enamel boundary, where the sharp edge gets blurred.

Some of the adaptive speckle reduction algorithms are applied to sound tooth image in combination with contrast enhancement. A good visual improvement is clearly displayed. The original image shows weak backscatters even in sound enamel region. After the contrast enhancement, unavoidably the speckle noise is also amplified along with the contrast. Three filters, Lee, SRAD and RKT have been applied to the noisy image. Good speckle reduction results are shown with all three filters. The features below the air-tooth surface, including DEJ line and sound enamel can be clearly identified. The RKT filter gives a strong response along the edge, as it is considered as an edge-detection filter. However, the loss in resolution is one of its disadvantages. This shortcoming can be greatly compensated by the process of image deconvolution later on to be discussed later in this chapter.

4.5 Wavelet-based Speckle Filters

In this Section, we review several representative wavelet based denoising methods for OCT ranging from thresholding to vector based minimum mean squared error estimation.

4.5.1. Discrete Wavelet transform

The wavelet transform has many unique features that have made it a popular method for the purpose of image processing. The wavelet transform performs a high degree of de-correlation between neighboring pixels, and it provides a distinct localization of the image in the spatial as well as the frequency domain. This transform also provides sub-band frameworks in which both high and low frequency components of the image can be analyzed separately. The significant wavelet coefficients corresponding to important edge information and other high-frequency content of the signal are often dispersed among a large number of insignificant coefficients.

There are many wavelet that can be used effectively, such as the “Haar", “Daubeschies”, “Coiflets", “Symlets", “Morlets", “Mexican Hat", “Meyer" and “Biorthogonal" wavelets [77]. All these wavelets share the following three general characteristics:

1. A wavelet system is a set of building blocks to construct or represent a signal or function. It is a two-dimensional expansion set (usually a basis) for some class of one- (or higher) dimensional signals.

2. The wavelet expansion gives a time-frequency localization of the signal. This means most of the energy of the signal is well presented by a few expansion coefficients.
3. The calculation of the coefficients from the signal can be done efficiently. It turns out that many wavelet transforms (the set of expansion coefficients) can be calculated with O(N) operations. More general wavelet transforms require O(N log(N)) operations, the same as for the fast Fourier transform (FFT) [77].

Throughout this thesis, the Daubeschies wavelet system [78] of order N = 8, denoted as “Db8" is used when implementing wavelet-based schemes. For the purpose of signal denoising, a smooth wavelet system is generally desired. While there are many wavelet systems that possess varying degree of smoothness and regularity, the selection of the “Db8" wavelet, which possesses the required properties, is somewhat arbitrary. Clearly, one could have chosen any one of the other smooth wavelets, such as “Symlets" or “Coiflets" wavelets.

The wavelet transform reorganizes image content into a low-resolution approximation and a set of details of different orientations and different resolution scales. A fast algorithm for the discrete wavelet transform is the iterative filter bank algorithm of Mallat [79], where a pair of high-pass and low-pass filters followed by down sampling by two is iterated on the low-pass output. In a decimated wavelet transform that we consider here, down sampling is included, and instead the filters are down sampled at each decomposition stage. The outputs of the low pass filter are the scaling coefficients and the outputs of the high-pass filter are the wavelet coefficients. At each decomposition level, the filter bank is applied sequentially to the rows and to the columns of the image. Low-pass filtering of both the rows and the columns yields the low-pass LL sub-band and other combinations of low-pass and high-pass filtering yield the wavelet sub-bands at different orientations: High-pass filtering of rows and low-pass filtering of columns (HL) yields horizontal edges and the opposite combination (LH) yields vertical edges, while high-pass filtering of both the rows and the columns (HH) yields highest frequency information, corners and edges that are close to diagonal orientations.

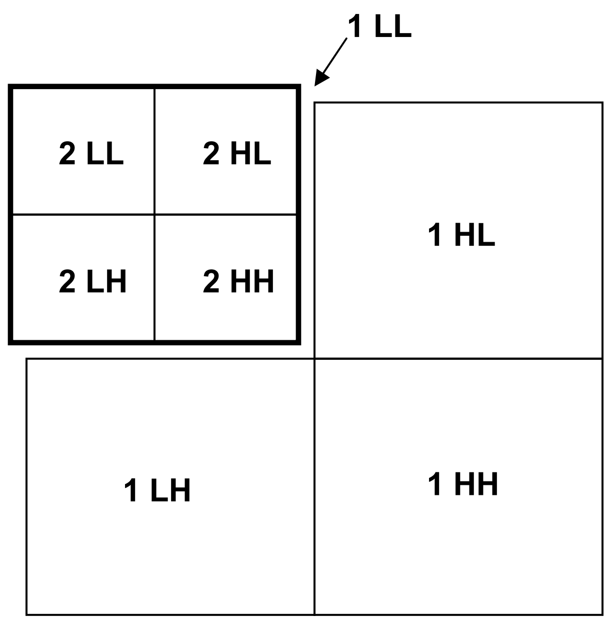

Figure 4.9 Illustrates wavelet decomposition using low-pass and high-pass filters. At each level, image is decomposed into four components, representing the original image: LL, LH, HL and HH. At each level, the image is also down-sampled and later on will be up-sampled when the inverse wavelet is applied.

The j-th decomposition level yields the coefficients at the resolution scale $2j$. Critically sampled (orthogonal) wavelet transform is not shift-invariant. In such a representation, small errors in estimation of the coefficients result in annoying blobs and ringing artifacts. Denoising performance is much improved when using redundant and (nearly) shift invariant transforms. Common approaches include using non-decimated wavelet transform [80], dual-tree complex wavelet transform [81] and cycle-spinning [82]. Cycle-spinning yields a similar improvement over the critically-sampled case as the non-decimated transform. More recent approaches achieve further improvements in the denoising performance by using highly redundant representations with multiple orientation bands such as curvelets [83] and steerable pyramids [84]. Another approach for a non-decimated wavelet transform is implemented with the method à trous [80].

4.5.2. The Wavelet Thresholding

Wavelet thresholding for image denoising attempts to remove the noise present in the signal while preserving most of the signal characteristics. If the image model or the true image is available, designing a thresholding transform $T(x,t)$ with threshold t requires the MSE,

$$MSE = E\{\left\|\hat{f}(x,y) - f_{true}(x,y)\right\|^2\} \tag{4.20}$$

To be minimized. Generally the global methods are referred to hard thresholding and soft thresholding. The hard thresholding operator is defined as,

$$T(x,t) = \begin{cases} x, & if\,|x| \geq t \\ 0 & otherwise \end{cases} \tag{4.21}$$

The soft thresholding operator is defined as,

$$T(x,t) = \begin{cases} x - t, & if\,|x| \geq t \\ x + t & f\,|x| \leq t \\ 0 + t & otherwise \end{cases} \tag{4.22}$$

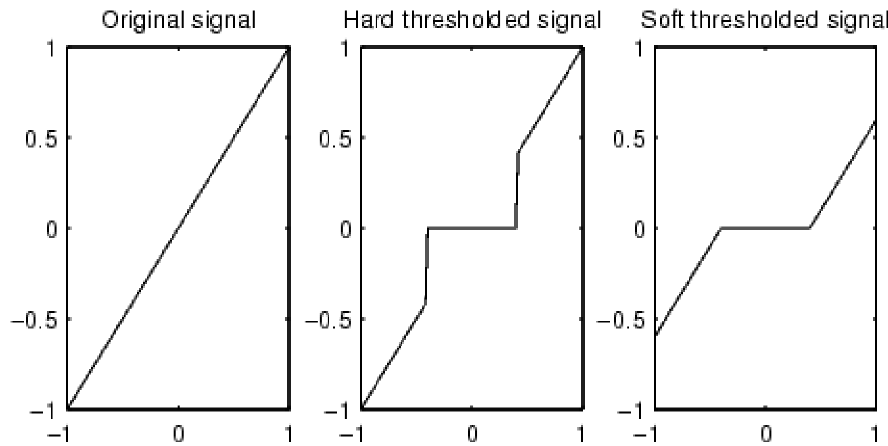

Figure 4.10 Examples of hard and soft thresholding applied on the wavelet coefficients.

Note that the hard thresholding appears to be more an intuitive procedure. On the other hand, soft thresholding shrinks coefficients above the threshold t. The underlying concept of wavelet denoising of images is similar to the above mentioned one-dimensional case. In the following section, some of the standard wavelet thresholding methods will be briefly described, implemented and compared. These techniques include VisuShrink, SureShrink, MinimaxiShrink and BayesShrink which differ in the selection of the threshold t and the strategy employed in applying the thresholding operator.

VisuShrink technique consists of applying the soft thresholding or hard thresholding using a universal threshold [80]:

$$t_{universal} = \sqrt{2\ln(M)} \times \hat{\sigma} \tag{4.23}$$

where M is the signal size and $\hat{\sigma}$ is the estimated noise standard deviation. $\hat{\sigma}$ is estimated by the empirical rule that if the speckle is assumed to be distributed Gaussian, the standard deviation can be approximated by the sample statistics: $\sigma = k \cdot median(|HH_1|)$.

k is a magnitude correction factor, and HH_1 is obtained by high-pass filtering of both the rows and the columns of the original image at the first level. The maximum of any M values as normal distribution will be smaller than the universal threshold with high probability, with the probability approaching 1 as M increases. Thus, with high probability, a pure noise signal is estimated as being identically zero. However, for denoising images, VisuShrink is found to yield an overly smoothed estimate. This is because the universal threshold ($t_{universal}$) is derived under the constraint that with high probability, the estimate should be at least as smooth as the signal. So the $t_{universal}$ tends to be high for large values of M, killing many signal coefficients along with the noise. Thus, the threshold does not adapt well to discontinuities in the signal.

SureShrink is based on applying a sub-band adaptive threshold, a distinct threshold is computed for each detail sub-band upon SURE (Stein's unbiased risk estimator), a method for estimating the risk of mean squared error. The risk is defined as [85],

$$R(x,t) = E\{\|x_j - T(x_j, t)\|\} \tag{4.24}$$

where R denotes the associate risk of a soft thresholding operator as each decomposition level j. The results have shown superiority over VisuShrink. The image sharp features of the image are retained and the MSE is considerably lower. This is because SureShrink is subband adaptive.

MinimaxiShrink [86] is developed according to Minimax thresholding. It uses a fixed threshold chosen to yield Minimax performance for mean square error against an ideal procedure. The Minimax principle is used in statistics in order to design estimators. Since the de-noised signal can be assimilated to the estimator of the unknown regression function, the Minimax estimator is the one that realizes the minimum of the maximum mean square error obtained for the worst function in a given set.

BayesShrink [87] threshold is driven in a Bayesian framework, and the assumption for generalized Gaussian distribution (GGD) still holds for the wavelet coefficients in each sub-band. The goal is to find the threshold t which minimizes the Bayesian Risk. Assuming such distribution for the wavelet coefficients, the standard deviation and Gaussian shape parameter is estimated for each sub-band threshold. The threshold t is found which minimizes the Bayesian Risk, i.e.

$$R(x,t) = E\{\|x_j - T(x_j,t)\|\} \tag{4.25}$$

Then the optimal threshold is given by

$$t* = \arg\min\left\{E\{\|x_j - T(x_j,t)\|\}\right\} \tag{4.26}$$

Numerical calculation is used here to find its value, since there is no closed form solution. T is found to be,

$$t* = \beta \frac{\mathrm{var}(noise)}{std(signal)} \tag{4.27}$$

The parameter β is the Gaussian shape parameter, and it is to be estimated together with the standard deviation of the signal. The noise variance is not estimated based on the original image, but it is estimate from the first level sub-band HH_1 by median estimator.

4.6 Wavelet Domain Speckle Reduction Results

Different thresholding methods are implemented for the purpose of speckle reduction and image restoration. For 850 nm OCT images, the range of thresholds for different algorithms is between 3.2486 and 4.6518. Only the two extreme values are selected to show how soft/hard thresholding affects image denoising outcomes. Good speckle reduction result is shown with soft thresholding (**Figure 4.11**). The edge sharpness is preserved and the lesion area is clearly outlined. Refer to **Figure 4.5** for a comparison with spatial speckle reduction results.

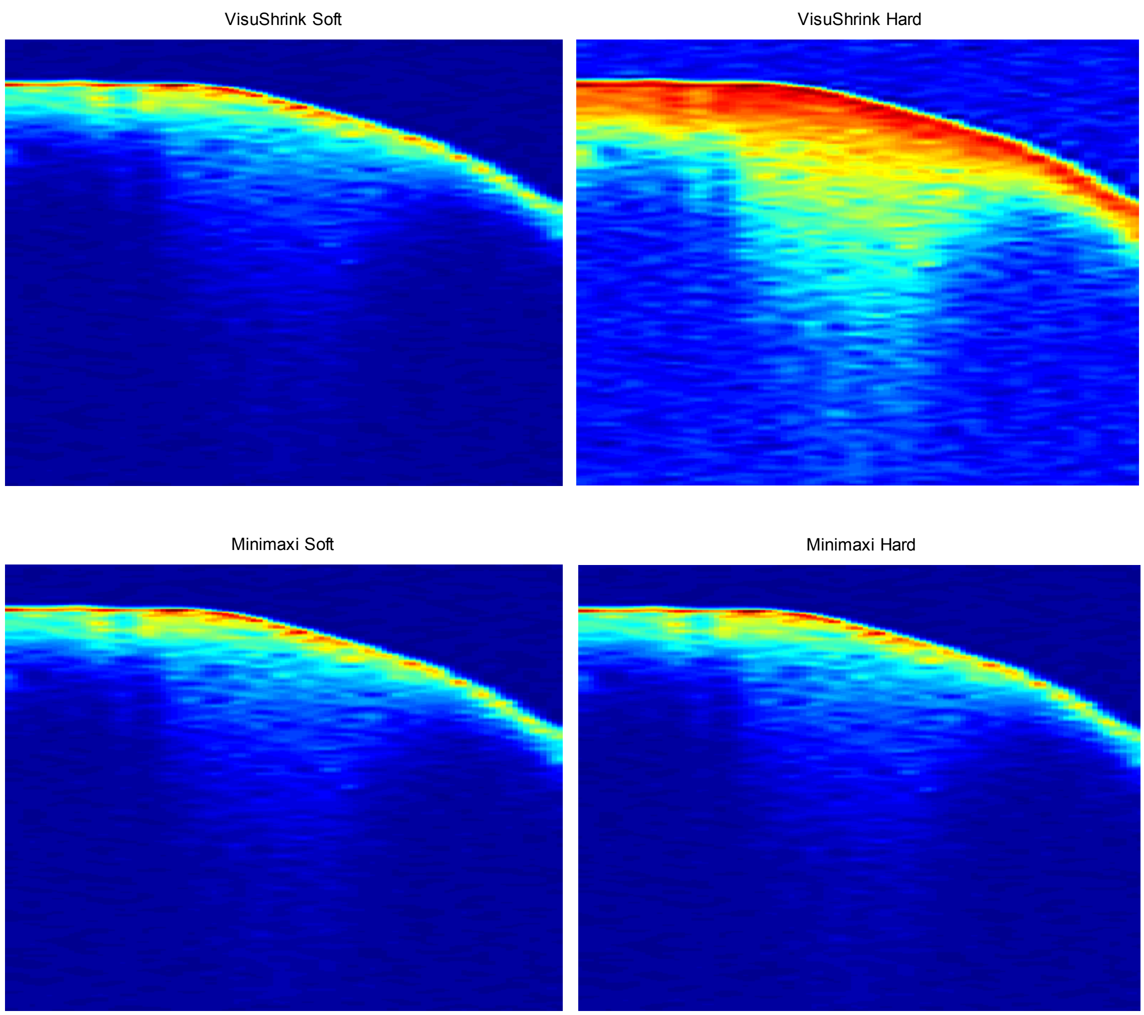

Figure 4.11 Results of applying VisuShrink and Minimax with soft and hard thresholding, to 850 nm OCT image. With both algorithms, soft thresholding gives satisfying results.

To compare the wavelet-domain filter and the other spatial-domain filters, in terms of gain level and the tendency of gain over the wavelet decomposition at each level, the five image quality measures similar to previous plots are shown (**Figure 4.12**). Again, PSNR and SSIM values are scaled to fit in one graph. The horizontal parameter is the wavelet decomposition levels, from 0 up to 4. 'level-4' is set as the upper bound. As the decomposition level increases, the image starts losing structural information. Similar results to spatial filtering can be observed. For different metrics, the corresponding gain levels are calculated. Different thresholding methods only change their corresponding gain, as they are merely the differences in threshold values. The dynamics of the graphs seems follow the same trend as spatial filtering. The SNR and PSNR decrease as the decomposition level increases.

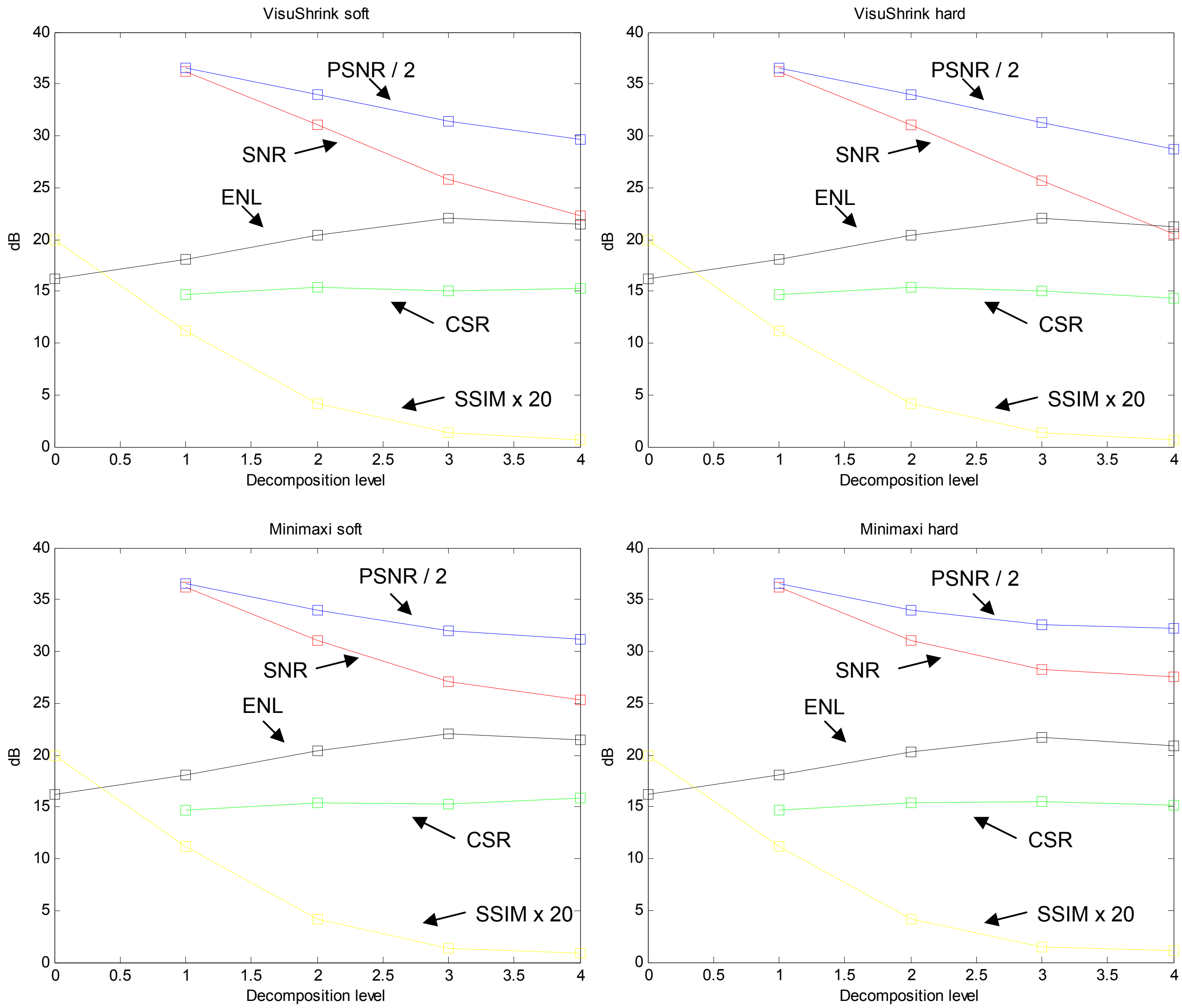

Figure 4.12 Plots of image quality measure when applying various wavelet-domain denoising techniques. These metrics can be compared with previous similar plots from spatial domain speckle filtering.

Different thresholding schemes were also applied to 1310 nm images. The threshold range is between 1.3119 and 5.1882. Similarly, only the two extreme values are shown here. **Figure 4.13** demonstrates the wavelet domain denoising results with two thresholding schemes at first decomposition levels. The overall image despeckling effects are shown on the left hand column and on the right hand column are the enlarged lesion regions. The noticeable advantage of wavelet filtering is the edge preservation. The border line at the air-tooth surface is not blurred. At proper threshold levels, good intensity response at the lesion region is shown.

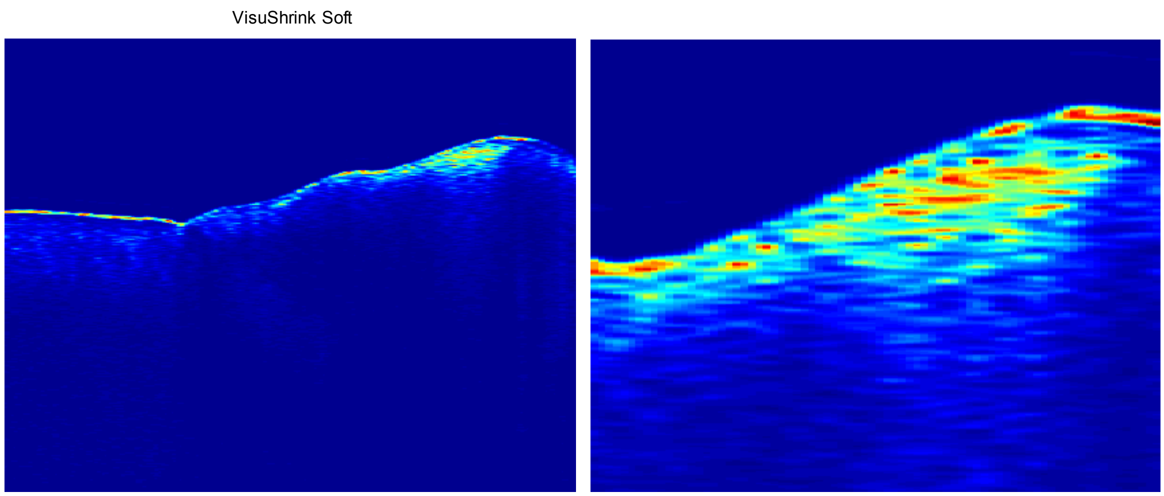

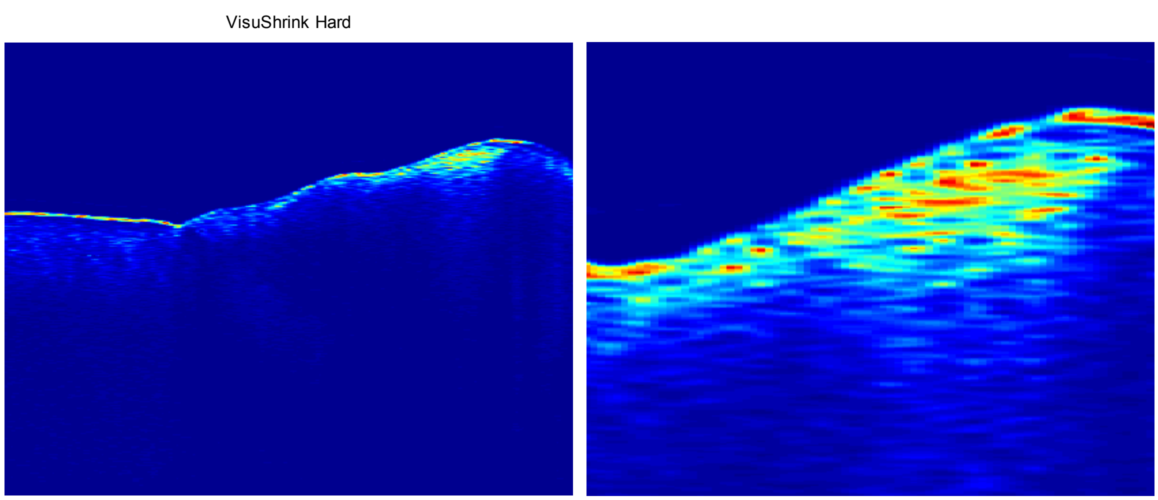

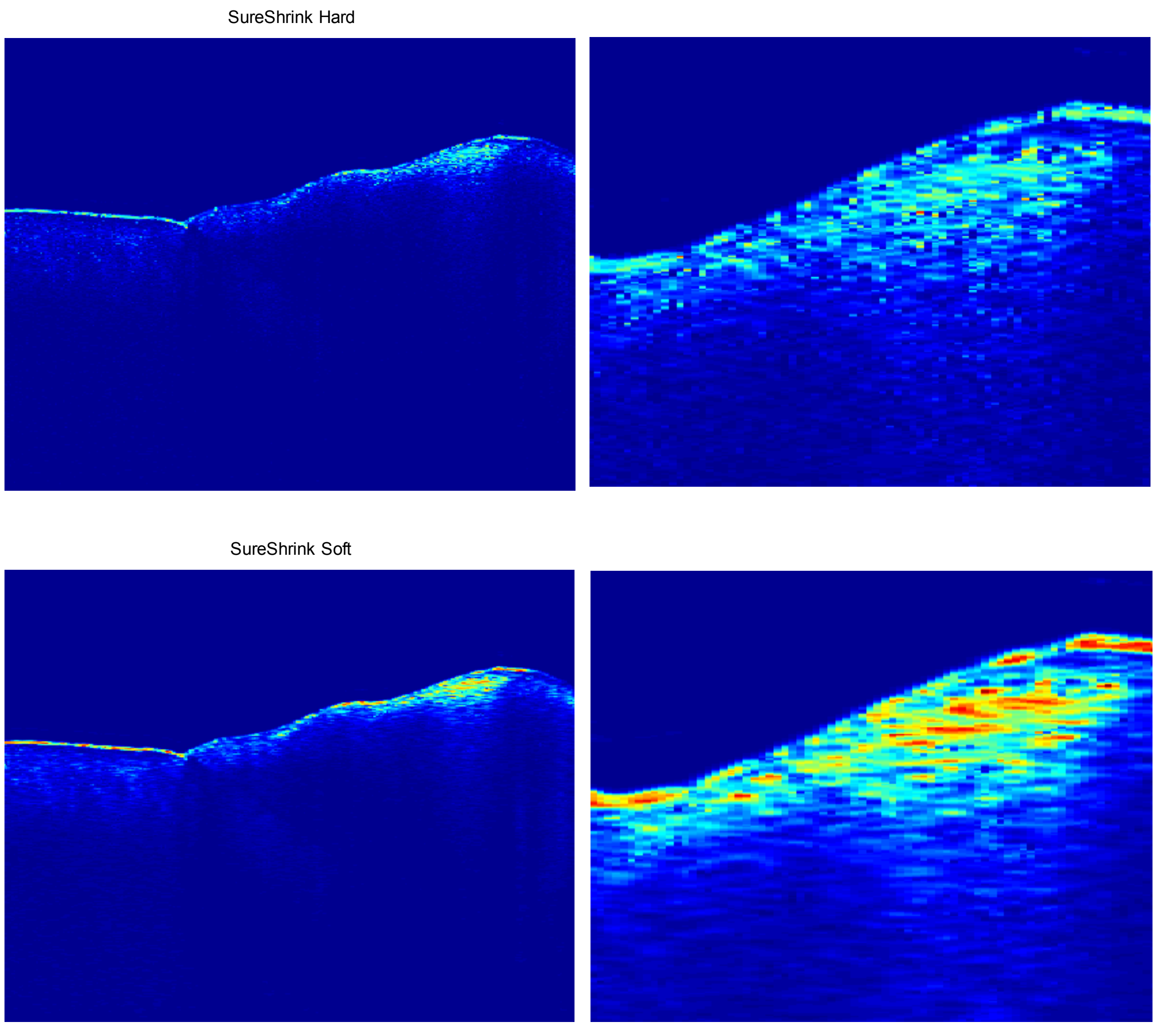

Figure 4.13 Results of applying SureShrink and VisuShrink with soft and hard thresholding, to 1310 nm image. Zoomed areas are the lesion areas.

The SureShrink thresholding was implemented on a second set of 1310 nm OCT images. This set of images has been previously adjusted with contrast stretching and histogram power-law transformation. A visual improvement as compared to the original noisy image is clearly observed. Comparing this result to the other spatial filtering results (**Figure 4.6** and **Figure 4.7**), less intensity is shown in the lesion area. The consequences of different intensity response at the lesion area after filtering which affect segmentation outcomes is to be studied in the next chapter.

SureShrink Soft

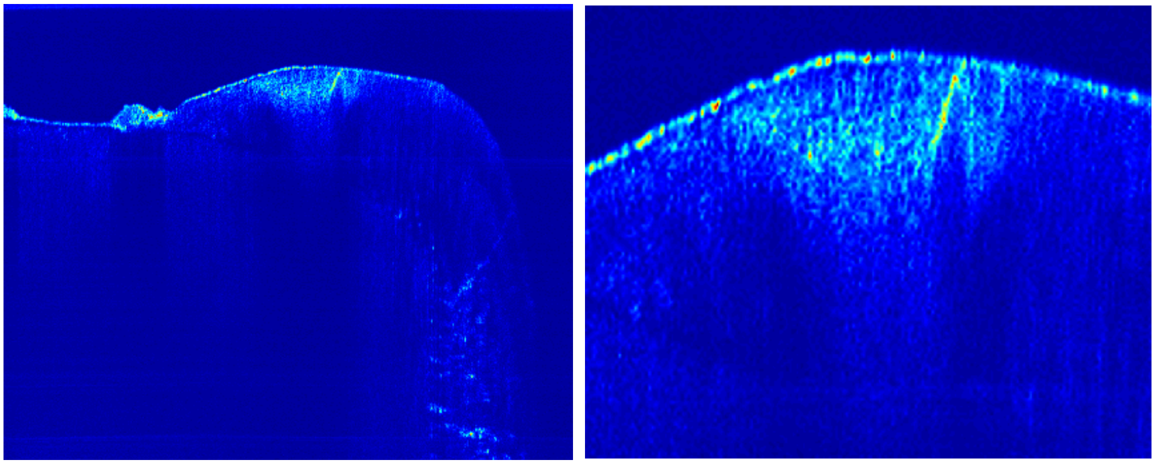

SureShrink Hard

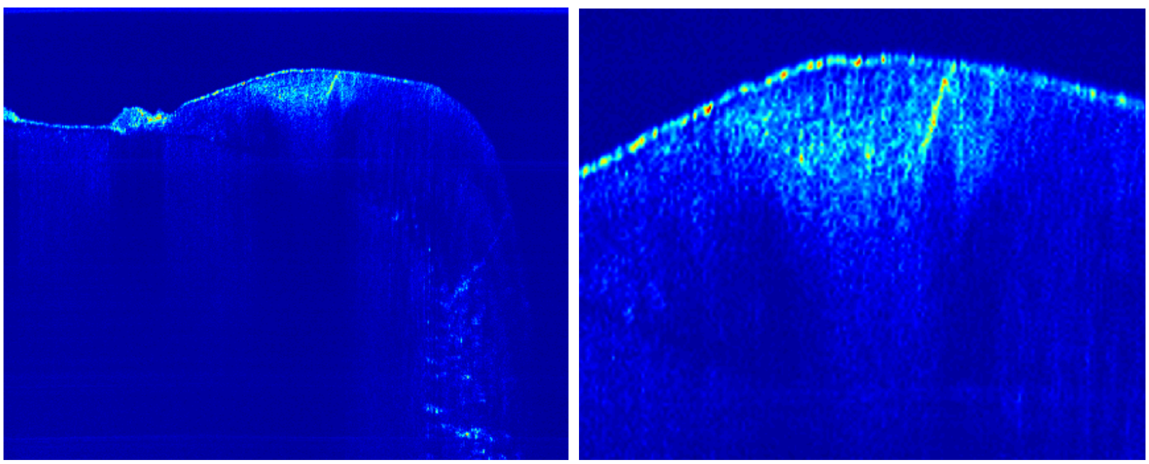

VisuShrink Soft

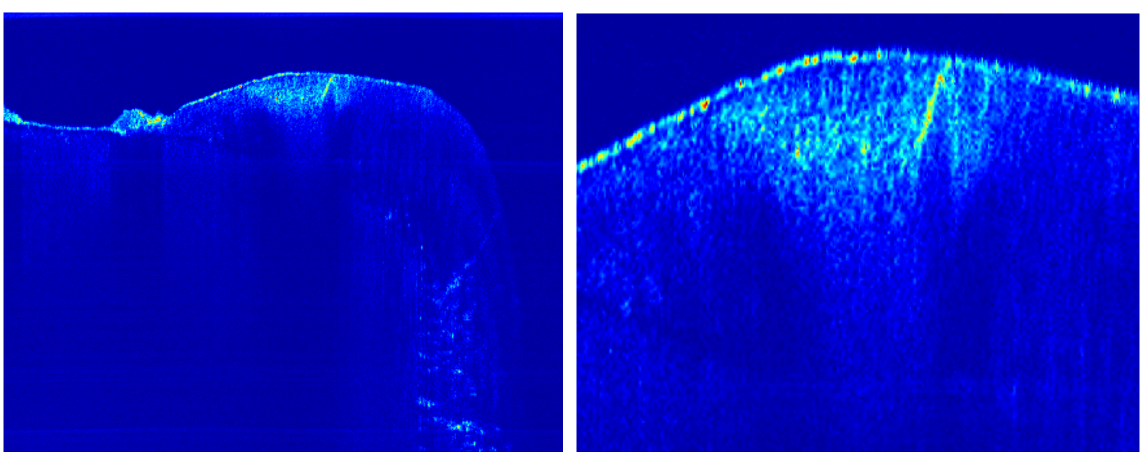

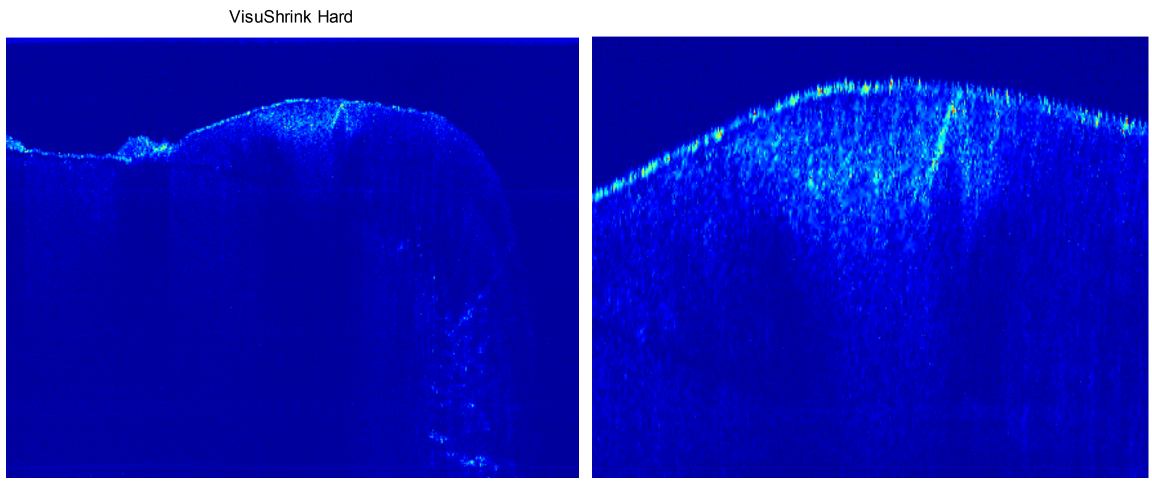

Figure 4.14 Results of applying SureShrink and VisuShrink with soft and hard thresholding, to 1310 nm image. Zoomed areas are the suspicious lesion (right column).

Figure 4.15 is the result of wavelet-domain speckle reduction from a sound tooth image. Notice that wavelet domain techniques yield similar results when compared with the other spatial domain filters. This is evident when comparing the sound enamel region and the outcomes of wavelet-filtering is not “washed-out”.

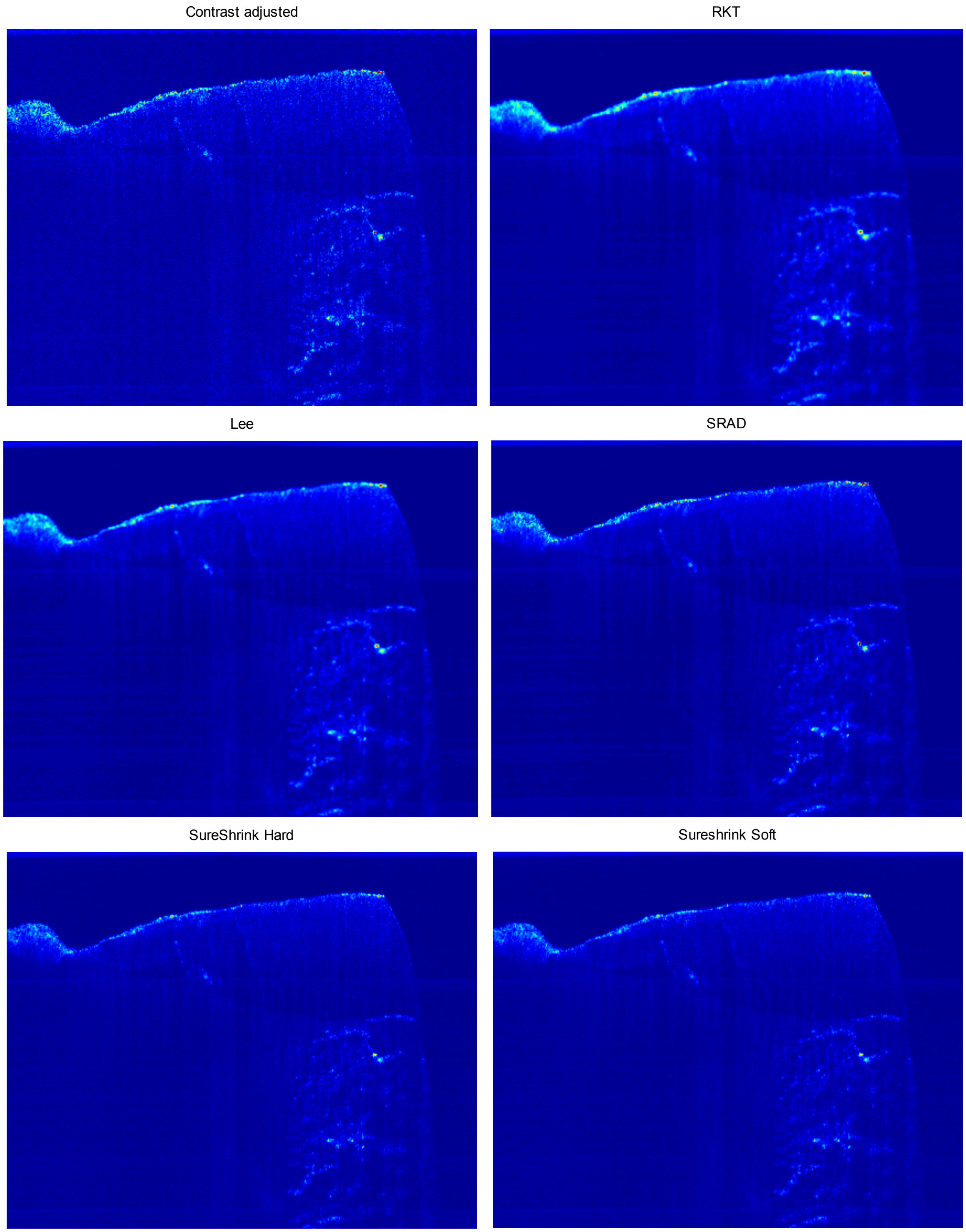

Figure 4.15 Results of applying wavelet-domain speckle reduction to 1310 nm OCT sound tooth image. This result is compared with spatial domain filtered images.

Both quantitative and visual assessment suggest that both spatially adaptive and wavelet-transform domain filters have considerable value. The use of local statistics helps to improve the differentiation of speckle noise from image pixels and preserve detail information. Although some of these existing spatial speckle filters are termed as "edge-preserving" and "feature preserving," there exist limitations of the filtering approach. The spatial filters are sensitive to the size and shape of the filter window. Given a filter window that is too large (compared to the scale of interest), over-smoothing will occur and edges will be blurred. A small window will decrease the smoothing capability of the filter and will leave speckle when any portion of the filter window contains an edge. The coefficient of variation will be high and smoothing will be inhibited. Therefore, noise/speckle in the neighborhood of an edge (or in the neighborhood of a point feature with high contrast) will remain after filtering. Spatial domain filters are not directional. In the vicinity of an edge, all smoothing is precluded, instead of inhibiting smoothing in directions perpendicular to the edge and encouraging smoothing in directions parallel to the edge. The advantages of wavelet decomposition enable noise reduction in all horizontal, vertical and diagonal directions. Also the fashion of *ad hoc* implementation only demonstrates the insufficiency of the window-based approaches. The straight forward pixel operation enacts neighborhood averaging and filtering in the extreme cases leads to blotching artifacts from averaging filtering and noisy boundaries from leaving the sharp features unfiltered. The log-transform prior to wavelet domain denoising is necessary and adheres to multiplicative nature of speckle noise. Overall, wavelet-domain filter demonstrates appealing features for its versatility, efficiency and adaptability.

4.7 Speckle Reduction in Conjunction with Iterative Deconvolution

Most of the methods mentioned above suppress only noise, while another class of methods attempt at resolution improvement/deblurring by applying deconvolution. In fact, one of the occurrences in image denoising, especially with spatial "averaging" filters like RKT, is the resolution loss. Also, the interferometric distortion of OCT as a result of the convolution between the point spread function (PSF) of the OCT scanner and tissue reflectivity function, introduces blurring.

Ideally the noise-free observation $f(x,y)$ is the result of the convolution of $f_{true}(x,y)$ and the PSF $h(x,y)$, given by

$$f(x,y) = f_{true}(x,y) * h(x,y) \tag{4.28}$$

In the Fourier domain the convolution is replaced by multiplication.

$$F(u,v) = F_{true}(u,v)H(u,v) \tag{4.29}$$

where $F(u,v)$, $F_{true}(u,v)$ and $H(u,v)$ are the Fourier domain representation of the spatial domain function respectively. Therefore, the deconvolution finds the true image in Fourier domain by division.

$$F_{true}(u,v) = \frac{F(u,v)}{H(u,v)} \tag{4.30}$$

However, in practice this algorithm is not desirable, as it is sensitive to noise. In fact, mathematically most imaging tools are usually posed in the form of inverse problems. The mathematical description of this leads to an inverse problem where one wants to infer the spatial distribution of scatters, which is a coefficient in a diffusion-type equation. Regular linear and non-linear deconvolution techniques utilize a known PSF. The non-linear deconvolution can be performed iteratively, whereby each iteration improves the estimation of the restored image. Iterative methods include maximum-likelihood estimation (ML), maximum-a-posteriori estimation (MAP) and expectation-maximization algorithm (EM). A good estimate of the PSF is helpful for quicker convergence.

The iterative deconvolution methods developed for OCT usually require a priori information about the point-spread function (PSF) of the imaging optics. Experimentally the properties of the PSF can be obtained by averaging multiple scans towards a reflective mirror, and the modeling of scanning tissue is subjected to phantom studies. Some of the related research involving deconvolution can be found in the following references [88], [89], [90], [91] and [92]. A study by S. Paes and I.K. Hong [93] applied adaptive speckle filtering followed by iterative deconvolution. The authors reviewed various deconvolution methods and preliminary adaptive speckle filtering. A combination of the Frost filter and Richardson-Lucy deconvolution (ML algorithm) methods has shown superiority in noise reduction and speckle reduction, due to the Richardson-Lucy algorithm high noise resistance property. Most of the previous deconvolution work was investigated on 1-D OCT signal (A-scan) deconvolution. In this work, we extend the iterative deconvolution to the image as a whole by incorporating a deconvolution mask that is restrained by axial/longitudinal and lateral/transverse resolution limits.

The FWHM value which is calculated as full width at half the maximum of the PSF profile, is generally considered as the measure of spatial resolution. A narrow FWHM means better resolution whereas the wider FWHM presents worse resolution. The lateral resolution of the OCT system is defined as

$$R_L = \frac{2\ln 2}{\pi} \cdot \frac{\lambda_0^2}{\Delta\lambda} = l_c \tag{4.31}$$

where λ_0 is the center wavelength and $\Delta\lambda$ is the FWHM of the power spectrum. Ralston [94] has proposed that the transverse resolution and longitudinal resolution are uncorrelated. The longitudinal resolution is determined by the coherence length of the light source. The transverse resolution is characterized by the Gaussian beam profile incident on the sample and the confocal parameter. **Figure 4.16** illustrates the geometry of the Gaussian beam profiles at different numerical aperture (NA).

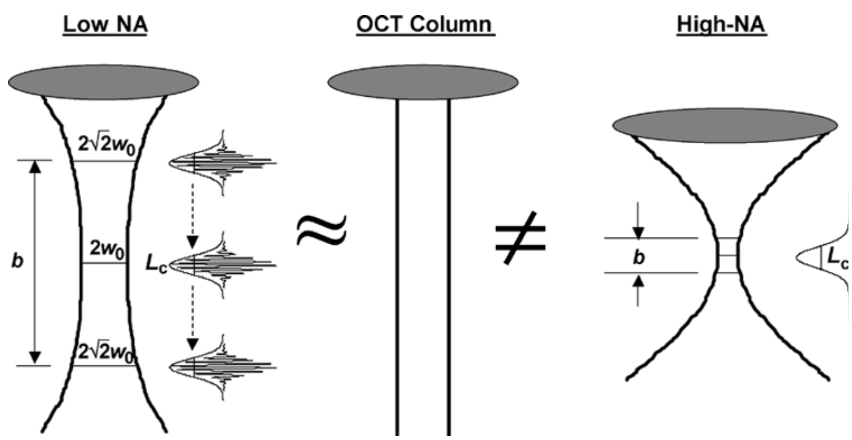

Figure 4.16 Geometry of a Gaussian beam for low and high NA lenses. *b* is the confocal parameter, ω_0 is the beam radius at the focus, and l_c is the coherence length of the source [94].

Typically in OCT, lenses with a lower NA are used, where a relatively uniform transverse resolution over the entire axial scan is preferred. The transverse resolution is determined by the diameter of the spot size $2\omega_0$, or equivalently by the width of the incident beam on the sample where the edges are determined by a decrease in intensity by a factor of $1/e^2$ and it is approximated by:

$$R_T \approx 2\omega_0 \approx 2.44\frac{f\lambda_0}{D} \tag{4.32}$$

where f is the focal length of the lens, D is the beam diameter incident on the objective lens, and λ_0 is the center wavelength. In our current OCT system, f = 25.6 mm, D = 4 mm and λ_0 = 1310 nm. An approximation of the transverse resolution is calculated as,

$$R_T \approx 2.44\frac{(25.6mm)(1310nm)}{4mm} \approx 20.45\mu m \tag{4.33}$$

As the longitudinal and transverse resolutions are properly defined, the next step is to first construct longitudinal and transverse PSFs with respect to the resolution requirement **Figure 4.17** is obtained by averaging 10 A-scans against a reflective mirror. The "delay" appearing on the second half of the PSF is possibly due to the thinness of the metal coating on the surface of the mirror which the OCT system is not able to resolve.

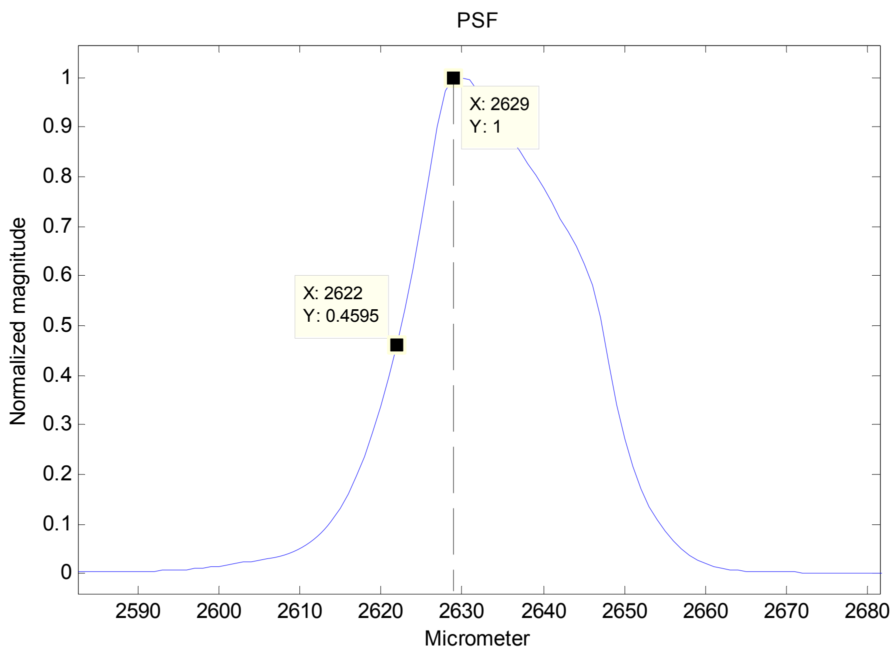

Figure 4.17 Results of averaging 10 A-scans and normalization of the magnitude.

By duplicating the first half of the original PSF, we create an ideal axial/longitudinal-direction PSF, shown in **Figure 4.18**. At FWHM, the width of the PSF is approximately 14 resolution cells. Each resolution cell is measured at 1 μm. Therefore the axial resolution, in this case, is 14 μm.

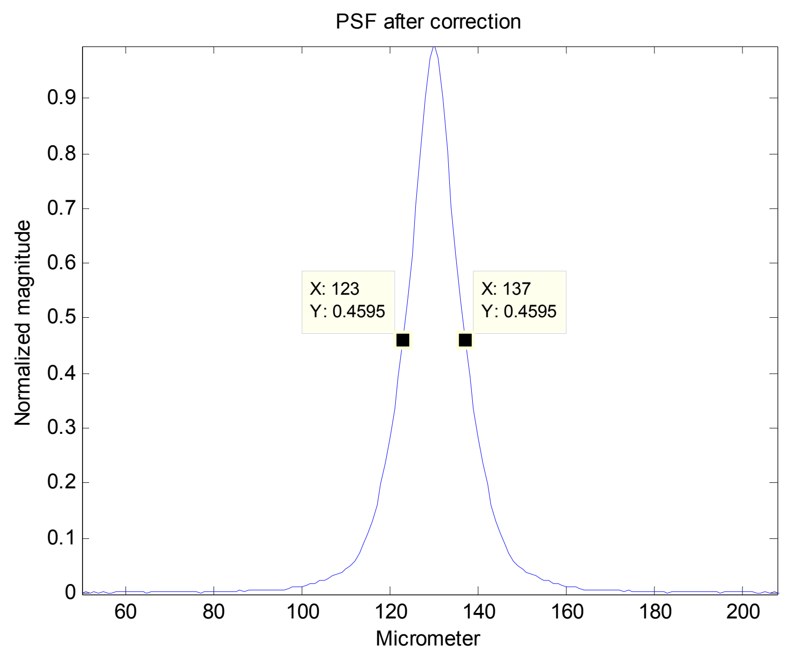

Figure 4.18 A reconstructed ideal PSF with matching axial resolution of 14 μm.

A separate PSF using Gaussian fitting is constructed satisfying the FWHM of 20 μm in the transverse direction is shown in **Figure 4.19**.

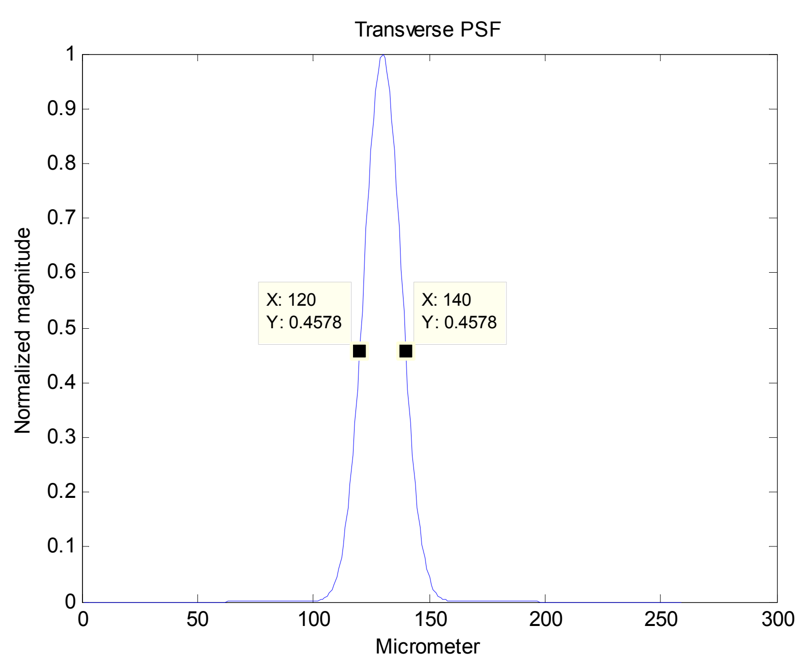

Figure 4.19 An ideal PSF with matching transverse resolution of 20 μm.

A deconvolution mask is consequently generated by convolving the longitudinal PSF and transverse PSF, and the iterative deconvolution process is thus ready to be used.

First a quick review of the Richardson-Lucy algorithm [95] [96] is discussed. A given image model f_M, which is the prior knowledge about the true image f_{true}, results in an observation f. The probability of the estimation $\hat{f}$ in turn is determined by a conditional probability function $p(\hat{f} \mid f)$. Two common statistical distributions for natural occurrences are Gaussian and Poisson distributions. Assuming the noise in different pixels is statistically independent, the joint probability of all the pixels is the product of the probabilities of the individual pixels. In practice, it is usually convenient to work with the log-likelihood function of the joint probability.

$$\ln\left[p\left(\hat{f} \mid f\right)\right] = \sum_i \ln\left[p\left(\hat{f}_i \mid f_i\right)\right] \tag{4.33}$$

where i denotes the individual pixel that gives rise to observed data. For a Poisson distribution, a simplified log-likelihood function after dropping the constants, is

$$\ln\left[p\left(\hat{f} \mid f\right)\right] = \sum_i \left(\hat{f}_i + f_i \ln \hat{f}_i\right) \tag{4.34}$$

The above non-linear log-likelihood function is minimized iteratively using multiplicative corrections:

$$\hat{f}^{(k+1)} = \left[h^T * \left(\frac{f}{\left(\hat{f} * h\right)^{(k)}}\right)\right] \cdot \hat{f}^{(k)} \tag{4.35}$$

where h^T is the transpose of the PSF h. The square brackets on the right-hand side enclose the factor by which the previous $\hat{f}^{(k)}$ is multiplied to give the new $\hat{f}^{(k+1)}$. The ratio between observation f and the estimation $\left(\hat{f} * h\right)^{(k)}$ from the previous iteration is back projected by the transpose of the PSF. It has also been shown empirically that if this iteration converges, it converges to the maximum likelihood solution.

On the representative graphs (**Figure 4.20**), **Figure 4.20-A** is the original image with speckle noise. **Figure 4.20-B** is the OCT image filtered by RKT algorithm (window size of 7 x 7). Strong surface intensity response and noise suppression can be observed. **Figure 4.20-C** and **Figure 4.20-D** are the regions near the air-tooth surface. The RKT filter has introduced resolution loss (blurring). After applying iterative convolution to both images with 20 iterations, we obtained **Figure 4.20-E** and **Figure 4.20-F**. The algorithm seems to provide good resolution enhancement. Note that in the parallel comparison between images without and with speckle reduction (**Figure 4.20-E** and **Figure 4.20-F,** respectively), the iterative deconvolution algorithm restores the sharpness near the edge by removing the blurry aspects of the RKT-filtered image. The advantage is also shown in the level of noise suppression by introducing speckle reduction prior to the iterative deconvolution, over straight forward applying deconvolution to the raw image (**Figure 4.20-E**). Thus a procedure combining spatial speckle reduction and iterative deconvolution is used to optimize the process of noise suppression and resolution restoration.

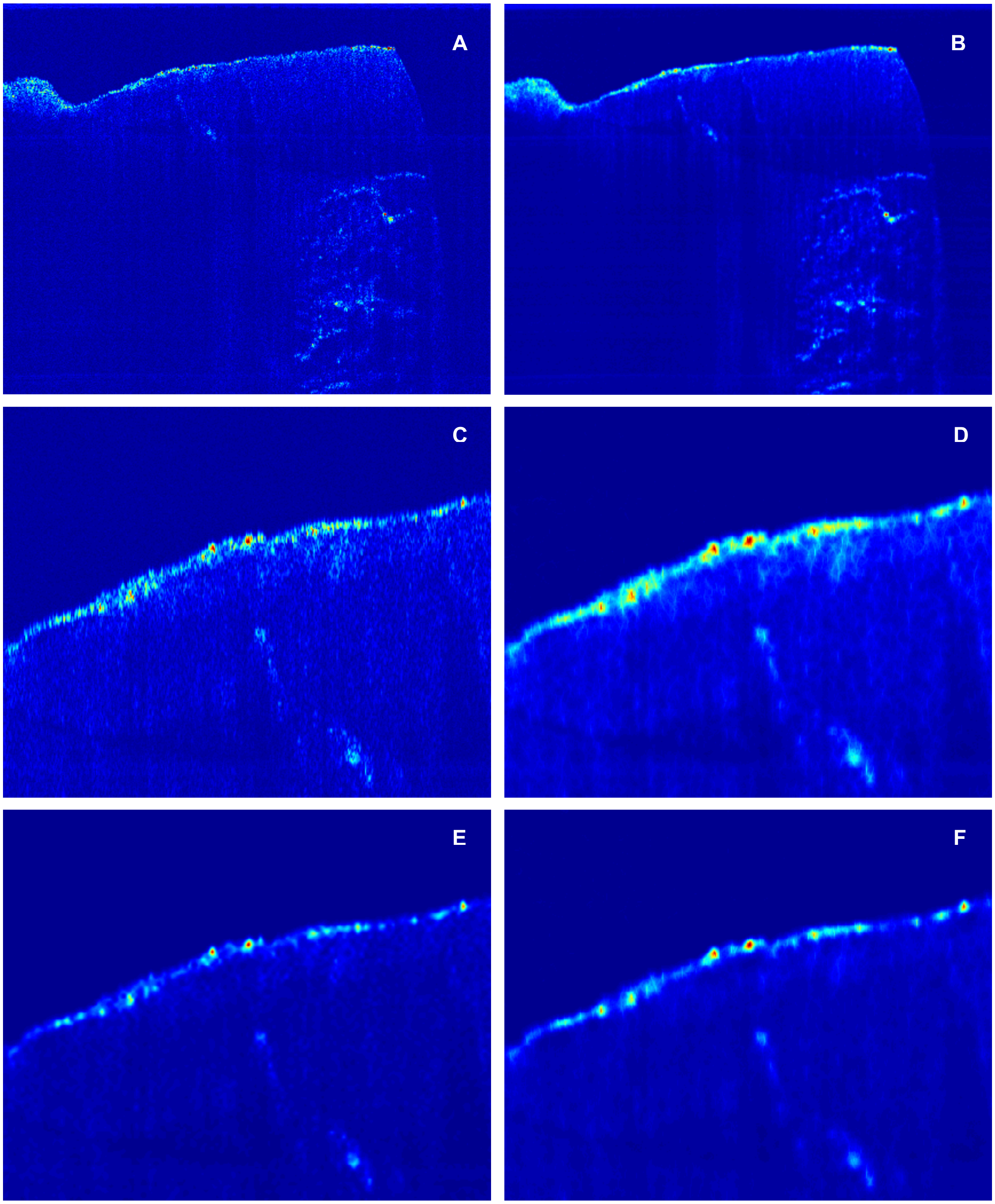

Figure 4.20 Results of applying iterative deconvolution algorithms to an original image and RKT filtered image. Image **A** is original OCT image. Image **B** is the OCT image filtered by RKT algorithm. The resolution loss is introduced (comparing with **C** and **D**). Image **E** is the restored image from raw observation. Image **F** is image after applying deconvolution to noise reduced image.

In summary, the effects of speckle reduction on raw OCT images are demonstrated, where the presence of speckle often obscures the underlying image content and reduces the interpretability of the image. Substantially reducing the speckle noise while effectively preserving image detail are two important speckle reduction considerations. In many applications, it is the balance between these two considerations that determines the success of a speckle suppression filter. For this reason, a cross examination of potential speckle reduction filters was performed. The optimal choice of speckle filter is an attempt of integrating the advantages of speckle reduction and denoised image visual interpretation. The performance of both spatial domain and wavelet domain filters was evaluated using a number of quantitative criteria. These included SNR, PSNR, ENL, CSR and SSIM. Three sets of OCT images were tested for evaluation purposes. The superiority of wavelet domain filtering is able to achieve effective speckle noise reduction while preserving details. For the simple purpose of OCT image restoration, wavelet domain filtering is a preferable choice.

Chapter 5

Caries Lesion Segmentation

5.1 Region-based Active Contour

A second purpose of speckle suppression, besides providing a visual aid to obtain a correct diagnosis, is to serve as a pre-processing step for region segmentation. In this application, speckle is considered noise in the image that prohibits classical segmentation algorithms from working optimally. The main goal of image segmentation, which plays an essential role in both qualitative and quantitative image analysis, is to divide an image into sets of regions that are visually distinct and uniform with respect to some property, such as gray level, texture, or color. Image segmentation is strongly influenced by the quality of the image data, and the lesion segmentation performance is severely degraded owing to the speckle, tissue textures, and other artifacts resulting from the imaging process.

The segmentation techniques on speckle contaminated images have been well investigated in the area of ultrasound medical imaging. Many methods, including thresholding, region growing, watershed, Markov random fields and active contours, [97], [98], [99], [100] and [101] were proposed. For this work, OCT image segmentation methods focus on the following main approaches: 1) thresholding technique, 2) region-based active contour segmentation technique.

In general active contour models, a contour is initiated on the images and is left to deform in a way that, firstly, moves it towards the features of interests in the image and, then maintain a certain degree of smoothness and continuity in the contour. In order to favor this type of contour deformation, an energy term is associated with the contour and is designed to be inversely proportional to the contour's smoothness and fit to desired image features. The deformation of the contour in the image plane will change its energy, thus one can imagine an energy surface on top of which the contour moves seeking the valleys of low energy.

Level sets based on active contour models can be divided into two categories: edge-based contour and region-based contour. Edge-based active contour models utilize image gradients in order to identify object boundaries [102]. This type of highly localized image information is adequate in some situations, but has been found to be very sensitive to image noise. Region-based active contour models the foreground and background regions statistically and find an energy optimum where the model best fits the image. More advanced techniques attempt to model regions by known distributions, intensity histograms, texture maps, or structure tensors. More recently, work in active contours has been focused on incorporating region statistical information. This investigation is inspired by the region-competition work of Chesnaud et al [103], who present a frame work for segmentation of images with various statistical models. Sarti *et al* [101] extended this work for the case of Rayleigh distributions. In this study, we apply a similar approach for segmenting OCT images. To deal with the low signal to noise ratio in OCT images, contour shapes are described using low order parametric deformable models. This low order parameterization is sufficient to accommodate the expected shape and size variations, yet provides robustness against noise, image artifacts and regions of missing data.

This approach consists of a maximum likelihood estimation approach to parametric deformable models. The basic building block is a probabilistic observation model $p(f(x,y)\mid\omega)$ characterizing the observed data $f(x,y)$ with the conditional class parameter ω. ω denotes a binary window function that defines a certain shape of the object (i.e. lesion) so that $\omega(x,y)$ is equal to one within the object and to zero elsewhere. Then the image is composed of two regions $\Omega_i = \{(x,y)\mid\omega(x,y)=1\}$ and $\Omega_o = \{(x,y)\mid\omega(x,y)=0\}$. "$i$" and "$o$" subscripts describe the locations of the observation either "inside" or "outside" ω. The purpose of the segmentation is, therefore, to estimate the most likely shape ω for the lesion. To achieve this estimation, different shape descriptions could be used to define ω. Here we only apply our approach to polygonal description. We assume that $p(f(x,y)\mid\omega)$ has a known parametric form (in this case, Rayleigh distribution for OCT speckles), and is therefore determined uniquely by the value of a parameter vector θ. For instance, we have $p(f(x,y)\mid\omega_i,\theta_i)$ and $p(f(x,y)\mid\omega_o,\theta_o)$ for each of the regions inside and outside the polygon. The assumption is that suppose the pixels (observations) are independent and identically distributed random variables drawn from domain f, which contains observations/samples $f(x,y)$, $(x,y)\in\Omega_i,\Omega_o$. Then the joint probability density function of the observed image, given a parameter vector θ, can be written as,

$$p(f\mid\omega,\theta) = p(f\mid\omega_i,\theta_i)\cdot p(f\mid\omega_o,\theta_o) \tag{5.1}$$

The right hand of the equation is the *likelihood* function of (ω,θ), and can be written as the joint probabilities of individual observations.

$$p(f \mid \omega,\theta)=\prod_{(x,y)\in\Omega_o} p(f(x,y)\mid \omega_o,\theta_o)\cdot \prod_{(x,y)\in\Omega_i} p(f(x,y)\mid \omega_i,\theta_i) \quad (5.2)$$

To show the dependence of $p(f \mid \omega,\theta)$ on θ explicitly, we write $p(f \mid \theta)$ as $p(f \mid \omega,\theta)$. Now the problem is simplified to only use the information provided by the observations to obtained good estimates for the unknown parameter vector θ.

$$p(f \mid \theta)=\prod_{(x,y)\in\Omega_o} p(f(x,y)\mid \theta_o)\cdot \prod_{(x,y)\in\Omega_i} p(f(x,y)\mid \theta_i) \quad (5.3)$$

The *maximum-likelihood* estimate of θ is, by definition, the value $\hat{\theta}$ that maximizes $p(f \mid \theta)$. Since the log function is strictly increasing, the maximum value of $p(f \mid \theta)$ will occur at the same points as the maximum value of $l(f,\theta)=\log(p(f \mid \theta))$

This function is the *log-likelihood* function and in many cases it is easier to work with it than with the likelihood function. Indeed the product structure of the probability function is transformed in a summation or integral structure of the log-likelihood. We need to maximize the function $l(f,\theta)$, that is,

$$\hat{\theta}=\arg\max_{\theta} l(\theta) \quad (5.4)$$

Therefore, the log-likelihood function has become,

$$\begin{aligned} l(f,\theta)=\ln(p(f \mid \theta)) &= \sum_{(x,y)\in\Omega_o} \ln(p(f(x,y)\mid \theta_o)) + \\ &+ \sum_{(x,y)\in\Omega_i} \ln(p(f(x,y)\mid \theta_i)) \end{aligned} \quad (5.5)$$

Given that OCT images follow a Rayleigh distribution, the pixel marginal probability densities have the form,

$$p(f(x,y)\mid\sigma)=\frac{f(x,y)}{\sigma^2}\exp\left(-\frac{f(x,y)^2}{\sigma^2}\right) \tag{5.6}$$

And in this case, $\theta=\sigma=[\theta_o,\theta_i]=[\sigma_o,\sigma_i]$, where σ_o and σ_i are the variances of the inside and outside polygon respectively.

$$\begin{aligned} l(f,\theta)=&\sum_{(x,y)\in\Omega_o}\ln\left(\frac{f(x,y)}{\theta_o^2}\exp\left(-\frac{f(x,y)^2}{\theta_o^2}\right)\right)+ \\ &+\sum_{(x,y)\in\Omega_i}\ln\left(\frac{f(x,y)}{\theta_i^2}\exp\left(-\frac{f(x,y)^2}{\theta_i^2}\right)\right) \end{aligned} \tag{5.7}$$

Since the dependence on f is implicit, thus we have from the above equation,

$$\begin{aligned} l(\theta)=&\sum_{(x,y)\in\Omega_o}\left(\ln(f(x,y))-\ln(\theta_o^2)-\frac{f(x,y)^2}{\theta_o^2}\right)+ \\ &+\sum_{(x,y)\in\Omega_i}\left(\ln(f(x,y))-\ln(\theta_i^2)-\frac{f(x,y)^2}{\theta_i^2}\right) \end{aligned} \tag{5.8}$$

and

$$\nabla_\theta l(\theta)=\sum_{(x,y)\in\Omega_o}\nabla_\theta\ln p(f(x,y)\mid\theta_o)+\sum_{(x,y)\in\Omega_i}\nabla_\theta\ln p(f(x,y)\mid\theta_i) \tag{5.9}$$

Thus, the necessary condition for the maximum-likelihood estimate for θ can be obtained by setting,

$$\nabla_\theta l(\theta)=0 \tag{5.10}$$

A solution $\hat{\theta}=\arg\max_\theta l(\theta)$ represents the maximum, and two sets of equation are derived.

$$\begin{cases} \sum\limits_{(x,y)\in\Omega_o} \nabla_{\theta_o} \ln p(f(x,y) \mid \theta_o) = 0 \\ \sum\limits_{(x,y)\in\Omega_i} \nabla_{\theta_i} \ln p(f(x,y) \mid \theta_i) = 0 \end{cases} \tag{5.11}$$

Or equivalently,

$$\begin{cases} \sum\limits_{(x,y)\in\Omega_o} \nabla_{\theta_o} \left(\ln(f(x,y)) - \ln(\theta_o^2) - \dfrac{f(x,y)^2}{\theta_o^2} \right) = 0 \\ \sum\limits_{(x,y)\in\Omega_i} \nabla_{\theta_i} \left(\ln(f(x,y)) - \ln(\theta_i^2) - \dfrac{f(x,y)^2}{\theta_i^2} \right) = 0 \end{cases} \tag{5.12}$$

Then solve for $\hat{\theta}_o$ and $\hat{\theta}_i$

$$\begin{cases} \hat{\theta}_o = \dfrac{\sum\limits_{(x,y)\in\Omega_o} f(x,y)^2}{N_o} \\ \hat{\theta}_i = \dfrac{\sum\limits_{(x,y)\in\Omega_i} f(x,y)^2}{N_i} \end{cases} \tag{5.13}$$

where N_o and N_i are the number of pixels outside and inside the polygon. Now we can introduce these two estimations in the log-likelihood function, and we can write,

$$\begin{aligned} l(\hat{\theta}) = & \sum_{(x,y)\in\Omega_o} \left(\ln(f(x,y)) - \ln(\hat{\theta}_o^2) - \frac{f(x,y)^2}{\hat{\theta}_o^2} \right) + \\ & + \sum_{(x,y)\in\Omega_i} \left(\ln(f(x,y)) - \ln(\hat{\theta}_i^2) - \frac{f(x,y)^2}{\hat{\theta}_i^2} \right) \end{aligned} \tag{5.14}$$

Now substituting the maximum estimations for $\hat{\theta}_o$ and $\hat{\theta}_i$.

$$l(\hat{\theta}) = \sum_{(x,y)\in\Omega} \ln(f(x,y)) + \sum_{(x,y)\in\Omega_o} \left(-\ln\left(\frac{\sum_{(x,y)\in\Omega_o} f(x,y)^2}{N_o} \right) - \frac{f(x,y)^2}{\frac{\sum_{(x,y)\in\Omega_o} f(x,y)^2}{N_o}} \right)$$

$$+ \sum_{(x,y)\in\Omega_i} \left(-\ln\left(\frac{\sum_{(x,y)\in\Omega_i} f(x,y)^2}{N_i} \right) - \frac{f(x,y)^2}{\frac{\sum_{(x,y)\in\Omega_i} f(x,y)^2}{N_i}} \right) \tag{5.15}$$

After simplification we have,

$$l(\hat{\theta}) = -\sum_{(x,y)\in\Omega_o} \ln\left(\frac{1}{N_o} \sum_{(x,y)\in\Omega_o} f(x,y)^2 \right) -$$

$$-\sum_{(x,y)\in\Omega_i} \ln\left(\frac{1}{N_i} \sum_{(x,y)\in\Omega_i} f(x,y)^2 \right) - \left(N_o^2 + N_i^2\right) + \sum_{(x,y)\in\Omega} \ln(f(x,y)) \tag{5.16}$$

The last two terms on the right hand of this equation do not depend on the shape of the polygon and thus can be omitted. Then we obtain the following expression for $l(\hat{\theta})$

$$l(\hat{\theta}) = -N_o \ln\left(\frac{1}{N_o} \sum_{(x,y)\in\Omega_o} f(x,y)^2 \right) - N_i \ln\left(\frac{1}{N_i} \sum_{(x,y)\in\Omega_i} f(x,y)^2 \right) \tag{5.17}$$

This is also an identical expression for the Rayleigh distribution, which has been referred by Chesnaud [103]. The following task is to embed this likelihood function as part of the region-based contour energy function that has been described by Chan [100]. According to Chan, a length term that has been introduced as regularization in the shape of the curve, and finally we ask to minimize the functional:

$$F(C) = \mu \cdot length(C) + l(\hat{\theta})$$

$$F(C) = \mu \cdot length(C) - N_o \ln\left(\frac{1}{N_o} \sum_{(x,y)\in\Omega_o} f(x,y)^2\right) - N_i \ln\left(\frac{1}{N_i} \sum_{(x,y)\in\Omega_i} f(x,y)^2\right) \quad (5.18)$$

To implement the polygon/contour as a deformable mask that was mentioned as the beginning of this chapter, the energy function can be written using Heaviside function $H(\varphi)$, and in the mean time we replace the summation with integral,

$$\begin{aligned} F(C) = \mu \cdot \int_{\Omega} |\nabla H(\varphi)| dxdy - N_i \ln\left(\frac{1}{N_i} \int_{(x,y)\in\Omega_i} f(x,y)^2 H(\varphi) dxdy\right) \\ - N_o \ln\left(\frac{1}{N_o} \int_{(x,y)\in\Omega_o} f(x,y)^2 (1 - H(\varphi)) dxdy\right) \end{aligned} \quad (5.19)$$

Also the pixel values are replaced by the Heaviside function, where:

$$\begin{cases} N_i = \int_{\Omega} H(\varphi) dxdy \\ N_o = \int_{\Omega} (1 - H(\varphi)) dxdy \end{cases} \quad (5.20)$$

and

$$length(\varphi = 0) = \int_{\Omega} |\nabla H(\varphi)| dxdy = \int_{\Omega} \delta(\varphi) |\nabla \varphi| dxdy \quad (5.21)$$

After minimizing with respect to φ, the associated Euler-Lagrange equations for φ are deduced. Parameterizing the descent direction by time $t \geq 0$, the equation in $\varphi(t, x, y)$ is,

$$\frac{\partial \varphi}{\partial t} = |\nabla \varphi| \left[\mu div\left(\frac{\nabla \varphi}{|\nabla \varphi|} \right) + \right.$$

$$+ \ln\left(\frac{1}{N_i} \int_{(x,y)\in\Omega_i} f(x,y)^2 dxdy \right) + \frac{N_i f(x,y)^2 - \int_{(x,y)\in\Omega_i} f(x,y)^2 dxdy}{\int_{(x,y)\in\Omega_i} f(x,y)^2 dxdy} -$$

$$\left. - \ln\left(\frac{1}{N_o} \int_{(x,y)\in\Omega_o} f(x,y)^2 dxdy \right) + \frac{N_i f(x,y)^2 - \int_{(x,y)\in\Omega_o} f(x,y)^2 dxdy}{\int_{(x,y)\in\Omega_o} f(x,y)^2 dxdy} \right] \qquad (5.22)$$

The initial condition $\varphi(x,y,0) = \varphi_0(x,y)$ defines the initial contour. $\frac{\delta(\varphi)}{|\nabla \varphi|}\frac{\partial \varphi}{\partial \vec{n}}$ is the boundary conditions, where $\vec{n}$ denotes the exterior normal to the boundary $\partial\Omega$, and $\partial\varphi / \partial\vec{n}$ denotes the normal derivative of φ at the boundary. The numerical approximation was carried out in a similar fashion using finite difference approximation that is described by the Chan-Vese method in [100].

5.2 Lesion Segmentation Results

In this study, the method is applied to all three sets of OCT images. As mentioned earlier, speckle statistics are not known. We here first outline how to validate some of the parameters from the noisy image. The statistics of Rayleigh speckle are uniquely determined by the speckle contrast (variance). The spatial-domain method is based on the assumption that an image has many regions of almost uniform intensity and most changes in these regions of insignificant variations are due to speckle noise. The proposed algorithm is applied to the second set of OCT images, shown in **Figure 5.1**. The lesion boundaries are marked with dark lines. The lesion segmentation algorithm is applied individually to each image with different de-noising filtering prior to the segmentation process. The final image outlines the boundaries of areas of possible lesions. After setting an initial contour and the evolution process of the contour shrinking, in most cases, the contour reaches the convergence around 250 iterations, and the evolving contour can reach the real upper boundary in less than 100 iterations.

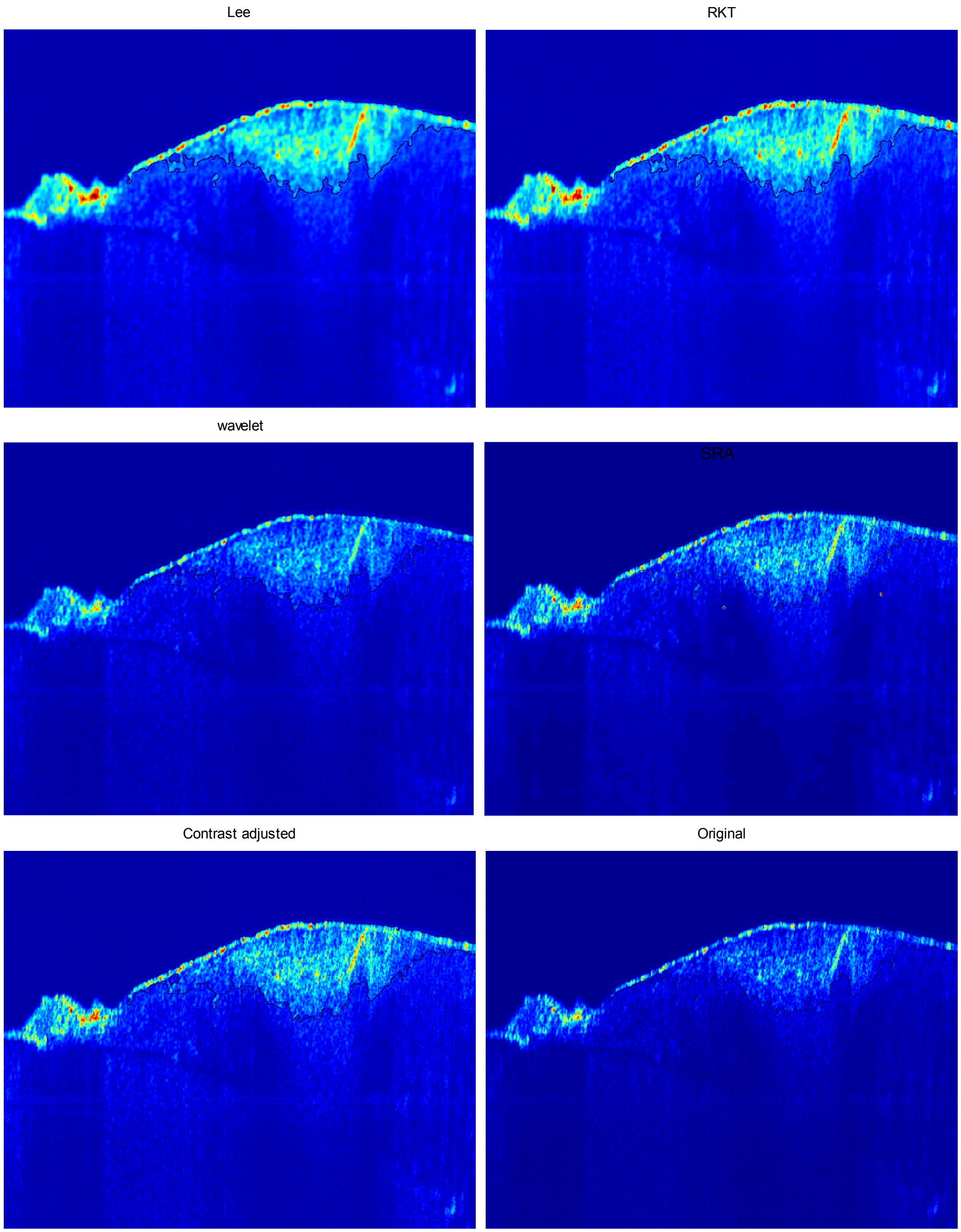

Figure 5.1 Results of applying region-based contour algorithm to 1310 nm images. The images only show the zoomed area near the carious lesion.

We can observe that the algorithm converges to the right contour even when directly applied to raw OCT image (**Figure 5.1**). The underlying difference in image intensity, which is not visible before contrast adjustment, still provides sufficient information for successful region-based segmentation. With proper contrast adjustment and speckle filtering, the algorithm produces similar segmentation results. The Lee and RKT filters seem to provide a smoother contour, and better contrast. Similar procedures were applied to the first set of 1310 nm OCT images (**Figure 5.2**). With less resolution, the convergence time is less than 200 iterations. The lesion is located near the surface of the tooth. The algorithm seems to provide satisfying results with both original image and filtered images. The contour also includes the regions of surface reflection as part of the contour. The depth measure of the lesion is much greater than normal surface reflection, and also the pixel intensity is another characteristic parameter to determine the possible lesion region. Finally, the algorithm is applied to 850 nm images that has lower signal to noise ratio compared to 1310 nm images (**Figure 5.3**). Again for most of the images, both original and filtered, the contour converges with similar shape regardless of whether the speckle reduction is applied or not.

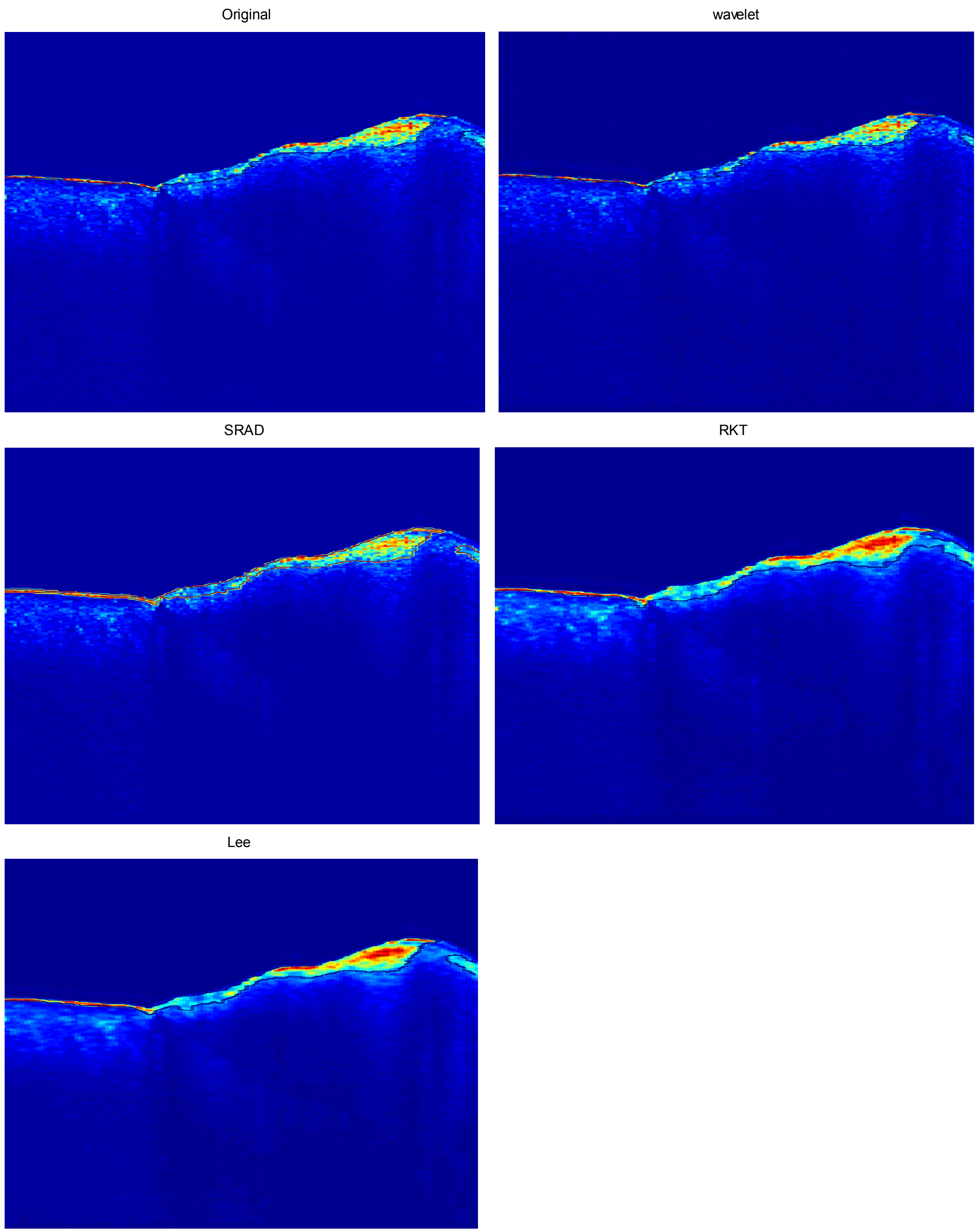

Figure 5.2 Results of applying region-based contour search algorithm to the first set of 1310 nm OCT images. Lesions are highlighted with dark lines.

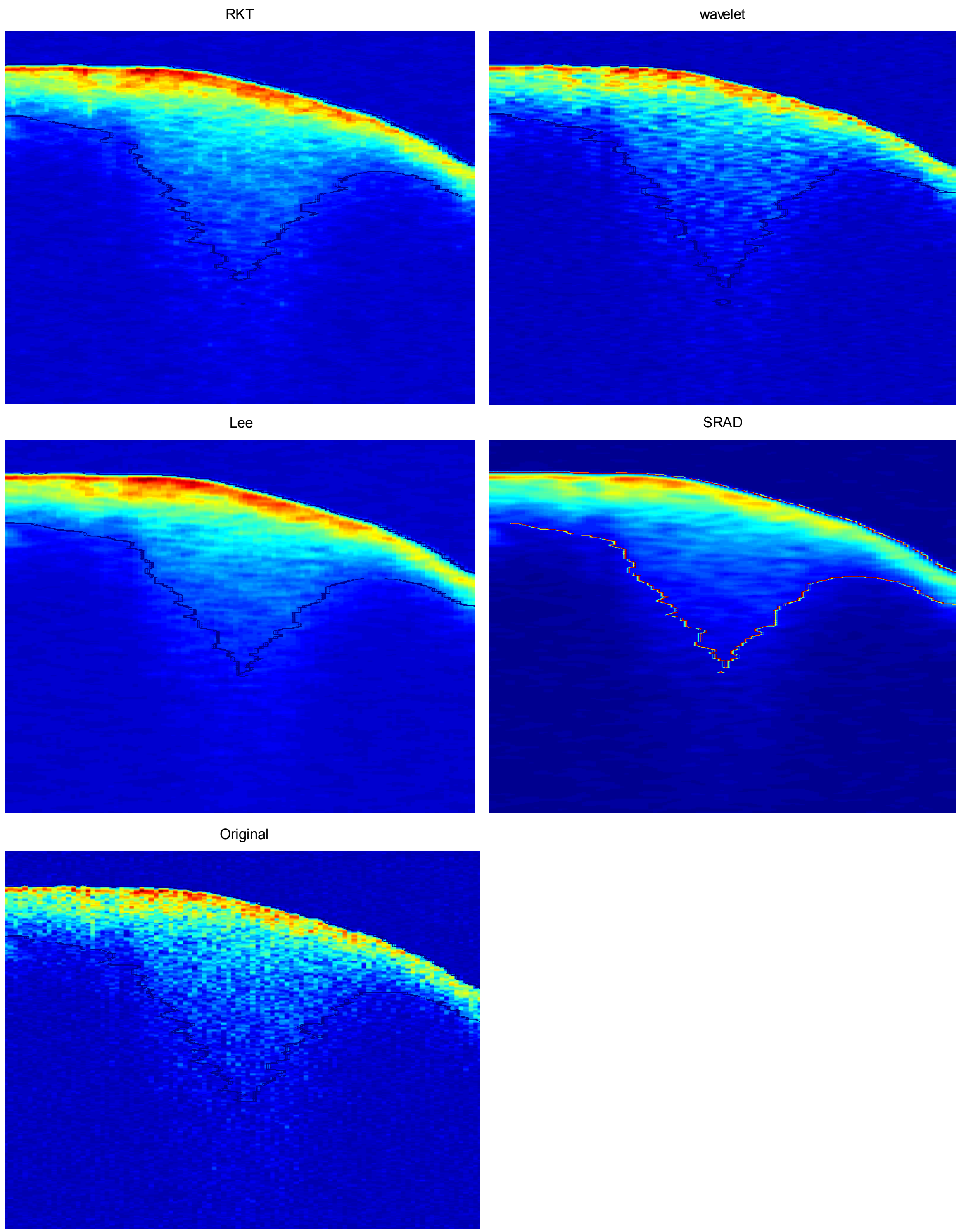

Figure 5.3 Results of applying contour algorithm to 850 nm OCT images.

To determine the reliability of the segmentation results versus the “true image”, the histology images of the tooth are shown in **Figure 5.4**. The results of the segmentation were assessed by comparing the disease-indicating areas found by the region-based contour and areas assessed by global thresholding. Images on the left column are the original 850 nm OCT images of tooth sample with different lesion depths. Images in the middle column are filtered with 11 × 11 median filter to retain the sharp edges. For comparison, the black lines are the direct results of region-based contour algorithm. The contours outlined by white lines are results of global thresholding and contouring of the binary images. Images from the third column are the histology images of the corresponding teeth. In essence, it is a comparison of OCT image segmentation results and histology images from the same sample. From visual examination when comparing with the histology images, the region-based contour algorithm seems to under-segment the lesion. This might greatly be due to the fact that the assumption of Rayleigh distribution model is not appropriate for 850 nm images. The algorithm tends to converge to the region where the pixels intensity is higher (yellow and red regions near the surface). The global thresholding is applied to the same filtered images and with the same global threshold level, the contour in white line appears to confine with better approximation to the “gold standard”.

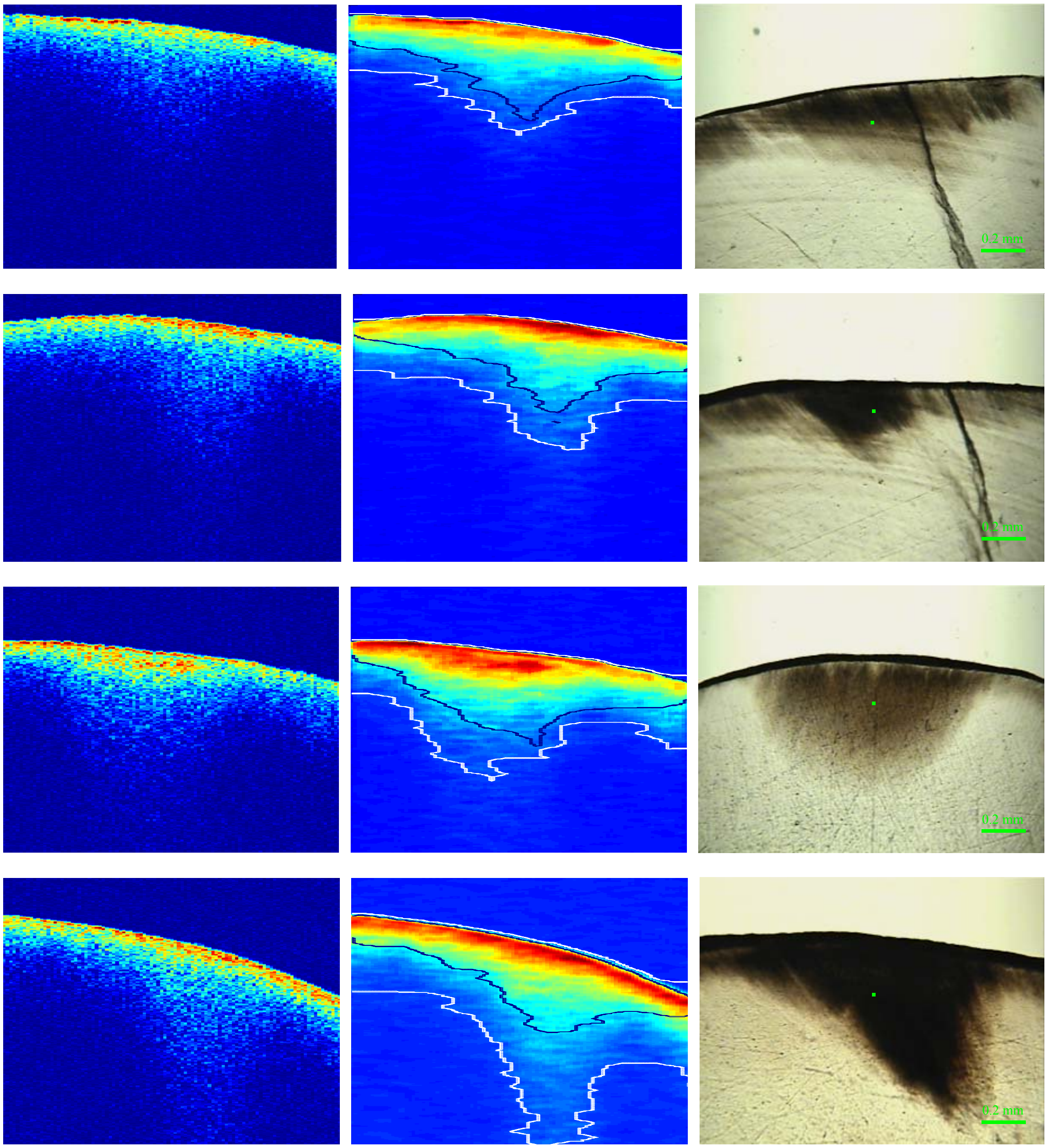
0.2 mm
0.2 mm
0.2 mm
0.2 mm

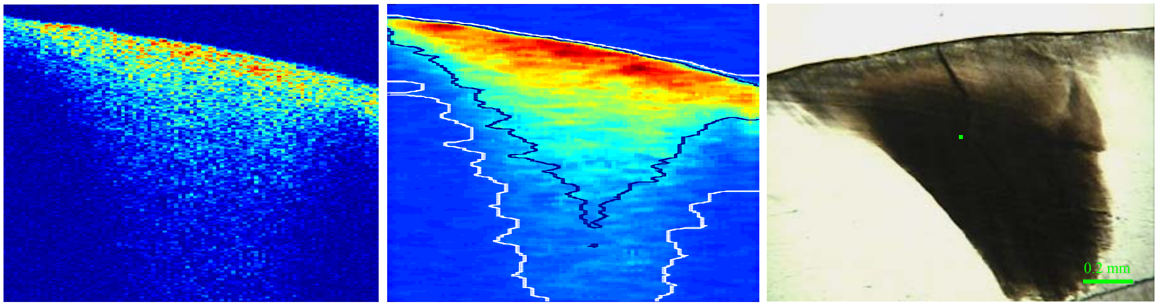

Figure 5.4 Results of region-based contour algorithm (blue lines) and global thresholding methods (white lines). The contour shape is compared with histological sectioning images of the samples.

For a wide range validation of the segmentation algorithm, the region-based contour search technique is applied to 14 images acquired at 1310 nm. Half of the images have carious lesion present and the other half are sound teeth. They are arranged in the way that two images (one carious and one sound) taken from the same sample, are placed in parallel for comparison. For example the two images from the first row in **Figure 5.6**, two images are acquired from the same tooth. Usually the carious and sound tooth images are taken with a few B-scans apart, which means the carious tooth image is the measure at the location of caries and the sound tooth image is scanned at the nearby location. Such comparison is based on the similarity in anatomical features (i.e. the location of DEJ) and parameter setting (i.e. same instrument and same sample). **Figure 5.5-5.10**, are the 7 sets of images from 7 individual tooth samples. The contrast adjustment parameters were set identically in all 14 images. Then a window size of 7×7 RKT filter was applied to these images. For each image, a carefully selected initial contour is placed near the lesion region, to avoid large number of interactions that are associated with inappropriate contour initialization. The number of iterations ranges from 200 ~ 300 for contour convergences. At the writing of the thesis, the tooth samples have not yet been histologically sectioned for examination by light microscopy as the samples are part of a larger study.

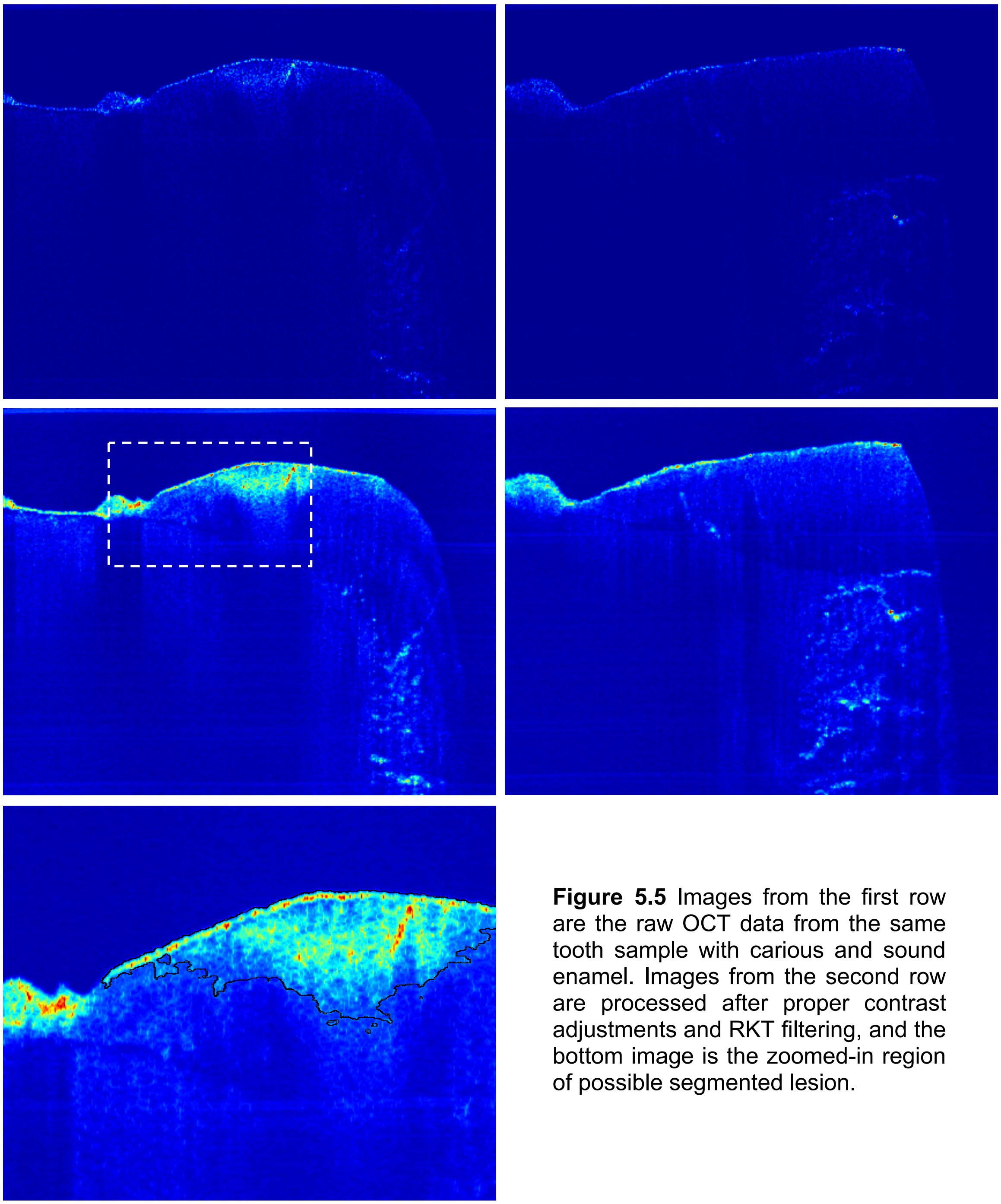

Figure 5.5 Images from the first row are the raw OCT data from the same tooth sample with carious and sound enamel. Images from the second row are processed after proper contrast adjustments and RKT filtering, and the bottom image is the zoomed-in region of possible segmented lesion.

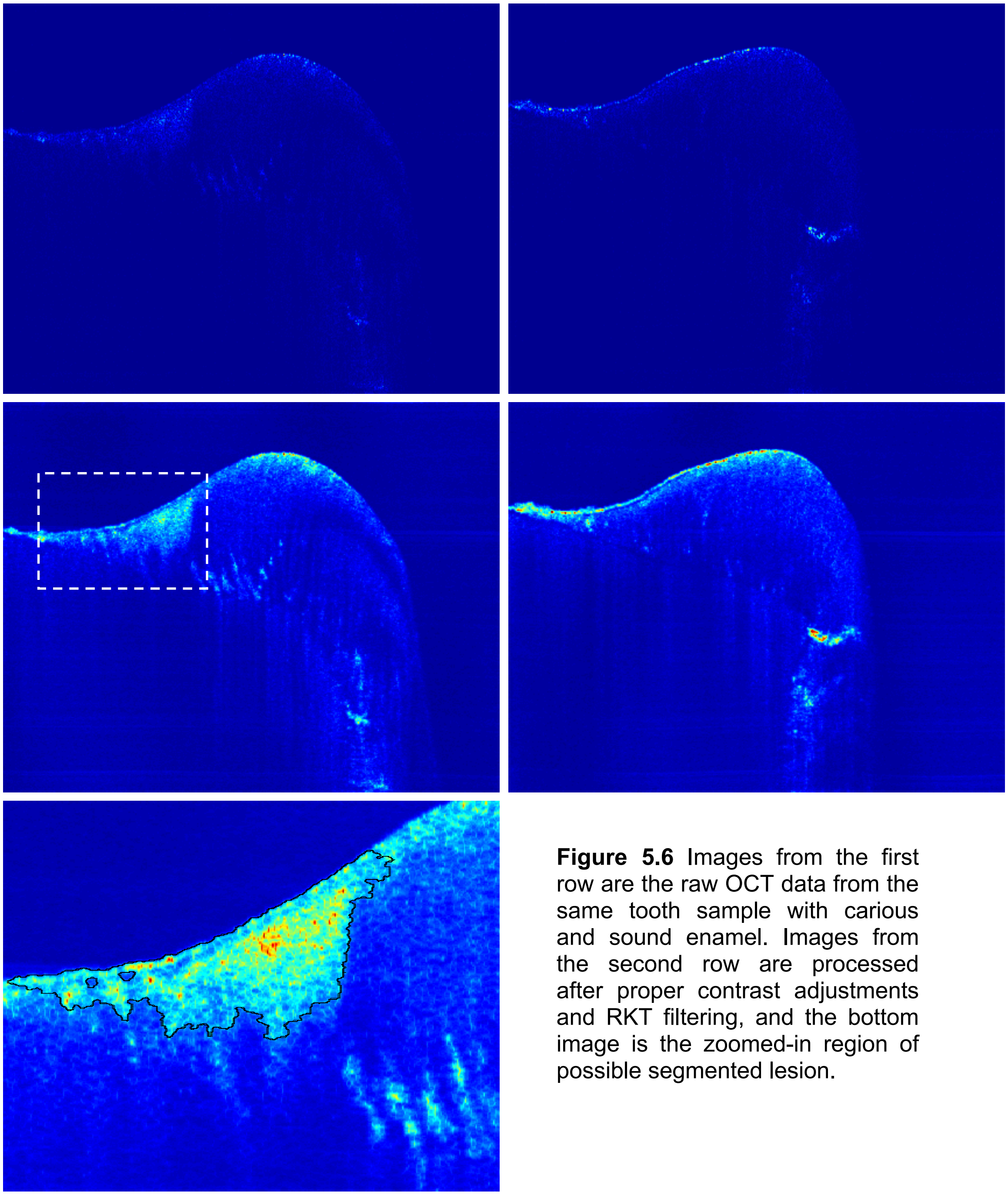

Figure 5.6 Images from the first row are the raw OCT data from the same tooth sample with carious and sound enamel. Images from the second row are processed after proper contrast adjustments and RKT filtering, and the bottom image is the zoomed-in region of possible segmented lesion.

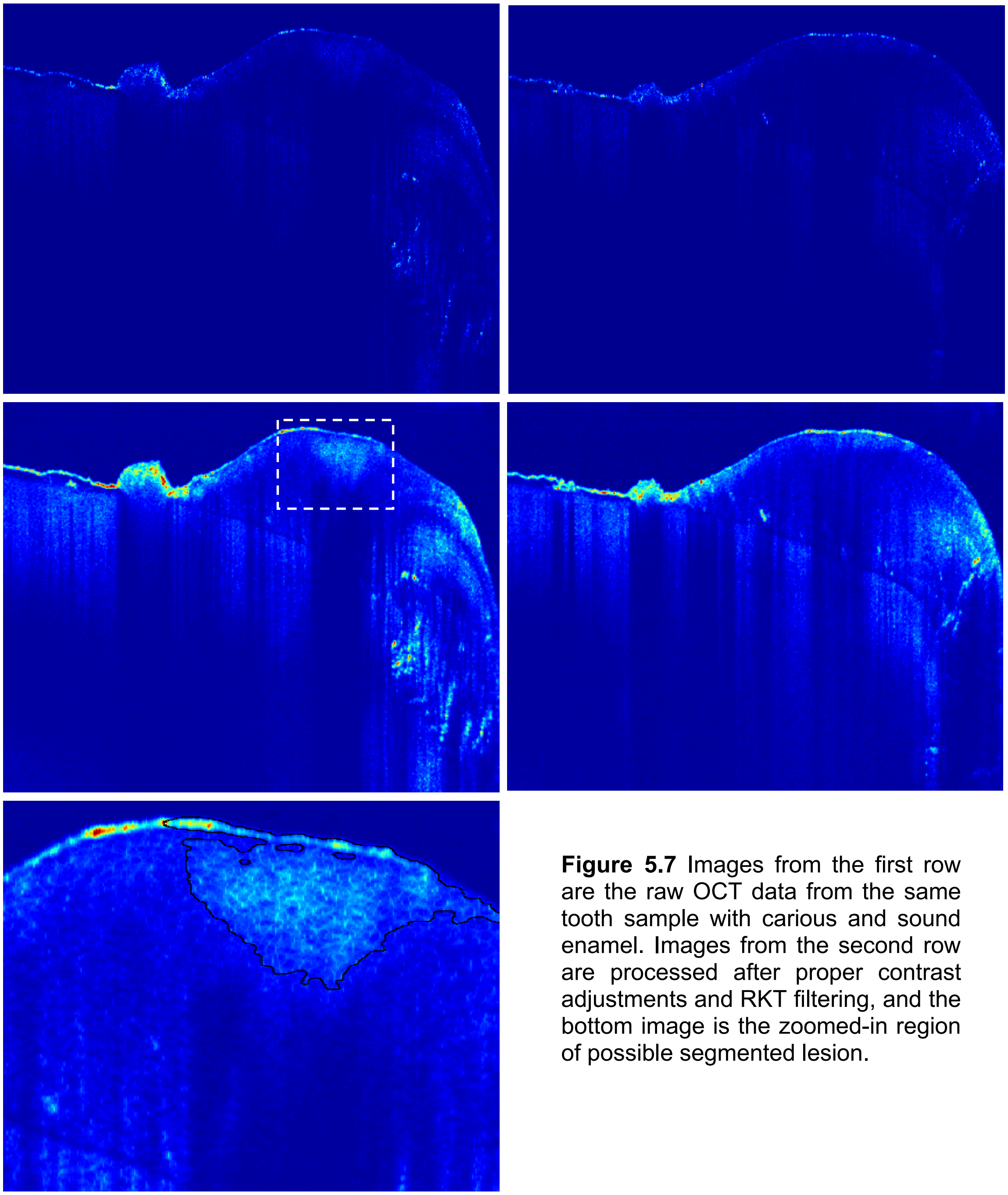

Figure 5.7 Images from the first row are the raw OCT data from the same tooth sample with carious and sound enamel. Images from the second row are processed after proper contrast adjustments and RKT filtering, and the bottom image is the zoomed-in region of possible segmented lesion.

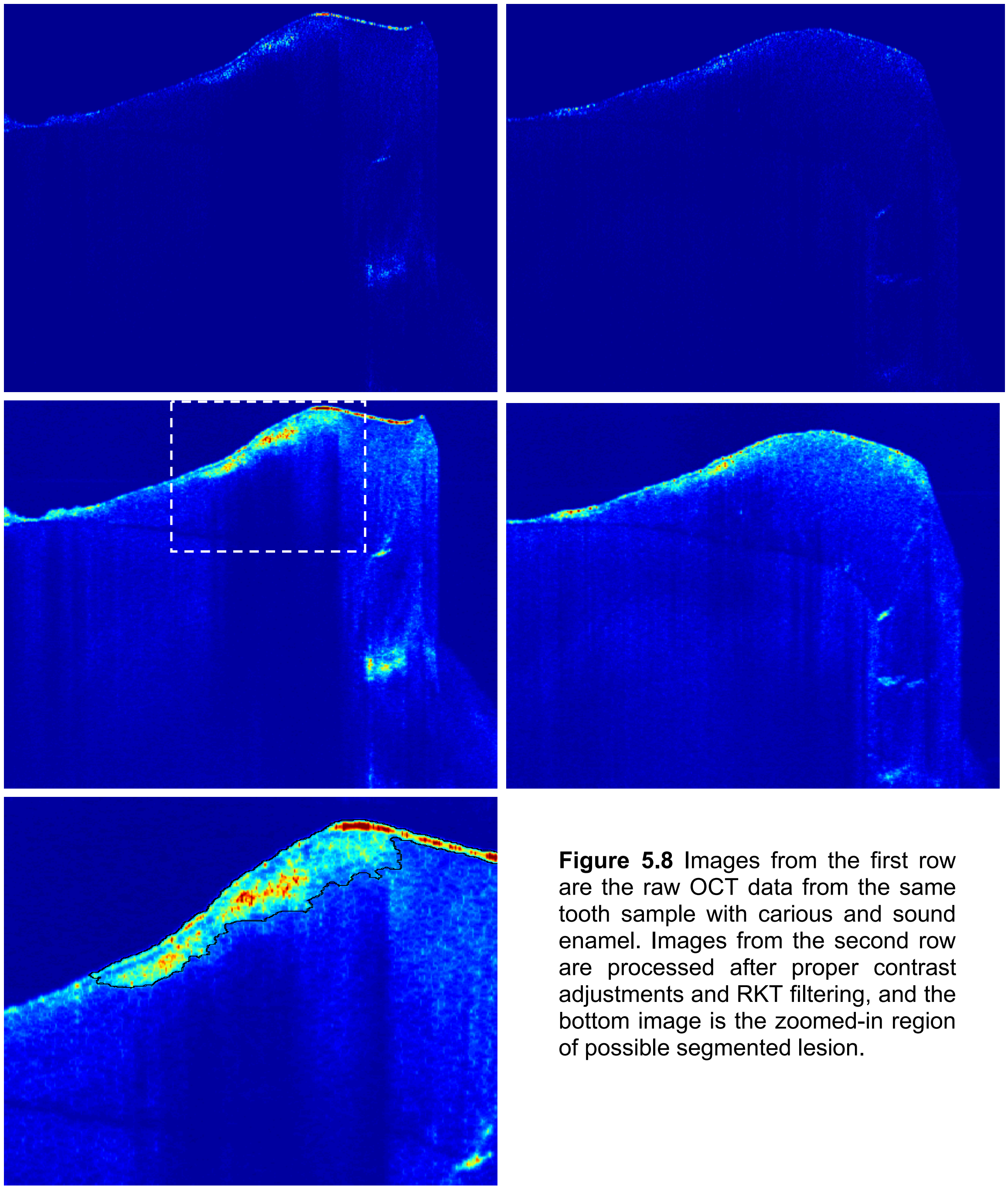

Figure 5.8 Images from the first row are the raw OCT data from the same tooth sample with carious and sound enamel. Images from the second row are processed after proper contrast adjustments and RKT filtering, and the bottom image is the zoomed-in region of possible segmented lesion.

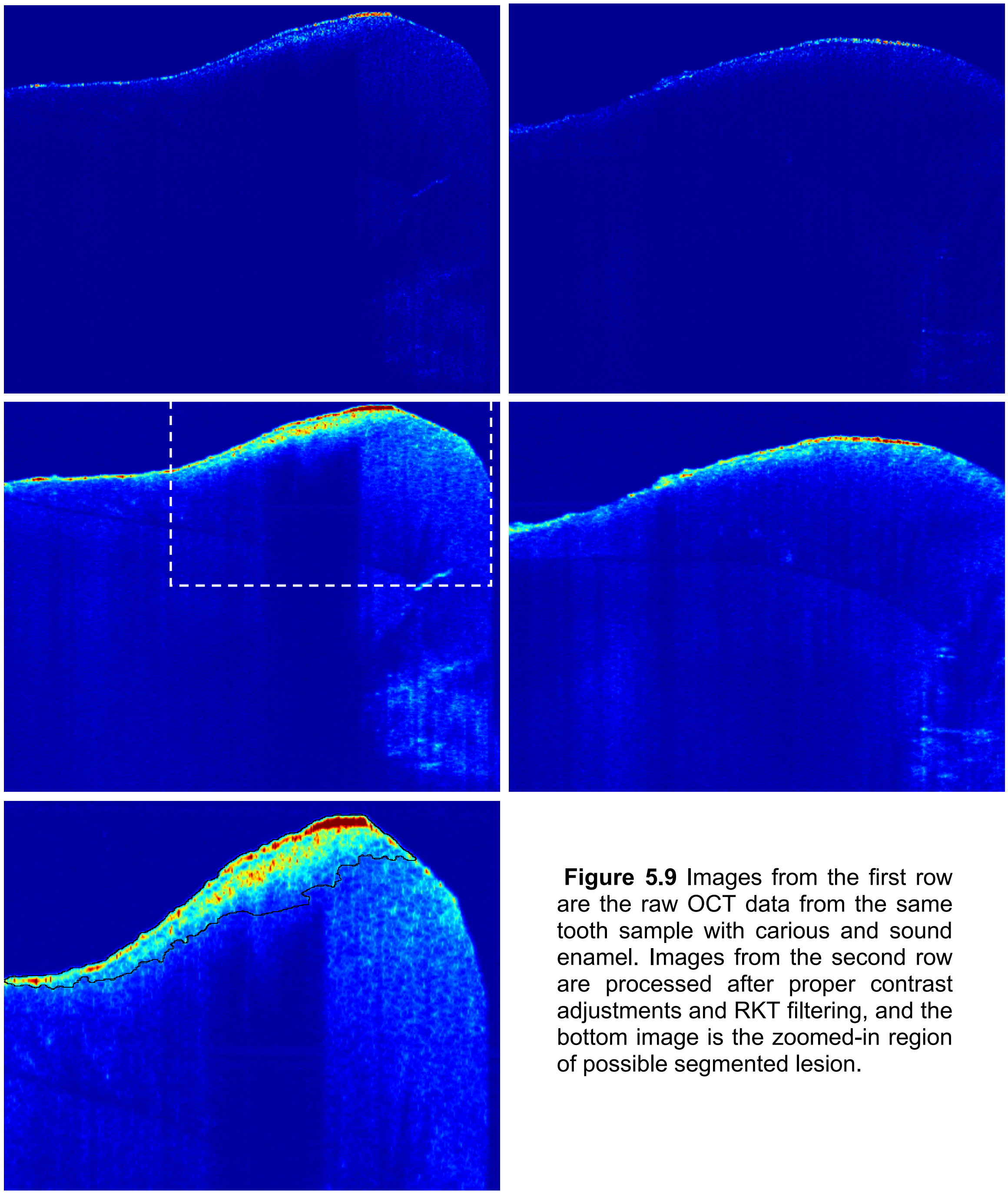

Figure 5.9 Images from the first row are the raw OCT data from the same tooth sample with carious and sound enamel. Images from the second row are processed after proper contrast adjustments and RKT filtering, and the bottom image is the zoomed-in region of possible segmented lesion.

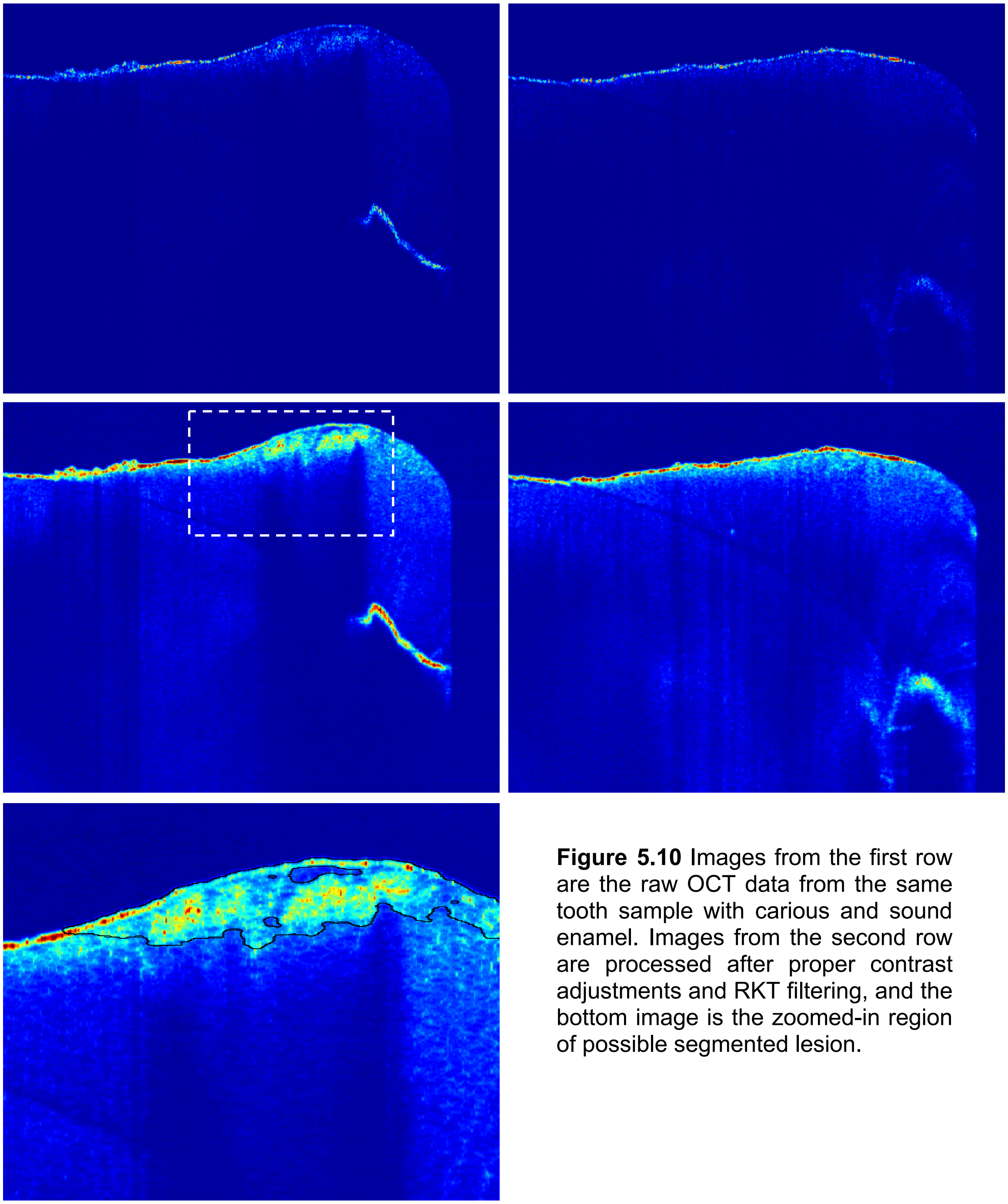

Figure 5.10 Images from the first row are the raw OCT data from the same tooth sample with carious and sound enamel. Images from the second row are processed after proper contrast adjustments and RKT filtering, and the bottom image is the zoomed-in region of possible segmented lesion.

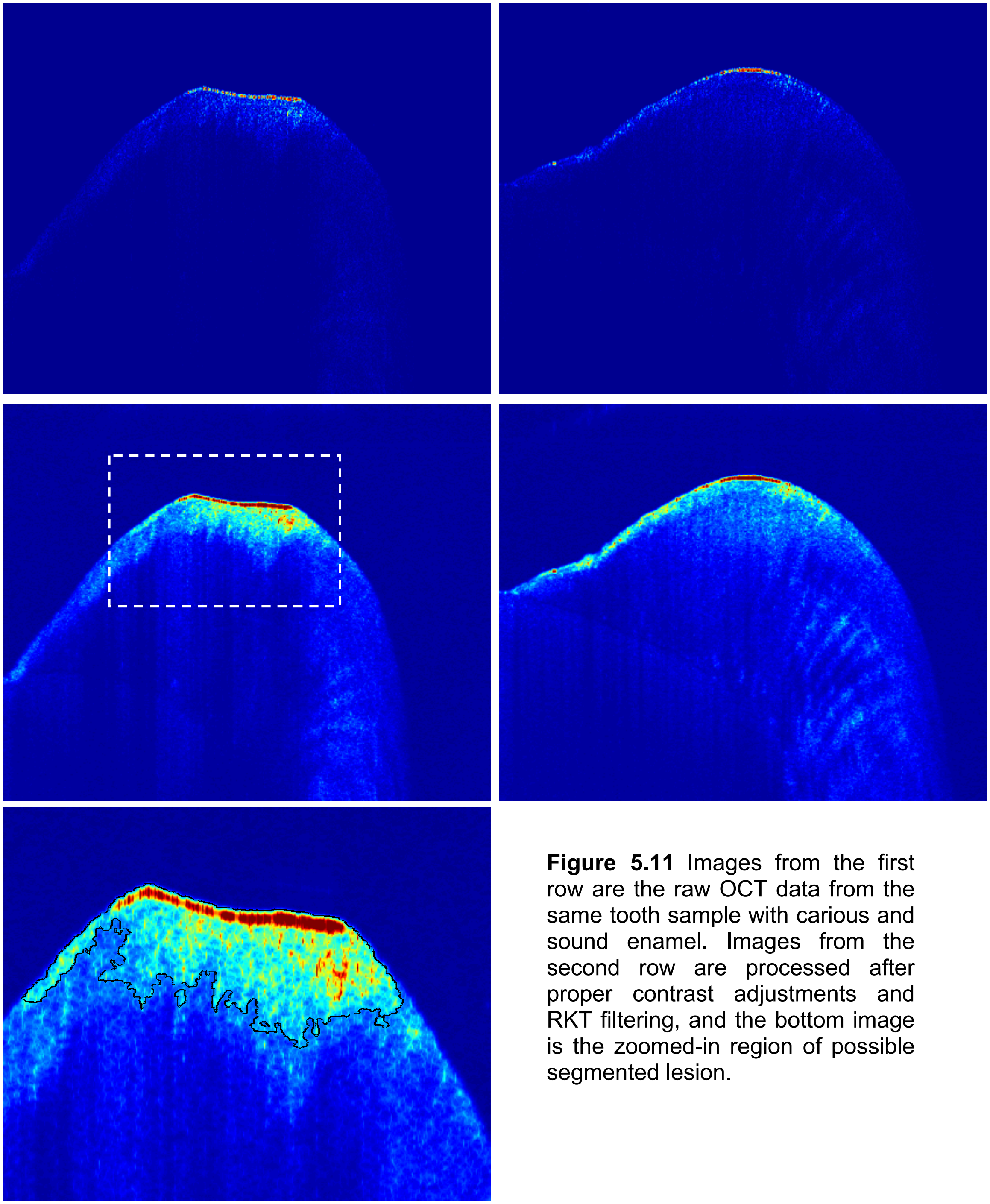

Figure 5.11 Images from the first row are the raw OCT data from the same tooth sample with carious and sound enamel. Images from the second row are processed after proper contrast adjustments and RKT filtering, and the bottom image is the zoomed-in region of possible segmented lesion.

The region-based active contour that evolves according to image statistical properties was applied to OCT dental images in this chapter. The analysis of the images in local regions has led us to model the B-scan image intensity with Rayleigh distributions. The main interests of the algorithm presented in this study are its local adaptiveness and robustness against noise. The semi-automatic lesion segmentation is achieved by evolving from a good guess of the initial contour. The experimental results are extremely good when applied to 1310 nm OCT images. The results have also demonstrated the discrepancy and error when the algorithm is implemented with 850 nm OCT images. A more suitable segmentation method, which is to apply a globally assumed threshold, can generate more accurate segmentation results with less error. This is likely due to the optical property difference with dental hard tissue at 850 nm and 1310 nm frequencies. Also it can be a result of error in image modeling, which we have assumed to be Rayleigh distributed for most of the images. Some further investigation on improvements of the algorithm has been proposed and involves the study to quantify the influence of the contour initialization. Generally, the farther the initial contour is from its final position, the more computations must be done for the contour to converge. Hence, if the contour is selected in almost near the lesion area, it drastically reduces the time needed for segmentation. A global thresholding technique can be first applied to create a rough guess that is close to the shape of the contour. In the case of multiple region segmentations, a heuristic or ranking process can be carried out.

Conclusions and Future Works

The main objective of this thesis was to develop and apply image processing techniques to identify early stage caries and assess lesion extent to determine the stage of the disease. The image processing techniques implemented in the thesis have shown potential results in the early study of non-invasive OCT imaging of incipient stage caries. For OCT images acquired with a 1310 nm center frequency, the combination of image speckle reduction and segmentation has generated satisfying results that holds promise for non-destructive visualization of dental caries and other anatomical structures and is approaching the elusive goals of in-vivo histopathology and optical biopsy. The presence of strong speckles for OCT images obtained at 850 nm center frequency tends to cause under-segmented lesions. Measuring the accuracy of the contour in this case is difficult due to the fact that the lesion areas from 850 nm images do not have clearly defined boundaries. As a result, generating similar contours from the same sample is challenging, and arguably of little reproducibility. However, if a spatial filter with a large filtering mask is applied, an "artificial" boarder line is created, but with an *ad hoc* fashion where a global thresholding is followed adaptively to generate a segmented region.

A number of image processing techniques have been used as part of this project. The techniques implemented all show potential, and different results could possibly be applied to specific applications depending on what types of procedures are required. Other alternative image processing techniques could also be explored. Methods of evaluating tissue texture are also worth exploring. Before any further work is undertaken, three key areas are addressed. First, analysis if speckle reduction results reveal that general spatial domain methods have the advantages of fast computation, adapting image local information and overall better speckle reduction results. The combining different filters within the same speckle reduction step would possibly be beneficial. Also, some research can be done in finding a more sophisticated image evaluation measure to give subjective judgments with greater proximity to human visual perception system. Secondly, a better way of evaluating the image deconvolution results yet needs to be established. Restoring the resolution at the air-tooth surface has a number of applications, such as line detection and image registration. Thirdly, for most of the OCT tooth images, ideally we would like to have a "gold standard" segmentation (a good segmentation that is directly measured from histology images). In such case we could compare the computer generated segmentation with the gold standard. If we could perform this process on a reasonable amount of clinical images, it would be possible to validate and evaluate the performance of the segmentation algorithms. For instance, we could test the hypothesis that the computer generated algorithm is not statistically different from the gold standard. Another approach would simply be to evaluate the difference between the active contour segmentations and the gold standard images or manual segmentation results. If successfully defining a quantitative measure that can reliably indicate a certain region as "carious lesion", an automated system can be developed for caries assessment. To make a reliable segmentation as such, one would need much more data than in the current study. Obviously, the development of such automatic system for clinical study was beyond the scope in this M.Sc. research. Another possibility is to exploit the ability of computerized texture analysis and tissue classification to automatically monitor the rate of caries progression during the course of treatment.

References

[1] W. J. Loesche, “Role of streptococcus mutans in human dental decay,” Microbiology Reviews, Vol. 50, No. 4, p. 353–380, December 1986.
[2] J. D. Featherstone, “An updated understanding of the mechanism of dental decay and its prevention,” Nutr. Qtr. Vol. 14, p. 5–11, 1992
[3] J. D. Featherstone, and B. E. Rodgers, “Effect of acetic, lactic and other organic acids on the formation of artificial carious lesions,” Caries. Res. Vol. 15, No. 5, p.377–385, 1981.
[4] A.I. Ismail, “Visual and visuo-tactile detection of dental caries,” J. Dent. Res. Vol. 83, p.56-66, 2004.
[5] H. C. B. de Vries, H. M. Juiken, and K. G. Konig, “Radiographic versus clinical diagnosis of approximal Carious Lesions,” Caries Res. Vol. 24, p. 364-70, 1990
[6] G. K. Stookey, and C. Gonzalez-Cabezas, “Emerging methods of caries diagnosis,” J. Dent. Educ. Vol. 65, p. 1001-1006, 2001
[7] A. F. Ferreira, and D. T. Zero, “Diagnostic tools for early caries detection”, Journal American Dental Association, Vol. 137, p. 1675-1684, December 2006,
[8] J. Na, J. H. Baeki, S. Y. Ryu, C. Lee, and B. H. Lee, “Tomographic imaging of incipient dental-caries using optical coherence tomography and comparison with various modalities,” Optical Review Vol. 16, No. 4, p. 426–431, 2009
[9] A. Hall, and J. M. Girkin, “A review of potential new diagnostic modalities for caries lesions,” J Dent. Res., Vol. 83 (Spec No C), p. 89-94, 2004.
[10] J. G. Fujimoto, Y. Chen, and A. Aguirre, “Biomedical imaging using optical coherence Tomography,” Biomedical Optical Imaging, Oxford University Press, March 2009, p.161.
[11] B. W. Colston, M. J. Everett, L. B. DaSilva, L. L. Otis, P. Stroeve, and H. Nathel, “Imaging of hard and soft Tissue in the oral cavity by optical coherence tomography” Appl. Optics, Vol. 37, p. 3582–3585, 1998
[12] F. I. Feldchtein, G. V. Gelikonov, V. M. Gelikonov, R. R. Iksanov, R. V. Kuranov, A. M. Sergeev, N. D. Gladkova, M. N. Ourutina, J. A. Warren, Jr., and D. H. Reitze, “In vivo OCT imaging of hard and soft tissue of the oral cavity,” Opt. Express, Vol. 3, p. 239–250,1998.
[13] B. W. Colston, Jr., M. J. Everett, U. S. Sathyam, L. B. DaSilva, and L. L. Otis, “Imaging of the Oral Cavity using Optical Coherence Tomography,”Monogr. Oral Sci., Vol. 17, p. 32–55, 2000.
[14] B. T. Amaechi, S. M. Higham, A. G. Podoleanu, J. A. Rogers, and D. A. Jackson, “Use of optical coherence tomography for assessment of dental caries: quantitative procedure,” J. Oral Rehabil. Vol. 28, p. 1092–1093, 2001.
[15] D. Fried, J. Xie, S. Shafi, J. D. B. Featherstone, T. M. Breunig, and C. Le, “Imaging carious lesions and lesion progression with polarization sensitive optical coherence tomography,” J. Biomed. Opt. Vol. 7, p. 618–627, 2002.
[16] Huang, D., Swanson, E.A., Lin, C.P., Schuman, J.S., Stinson, W.G., Chang, W., Hee, M.R., Flotte, T., Gregory, K., Puliafito, C.A. and Fujimoto, J.G., “Optical coherence tomography,” Science, 1991. 254 (5035): p.1178-81.
[17] R. Hogg, and P. Anderson, “Quantum-dot diodes provide sources for optical coherence tomography” https://spie.org/x8853.xml?ArticleID=x8853
[18] E. A. Swanson, D. Huang, M. R. Hee, J.G. Fujimoto, C. P. Lin, and C. A. Puliafito. “High-speed optical coherence domain reflectometry”, Optical Letter, vol. 17, p. 151-53, 1992
[19] Fujimoto, J. G., Chen, Y., and Aguirre, A., “Biomedical Imaging Using Optical Coherence Tomography,” Biomedical Optical Imaging, Oxford University Press, p.161, March 2009
[20] M. Bath-Balog, and M. J. Febrenbach, “Illustrated dental embryology, histology, and anatomy,” W.B. Suanders Company, Philadelphia, PA., 1997.

[21] B.W. Colston, Jr., M.J. Everett, U. S. Sathyam, and L. Da Silva, "Optical coherence tomography in dentistry," Handbook of Optical Coherence Tomography, New York: Marcel Dekker, 2002.
[22] D. Fried, R. E. Glena, J.D. Featherstone, and W. Seka, "Nature of light scattering in dental enamel and dentin at visible and near-infrared wavelengths," Applied Optics, Vol.34, p.1278-1285, 1995
[23] J. M. Schmitt, "Optical Coherence Tomography (OCT): A Review", IEEE Journal of Selected Topics in Quantum Electronics, Vol. 5, No. 4 , p. 1205-1215, July/August 1999
[24] E. Hecht, Optics, p. 120, Addison Wesley, 2002.
[25] J. A. Izatt, M. R. Hee, G. M. Owen, E. A. Swanson, and J. G. Fujimoto, "Optical Coherence Microscopy in Scattering media", Optical Letter, Vol. 19, p. 590-592, 1994
[26] Y.T. Pan, R. Birngruber, I, Rosperich, and R. Engelhardt, "Low-coherence optical tomography in turbid tissue" Applied Optics, Vol. 34, p. 6564-6574, 1995
[27] T. Hellmuth, "Contrast and resolution in optical coherence tomography," Proceedings SPIE, Vol.2926, p. 228-237, 1997.
[28] M. E. Brezinski, and J. G. Fujimoto, "Optical coherence tomography: high-resolution imaging in nontransparent tissue", IEEE Journal of Selected Topics in Quantum Electronics, Vol. 5, No. 4, pp.1185-1192, July/August, 1999.
[29] B. W. Colston, M. J. Everett, L., and B. Da Silva, "Imaging of hard and soft tissue structure in the oral cavity by optical coherence tomography," Applied Optics, Vol.37, p. 3582-3585, 1998.
[30] B. W. Colston, U. S. Sathyam, and B. Da Silva, "Dental OCT," Optics Express, Vol. 3, p.230-239, 1998.
[31] F. I. Feldchtein, G. V. Gelikonov, V. M. Gelikonov, R. R. Iksanov, R. V. Kuranov, A. M. Sergeev, N. D. Gladkova, M. N. Ourutina, J. A. Warren, Jr. and D. H. Reitze, "In vivo imaging of hard and soft tissue of oral cavity," Optics Express, Vol. 3, p.239-250, 1998.
[32] B. T. Amaechi, S. M. Higham, A. G. Podoleanu, J. A. Rogers, and D.A.Jackson, "Use of optical coherence tomography for assessment of dental caries: quantitative procedure," Journal of Oral Rehabilitation, vol.28, p.1092-1093, 2001
[33] D. Fried, J. Xie, S. Shafi, J. D. B. Featherstone, T. M. Breuning, and C. Le, "Imaging caries lesions and lesion progression with polarization sensitive optical coherence tomography," Journal of Biomedical Optics. Vol. 7, p. 618-627, 2002
[34] R. Brandenburg, B. Haller, and C. Hauger, "Real-time in vivo imaging of dental tissue by means of optical coherence tomography (OCT)", Optical Communication, Vol. 227, pp.203-211, 2003.
[35] M.D. Hewko, L.-P. Choo-Smith, A. C.-T.Ko, L. Leonardi, C. C.S. Dong, B. Cleghorn, and M. G. Sowa, "OCT of early dental caries: A comparative study with histology and Raman spectroscopy" Progress in Biomedical Optics and Imaging - Proceedings of SPIE, Vol. 5687, p 16-24, 2005.
[36] A. C. –T.Ko, L. -P. Choo-Smith, M.D. Hewko, L. Leonardi, M. G. Sowa, C.C.S. Dong,, P. Williams, and B. Cleghorn, "Ex vivo detection and characterization of early dental caries by optical coherence tomography and Raman spectroscopy", Journal of Biomedical Optics, Vol. 10, No. 3, p, 31118-1-16, May 2005.
[37] L.-P. Choo-Smith, M.D. Hewko, M.L. Dufour, C. Fulton, P. Qiu, B. Gauthier, C. Padioleau, C.-E. Bisaillon, C. Dong, B.M. Cleghorn, G. Lamouche, and M.G. Sowa, "Ex vivo imaging of early dental caries within the interproximal space," Proc. SPIE Laser in Dentistry XV., Vol. 7162, p. 716206-1-10, 2009.
[38] M.H. Frosz, M. Juhl, M.H. Lang, "Optical Coherence Tomography: System Design and Noise Analysis", Riso National Laboratory, Roskilde, Denmark, July, 2001.
[39] M. R. Hee, "Optical Coherence Tomography: Theory", Handbook of Optical Coherence Tomography, New York: Marcel Dekker, 2002.

[40] J. Goodman, "Some fundamental properties of speckle", Journal of Optical Society of America, Vol. 66, 1976, p.1145-1150.
[41] J. L. Lim and H. Nawab, "Techniques for speckle noise removal," Optical Engineering, vol. 20, p. 472-480, May/June 1981.
[42] J. M. Schmitt, S.H. Xiang, and K. M. Yung, "Speckle reduction techniques," Handbook of optical coherence tomography, New York: Marcel Dekker, 2002.
[43] B. Bouma, and G. Tearney, Handbook of Optical Coherence Tomography, New York: Marcel Dekker, 2002.
[44] A. Achim, A. Bezerianos, and P. Tsakalides, "Novel Bayesian multiscale method for speckle removal in medical ultrasound Images," IEEE Transaction on Medical Imaging, Vol. 20, p. 772-783, 2001
[45] O. Michailovich, A. Tannenbaum, "Despeckling of Medical Ultrasound Images," IEEE Transaction on Ultrasonics, Ferroelectrics and Frequency Control, Vol. 53, p. 64-78, 2006
[46] M. Bashkansky, J. Reintjes, "Statistics and reduction of speckle in optical coherence tomography," Optics Letters, Vol. 25, p. 545-547, 2000.
[47] B. Karamata, K. Hassler, M. Laubscher, T. Lasser, "Speckle statistics in optical coherence tomography," Journal of Optical Society of America, Vol. 8, p. 593-596, 2005.
[48] M. Pircher, E. Geotzinger, R. Leitgeb, A. Fercher, and C. Hitzenberger, "Speckle reduction in optical coherence tomography by frequency compounding," Journal of Biomedical Optics, vol. 8 2003, pp.565-569.
[49] Andersen, L Thrane, H. Yura, A. Tycho, T. Jorgensen, and M. Frozs, "Advanced Modeling of Optical coherence tomography systems," Physics in Medicine and Biology, Vol. 49, p. 1307-1327, 2004.
[50] L. Thrane, "Optical Coherence Tomography: Modeling and Applications", Ph.D. Dissertation, Riso National Laboratory, Roskilde, Denmark, 2001.
[51] A. K. Jain, Fundamental of Digital Image Processing. Englewood Cliffs, NJ, Prentice-Hall, 1989.
[52] H. Xie, L. E. Pierce, and F. T. Ulaby, "Statistical properties of the logarithmically transformed speckle," IEEE Tran. Geosci. Remote Sensing," Vol. 40, No. 3, p. 721-727, Mar, 2002.
[53] T. R. Hillman, S. G. Adie, V. Seemann, J. J . Armstrong, S. L. Jacques and D. D. Sampson, Correlation of static speckle with sample properties in optical coherence tomography," Optical Letter, 2006
[54] Dan P. Popescu, Michael G. Sowa, Mark D. Hewko, and Lin-P'ing Choo-Smith, "Extracting information from optical coherence tomography images of tissues: signal attenuation and fractal analysis of speckle pattern," Proc. SPIE, Vol. 7555, 2010.
[55] Z. Li, H. Li, Y. He, S. Cai, S. Xie, "A model of speckle contrast in optical coherence tomography for characterizing the scattering coefficient of homogenous tissues," Physics in Medicine and Biology, Vol. 53, No. 20, p. 5859-5866, Oct. 2008.
[56] K.M. Yung, S.L. Lee, and J.M. Schmitt, "Phase-domain processing of optical coherence tomography images," Journals of Biomedical Optics, Vol. 4, p.125-136, 1999.
[57] J.M. Schmitt, "Restoration of optical coherence images of living tissue using CLEAN algorithm", Journal of Biomedical Optics, Vol. 3, pp.66-75, 1998.
[58] J. Lee, "Digital image enhancement and noise filtering by use of local statistics," IEEE Transaction in Pattern Analysis and Computer Intelligence, Vol. 2, p. 165-168, 1980
[59] D. Kuan, A. Sawchuk, T. Strand, P.Chavel, "Adaptive noise smoothing filter for image with signal-dependent noise," IEEE Transaction in Pattern Analysis and Computer Intelligence, Vol. 7, p.165-167, 1985.

[60] V. Frost, J. Stiles, K. Shanmugan, J. Holzman, “A model for radar images and its application to adaptive digital filtering of multiplicative noise,” IEEE Transaction in Pattern Analysis and Computer Intelligence, Vol. 2, p. 157-166. 1982.
[61] A. Ozcan, A. Bilenca, A. E. Desjardins, B. E. Bouma, and G. J. Tearney, “Speckle reduction in optical coherence tomography images using digital filtering,” Journal of Optical Society of America, Vol. 24, p. 11901-1910, 2007.
[62] A. Lopes, R. Touzi, and E. Nezry, “Adaptive speckle filters and scene heterogeneity,” IEEE Transaction on Geo. and Remote Sensing, Vol. 24, no. 6 pp. 992-1000, Nov. 1990.
[63] J. Rogowska and M.E. Breziski, “Evolution of the adaptive speckle suppression filter for coronary optical coherence tomography imaging”, IEEE Transaction on Circuit and Systems, Vol. 19, p.1261-1266, 2000.
[64] H. M. Salinas and D.C. Fernadez. “Comparison of PDE based nonlinear diffusion approaches for image enhancement and denoising in optical coherence tomography,” IEEE Transacting on Medical Imaging, Vol. 26, p. 761-771, 2007.
[65] S. Aja, C. Alberola, and J. Ruiz. “Fuzzy anisotropic diffusion for speckle filtering,” Proceeding IEEE international conference on Acoustics, Speech and Signal Processing, pp.1261-1264, 2001.
[66] D. Adler, T. Ko and J. Fujimoto, “Speckle reduction in optical coherence tomography images by use of a spatially adaptive wavelet filter,” Optics Letters, Vol. 29, No. 24, pp. 2878-2880, 2004.
[67] S. Xiang, L. Zhou and J. Schmitt, “Speckle noise reduction for optical coherence tomography,” Proceedings SPIE, Vol. 3196, p. 79-88, 1997.
[68] S. Xiang and Y. Zhang, “Sensitivity enhancement using nonlinear optical wavelet thresholding for two-dimensional medical ultrasound transducer,” Biomed Eng Appl. Basis Commun. Vol. 9, p. 91-100, 1997.
[69] T. Ralston, I. Atkinson, F. Kamalabadi and S. Boppart , “Multi-dimensional denoising of real-time OCT imaging data,” Proceedings of ICASSP p.1148, 2006
[70] Q. Huynh-Thu, M. Ghanbari, “Scope of validity of PSNR in image/video quality assessment”, Electronics Letters, Vol. 44, p. 800-801, 2008
[71] C. H. Gierull, I. Sikaneta, “Estimating the effective number of looks in interferometric SAR data”, IEEE Trans. Geosci. Remove Sensing, Vol. 40, pp. 1733-1742, Aug, 2002.
[72] Z. Wang, A. C. Bovik, H. R. Sheikh, E. P. Simoncelli, “Image quality assessment: From error visibility to structural similarity”, IEEE Transaction on Image Processing, Vol. 13, No. 4, p. 600-612, April, 2004.
[73] J. S. Lee, “Speckle suppression and analysis for synthetic aperture radar images”, Optical Engineering,” Vol. 25, No. 5, p. 636-643, 1986.
[74] D. T. Kuan, A. A. Sawchuk, T. C. Strand, P. Chavel, “Adaptive restoration of images with speckle,” IEEE Trans. ASSP., Vol. 35, No. 3, p. 373-383, March 1987.
[75] Y.-K. Lee and W. T. Rhodes, “Nonlinear image processing by a rotating kernel transformation,” Opt. Lett., p. 43–46, 1990.
[76] Y. J. Yu, and S. T. Acton, “Speckle reduction anisotropic diffusion,” IEEE Transaction on Image Processing, Vol. 11, p.1260, 2002.
[77] C. S. Burrus, R. A. Gopinath, and H. Guo, Introduction to Wavelets and Wavelet Transforms:
A Primer, Prentice Hall. New Jersey, 1997.
[78] I. Daubechies, Ten Lectures on Wavelets. SIAM Press, Philadelphia, 1992.
[79] Mallat S. A Theory for Multiresolution Signal Decomposition: the Wavelet Representation. IEEE Trans. Pattern Anal Machine Intell., Vol. 11, p.674-693, 1989.
[80] Mallat S. A. “Wavelet tour of signal processing”, Academic Press, London, 1998.

[81] I. Selesnick, R. G. Baraniuk, N. G. Kingsbury, “The dual-tree complex wavelet transform,” IEEE Signal Proc.Vol. 22, p.123–151, 2005.
[82] R. R. Coifman and D. L. Donoho Wavelets and translation-invariant denoising,” New York, Springer Verlag. p.125-150, 1995.
[83] J. L. Starck, E. J. Candès, D. L. Donoho, “The curvelet transform for image denoising,” IEEE Trans Image Proc. Vol.11, p.670-84, 2002.
[84] J. Portilla, V. Strela, M. J. Wainwright and E. P. Simoncelli, “Image denoising using scale mixtures of Gaussians in the wavelet domain. IEEE Trans Image Proc. Vol.12, p.1338-1351, 2003.
[85] D. L. Donoho, I. M. Johnstone, “Adapting to unknown smoothness via wavelet shrinkage,” Jouranl of American Statistical Association, Vol. 90, No. 432, p. 1200-1224, December 1995.
[86] D. L. Donoho, I. M. Johnstone, “Minimax estimation via wavelet shrinkage,” The Annals of Statistics, Vol. 26, No. 3, p. 879-921, 1998
[87] M. Vetterli, G. Chang, B. Yu, “Adaptive wavelet thresholding for image denoising and compression,” IEEE Transactions on Image Processing, Vol. p. 1532–1546, Sep 2000.
[88] Y. Liu, Y. Liang, G. Mu and X. Zhu, “Deconvolution methods for image deblurring in optical coherence tomography, Journal of the Optical Society of America, Vol. 26, No. 1, p. 72, Jan.2009
[89] Y. Yansuno, J, Sugisaka, Y. Sando, Y. Nakamura, S. Makita, M. Itoh, and T. Yatagai, “Non-iterative numerical method for laterally super-resolving Fourier domain optical coherence tomography,” Optics Express, Vol. 14, No. 3, Jan. 2006.
[90] I.-J., Hsu, C.-W. Sun, C.-W, Liu, C.-C. Yang, C.-P Chang, and C.-W. Lin, “Process algorithms for resolution improvement and contrast enhancement in optical coherence tomography,” Vol. 10, No. 6, p. 567-571, Dec. 2003.
[91] M.D. Kulkarni, C.W. Thomas and J.A. Izatt, “Image enhancement in optical coherence tomography using deconvolution,” Vol. 33, No. 16, p. 1365-1367, July 1997.
[92] I. -C. Jan, C.-H. Chiu, E.-K. Tien and G.-J. Jan. “Study on deconvolution algorithms for optical coherent tomography,” Journal of Medical and Biological Engineering, Vol. 23, No. 2, p. 73-78, June 2003.
[93] S. Paes, S. Y. Ryu, J. Na, E. Choi, B.H. Lee, I. K. Hong, “Advantages of adaptive speckle filtering prior to application of iterative deconvolution methods for optical coherent tomography imaging,” Optical and Quantum Electronics, Vol. 37, No. 13-15, p. 1225-1238, December 2005.
[94] T. S. Ralston, D. L. Marks, F. kamalabadi, S. A. Boppart, “Deconvolution methods for mitigation of transverse blurring in optical coherence tomography,” IEEE Trans. Image Processing, Vol. 14, No. 9, p. 1254-1264, Sep. 2005.
[95] Lucy L.B. “An iterative technique for rectification of observed distributions.” The Astronomical journal, Vol. 79, No. 6, p. 745-765, 1974
[96] Richardson W.H. “Bayesian-based method of image restoration.” Journals of Physics. p. 511-532,1972.
[97] D. Boukerroui, “Segmentation of ultrasound images multiresolution 2D and 3D algorithm based on global and local statistics,” Pattern Recognition Letter, Vol. 24, p.779–790, 2003.
[98] Y. L. Huang and D. R. Chen, “Watershed segmentation for breast tumor in 2-D sonography,” Ultrasound Med. Biol., Vol. 30, No. 5, p. 625–632, May 2004.
[99] A. Madabhushi and D. N. Metaxas, “Combining low, high-level and empirical domain knowledge for automated segmentation of ultrasonic breast lesions,” IEEE Trans. Med. Imag., Vol. 22, No. 2, p. 155-169, Feb. 2003.
[100] C. M. Chen, Y. H. Chou, C. S. K. Chen, “Cell-competition: a new segmentation algorithm for multiple objects with irregular boundaries in ultrasound images,” Ultrasound Med. Biol., Vol. 31, No. 12, p. 1647–1664, Dec. 2005.

[101] A. Sarti, C. Corsi, E. Mazzini, and C. Lamberti, "Maximum Likelihood Segmentation of Ultrasound Images with Rayleigh Distribution," IEEE Trans. Ultrasonics, Ferroelectrics, and Frequency Control, Vol. 52, No.6, June 2005.
[102] V. Caselles, R. Kimmel, and G. Sapiro, "Geodesic active contours," Int. J. Computer Vision, Vol. 22, No. 1, p. 61-79, Feb. 1997.
[103] C. Chesnaud, P. Refegier and V. Boulet, "Statistical Region Snake-Based Segmentation Adapted to Different Physical Noise Models" IEEE Transaction on Pattern analysis and machine intelligence, p.1145-1157, 1999.